



Norwegian University of
Science and Technology

Thermal Stimulation of Shale Barriers

Simon Thorbjørnsen
Stavland

Petroleum Geoscience and Engineering

Submission date: June 2017

Supervisor: Andreas Bauer, IGP

Co-supervisor: Erling Fjær, IGP

Norwegian University of Science and Technology
Department of Geoscience and Petroleum

Summary

Some shale sections in petroleum wells have shown to form effective annular barriers with the casing due to creep. These barriers are now acknowledged by the petroleum safety authority of Norway as verified well barrier elements for permanent plug and abandonment. Stimulation of such barriers in areas where shale barriers have not been formed is key to significant cost reduction in offshore plug and abandonment operations. The purpose of this thesis is to investigate whether thermal stimulation of shale barriers can induce sufficient plastic deformation to form a barrier. Failure criteria, plasticity and thermoelasticity related to rocks have been evaluated to understand governing concepts related to this stimulation technique. A coupled temperature-pore pressure finite element analysis was used to study a shale formation in hollow cylinder geometry subject to four days of heating on the borehole wall. Furthermore, a sensitivity analysis with respect to stress conditions and rock and fluid properties was conducted.

The results showed significant displacement into the borehole and plastic strain developing deeper into the formation than the initial stress redistribution. This indicates that heating is a more effective stimulation technique than reducing well pressure. Heating associated pore pressure increase was more important than earth stress increase, resulting in lower effective stress and stress conditions shifting towards the failure envelope. Furthermore, simulation of temperature reduction after heating showed that the established shale deformation due to heating does not recede when temperature reduces to its in-situ state.

Strong stress concentration around the borehole and a lower dilatancy angle were found to be the most important conditions to improve the potential for obtaining a sealing barrier. Hence, a combination of well pressure reduction and thermal stimulation is suggested as a more effective stimulation technique. Moreover, a higher thermal expansion coefficient of the matrix may cause more displacement into the borehole, but is believed to have a limited effect. Permeability in the nano-darcy range is essential for pore pressure accumulation, and a permeability lower than this did not show any significant effects on the displacement of the borehole wall. Stress anisotropy resulted in varying displacement around the borehole, and in general, there was more displacement in the direction of minimum horizontal stress.

The results of the finite element analysis show that heating induced shale barriers is a promising stimulation technique, but further development of simulations, laboratory experiments, and field tests are required to verify its feasibility.

Sammendrag

Noen skiferseksjoner i olje- og gassbrønner har påvist ringromsbarrierer forårsaket av naturlig selvforseglingseffekt. Petroleumstilsynet har nå anerkjent bruken av skifer som ringromsbarriere for permanent plugging- og forlatingsoperasjoner. Stimulering av skifer som ringromsbarriere kan føre til enorme kostnadsreduksjoner knyttet til plugging- og forlatingsoperasjoner utenfor kysten. Denne oppgaven undersøker om oppvarming av skiferformasjoner kan føre til nok plastisk deformasjon for å etablere ringromsbarrierer av skifer. Bruddkriterier, plastisitet og temperaturpåvirking relatert til bergarter har blitt undersøkt for å forstå drivmekanismer knyttet til oppvarming av bergarter. Numerisk simulering med koblet temperatur-poretrykk, som forestiller en skifer i hul-sylinder geometri, ble brukt for å studere fire dagers oppvarming av brønnveggen nærliggende en skiferformasjon. I tillegg, ble det gjennomført en sensitivitetsanalyse med hensyn til spenningsvilkår og bergarts- og fluid egenskaper.

Resultatene viser betydelig forflytting av skifer inn i ringrommet og utvikling av plastisk tøyning dypt inn i modellen utover den opprinnelige spenningsomfordelingen. Dette antyder at oppvarming er en mer effektiv stimuleringsmetode enn å redusere ringromstrykket. Poretrykksøkning var større enn spenningsøkningen tilknyttet oppvarmingen, og førte til lavere effektivspenninger og spenningsforhold nærmere bruddkriteriet. Simulering av temperaturreduksjon etter oppvarming viste at skifer som hadde forflyttet seg inn i brønnen ikke trakk seg tilbake når temperaturen i nærliggende skiferformasjon reduserte til opprinnelig verdi.

En kraftig spenningskonsentrasjon rundt brønnen og en lavere dilatansvinkel var de viktigste egenskapene for å øke forflytning inn i brønnen. En kombinasjon av å redusere ringromstrykk og oppvarming ble derfor foreslått som en mer effektiv stimuleringsmetode. Høyere termisk ekspansjonskoeffisient til skifer kan føre til mer forflytting inn i brønnen, men variasjon av denne egenskapen har begrenset omfang. Permeabilitet i størrelsesorden nanodarcy er essensielt for å oppnå poretrykksakkumulering, og en lavere permeabilitet enn dette viser minimal effekt forflytting inn i brønnen. Anisotrope spenninger førte til varierende forflytting langs brønnveggen, og generelt, var det mer forflytting i retning av den minste horisontale hovedspenningen.

Resultatene fra de numeriske simuleringene viser at oppvarming for dannelse av skifer som ringromsbarriere er en lovende metode. Likevel, trengs videre utvikling av simuleringer, laboratorieforsøk og operasjonelle tester for å verifisere gjennomførbarheten til denne metoden.

Acknowledgment

This master thesis is the concluding work of my Master of Science degree in Petroleum Geosciences and Engineering, specializing in drilling engineerin. It was completed at the Norwegian University of Science and Technology (NTNU), at the Department of Geoscience and Petroleum, during the Spring of 2017 in Trondheim, Norway.

Special gratitude goes to my supervisor at NTNU, Professor Andreas Bauer, who has provided guidance and feedback throughout the work on my master thesis, and introduced me to the current standing and challenges in the industry related to plug and abandonment and shale barriers.

Acknowledgment also goes to my co-supervisor at NTNU, Professor Erling Fjær, for support and advice through the spring of 2017. Furthermore, recognition goes to Ph.D. student Xiyang Xie for helpful and relevant discussion of results. I would also like to thank SINTEF Petroleum Research for allowing me to use and develop their numerical model.

Finally, I would like to thank my girlfriend, family and close friends for great support and motivation throughout the process of completing this thesis.

Table of Contents

- Summary** **iii**
- Sammendrag** **v**
- Acknowledgment** **vii**
- Table of Contents** **ix**
- List of Tables** **xiii**
- List of Figures** **xv**
- Nomenclature** **xix**
-
- 1 Introduction** **1**
- 1.1 Background 1
- 1.2 Approach 3
- 1.3 Structure of Thesis 4
-
- 2 Theory** **5**
- 2.1 Inducing Shale as a Barrier 5
- 2.2 Failure Criteria 7
 - 2.2.1 Basic Concepts 7
 - 2.2.2 Tensile Failure 7
 - 2.2.3 Shear Failure 8
 - 2.2.4 Effective Stress in Failure Criteria 10
- 2.3 Plasticity 12
 - 2.3.1 Dilatency 14
 - 2.3.2 Mohr-Coulomb Yield Criterion Beyond Failure 17
- 2.4 Thermoelasticity 19
 - 2.4.1 Thermal Strain 19
 - 2.4.2 Thermal Stress 19
 - 2.4.3 Thermoporoelastic Effects Around the Borehole 20

2.4.4	Thermally Induced Stress Changes Around the Wellbore	23
3	Method	27
3.1	Finite Element Analysis	27
3.1.1	Heating the Borehole	31
3.1.2	Development of the Finite Element Analysis	31
3.2	Input Parameters	32
3.2.1	Elastic Moduli and Poisson’s Ratio	32
3.2.2	Permeability and Porosity	33
3.2.3	Mohr-Coulomb Plasticity Model	33
3.2.4	Density	35
3.2.5	Thermal Expansion Coefficient	36
3.2.6	Thermal conductivity	37
3.2.7	Heat Capacity	38
4	Approach	41
4.1	Data	41
4.2	Sensitivity Analysis	43
4.3	Sealing Potential	45
4.3.1	The Geomechanical Concept	45
4.3.2	Temperature Effects on Pore pressure and Earth Stress	45
4.4	Hypotheses	46
4.4.1	Predictions for the Sensitivity Analysis	46
4.4.2	Stress Anisotropy Influence on Displacement	49
4.4.3	Pressure-Temperature Relation	49
4.4.4	Proximity to Failure	50
5	Results and Discussion	55
5.1	Output Parameters from the Simulations	55
5.2	Sealing potential	60
5.2.1	Displacement in the Base Case	60
5.2.2	Displacement in the Sensitivity Analysis	61
5.2.3	Influence of Stress Anisotropy	63
5.2.4	Combining Annular Pressure Reduction and Heating to Stimulate Shale Barriers	66
5.3	The Pressure-Temperature Relation	70
5.4	Temperature Reduction After Stimulation	73
5.5	Implications from the Finite Element Analysis	75
5.5.1	Stimulating Shale Barriers	75
5.5.2	Candidate Selection	76

5.5.3	Thermal Considerations	77
5.5.4	Operational Considerations	78
5.6	Recommendations for Further Work and Improvements	80
6	Conclusion	83
	References	85
	Appendices	89
A	Stresses Around the borehole	91
B	Results from the Sensitivity Analysis	93
B.1	Output Parameters from the Simulations	93
B.1.1	Case 2	93
B.1.2	Case 3	96
B.1.3	Case 4	99
B.1.4	Case 5	102
B.1.5	Case 6	105
B.1.6	Case 7	108
B.2	Stress conditions in case 1 and 3	111
B.2.1	Case 1	111
B.2.2	Case 3	113
B.3	The Pressure-Temperature relation	114
B.4	Excerpts from ABAQUS displaying selected output parameters	117
B.4.1	Displacement	117
B.4.2	Radial plastic strain	117

List of Tables

3.1	Stress conditions in FEA	28
3.2	Geostatic stress conditions in the FEA	29
3.3	Predefined fields in the FEA	30
3.4	Boundary conditions and surface sets they apply to	30
3.5	Material properties used in finite element analysis	32
3.6	Conductivity of seawater	38
3.7	Heat capacity of shale matrix and seawater for different temperatures	40
4.1	Pore fluid density used in case 7	44
4.2	Linear thermal expansion coefficient of pore fluid used in case 7	44
4.3	Prediction of sensitivity analysis	46
5.1	Displacement at 97.2 h for N1, N2 and N3	61
5.2	Required shear deformation to seal typical borehole diameter and casing sizes .	75
A.1	Values used to calculate stresses around the borehole in figure A.1	91

List of Figures

2.1	Schematic of a borehole with a casing	5
2.2	Uniaxial and triaxial tests.	8
2.3	Mohr-Coulomb yield criterion with a Mohr circle	9
2.4	Mohr-Coulomb failure surface in principal stress space	11
2.5	Stress-strain curve displaying ideally plastic behavior	13
2.6	Concept of dilation of a loose granular material	14
2.7	Triaxial test results illustrated with three different axes configurations	16
2.8	Stresses around a borehole with a plastic zone	18
2.9	Effect of 50 °C temperature difference between wellbore and formation illustrated by temperature and pore pressure development with time	22
2.10	Thermally induced pore pressure for different rock types	23
2.11	Semi-infinite cylinder inside elastic medium, side-view	24
2.12	Superposed cylinders inside elastic medium, top-view	25
3.1	Schematic of the numerical model, seen from above	28
3.2	Schematic of the quadrant used in the model, seen from above	29
3.3	Excerpt of numerical model from ABAQUS GUI	30
3.4	Failure envelope in the finite element analysis	34
3.5	Density of seawater vs. temperature. Salinity=35g/l, p=16 MPa	35
3.6	Linear thermal expansion coefficient for water and seawater	37
3.7	Graph of experimental heat capacity of rocks vs. temperature	39
3.8	Calculated heat Capacity of seawater (blue) and water (green) as a function of temperature. Pressure=16 MPa	39
4.1	Nodes at the wellbore where displacement is evaluated	42
4.2	Mohr circles in Case 1 and 3 compared with the yield criterion	47
4.3	Mohr circles displaying stress conditions in $\theta = 0^\circ$ and 90° on the borehole wall, case 1	49
4.4	Temperature effects on pore pressure and total stress illustrated by Mohr circles	51
4.5	Proximity to failure in direction $\theta=0^\circ$, with evaluation of temperature effect at $r = 0.18$ m and 1.0 m	53

5.1	Case 1, Temperature profile in the formation resulting from the ABAQUS FEA	56
5.2	Case 1, Radial displacement in the formation resulting from the ABAQUS FEA	57
5.3	Case 1, Pore pressure distribution in the formation resulting from the ABAQUS FEA	57
5.4	Case 1, Void ratio distribution in the formation resulting from the ABAQUS FEA	58
5.5	Case 1, total radial strain in the formation resulting from the ABAQUS FEA . .	59
5.6	Case 1, Radial plastic strain in the formation resulting from the ABAQUS FEA	59
5.7	Case 1, Displacement of the borehole wall vs. time	60
5.8	Displacement vs. Time	61
5.9	Temperature difference between Case 1 and 7	64
5.10	Excerpt of ABAQUS FEA model for Case 1 displaying radial displacement . .	65
5.11	Excerpt of ABAQUS FEA model for Case 1 displaying radial plastic strain . .	66
5.12	Stress conditions at 24 h, case 1	67
5.13	Stress conditions at 24 h, case 3	68
5.14	Pore pressure difference between Case 1 and 3	69
5.15	Pressure-temperature relation, case 1	70
5.16	Radial displacement in the base case including heating and temperature reduction	74
5.17	Schematic of heating induced shale displacement in case 7	76
5.18	Schematic of trapped volume due to heterogeneous shale	78
A.1	Stresses around a borehole, linearly elastic formation	92
B.1	Case 2, Temperature profile in the formation resulting from the ABAQUS FEA	93
B.2	Case 2, Radial displacement in the formation resulting from the ABAQUS FEA	94
B.3	Case 2, Pore pressure distribution in the formation resulting from the ABAQUS FEA	94
B.4	Case 2, Void ratio distribution in the formation resulting from the ABAQUS FEA	95
B.5	Case 2, total radial strain in the formation resulting from the ABAQUS FEA . .	95
B.6	Case 3, Temperature profile in the formation resulting from the ABAQUS FEA	96
B.7	Case 3, Radial displacement in the formation resulting from the ABAQUS FEA	96
B.8	Case 3, Pore pressure distribution in the formation resulting from the ABAQUS FEA	97
B.9	Case 3, Void ratio distribution in the formation resulting from the ABAQUS FEA	97
B.10	Case 3, total radial strain in the formation resulting from the ABAQUS FEA . .	98
B.11	Case 3, Radial plastic strain in the formation resulting from the ABAQUS FEA	98
B.12	Case 4, Temperature profile in the formation resulting from the ABAQUS FEA	99
B.13	Case 4, Radial displacement in the formation resulting from the ABAQUS FEA	99
B.14	Case 4, Pore pressure distribution in the formation resulting from the ABAQUS FEA	100
B.15	Case 4, Void ratio distribution in the formation resulting from the ABAQUS FEA	100

B.16	Case 4, total radial strain in the formation resulting from the ABAQUS FEA . .	101
B.17	Case 4, Radial plastic strain in the formation resulting from the ABAQUS FEA	101
B.18	Case 5, Temperature profile in the formation resulting from the ABAQUS FEA	102
B.19	Case 5, Radial displacement in the formation resulting from the ABAQUS FEA	102
B.20	Case 5, Pore pressure distribution in the formation resulting from the ABAQUS FEA	103
B.21	Case 5, Void ratio distribution in the formation resulting from the ABAQUS FEA	103
B.22	Case 5, total radial strain in the formation resulting from the ABAQUS FEA . .	104
B.23	Case 5, Radial plastic strain in the formation resulting from the ABAQUS FEA	104
B.24	Case 6, Temperature profile in the formation resulting from the ABAQUS FEA	105
B.25	Case 6, Radial displacement in the formation resulting from the ABAQUS FEA	105
B.26	Case 6, Pore pressure distribution in the formation resulting from the ABAQUS FEA	106
B.27	Case 6, Void ratio distribution in the formation resulting from the ABAQUS FEA	106
B.28	Case 6, total radial strain in the formation resulting from the ABAQUS FEA . .	107
B.29	Case 6, Radial plastic strain in the formation resulting from the ABAQUS FEA	107
B.30	Case 7, Temperature profile in the formation resulting from the ABAQUS FEA	108
B.31	Case 7, Radial displacement in the formation resulting from the ABAQUS FEA	108
B.32	Case 7, Pore pressure distribution in the formation resulting from the ABAQUS FEA	109
B.33	Case 7, Void ratio distribution in the formation resulting from the ABAQUS FEA	109
B.34	Case 7, total radial strain in the formation resulting from the ABAQUS FEA . .	110
B.35	Case 7 - Radial plastic strain in the formation resulting from the ABAQUS FEA	110
B.36	Case 1 - Stress conditions, t=0.3 h	111
B.37	Case 1 - Stress conditions, t=96.7 h	112
B.38	Case 3 - Stress conditions, t=0.3 h	113
B.39	Case 3 - Stress conditions, t=97.1 h	113
B.40	Pressure-temperature relation, case 2	114
B.41	Pressure-temperature relation, case 3	114
B.42	Pressure-temperature relation, case 4	115
B.43	Pressure-temperature relation, case 5	115
B.44	Pressure-temperature relation, case 6	116
B.45	Pressure-temperature relation, case 7	116
B.46	Excerpt of ABAQUS FEA model for Case 2 displaying radial displacement . .	117
B.47	Excerpt of ABAQUS FEA model for Case 3 displaying radial displacement . .	117
B.48	Excerpt of ABAQUS FEA model for Case 4 displaying radial displacement . .	118
B.49	Excerpt of ABAQUS FEA model for Case 5 displaying radial displacement . .	118
B.50	Excerpt of ABAQUS FEA model for Case 6 displaying radial displacement . .	119
B.51	Excerpt of ABAQUS FEA model for Case 7 displaying radial displacement . .	119

B.52	Excerpt of ABAQUS FEA model for Case 3 displaying radial plastic strain	. .	120
B.53	Excerpt of ABAQUS FEA model for Case 4 displaying radial plastic strain	. .	120
B.54	Excerpt of ABAQUS FEA model for Case 5 displaying radial plastic strain	. .	121
B.55	Excerpt of ABAQUS FEA model for Case 6 displaying radial plastic strain	. .	121
B.56	Excerpt of ABAQUS FEA model for Case 7 displaying radial plastic strain	. .	122

Nomenclature

Acronyms

FEA	Finite Element Analysis
GUI	Graphical User Interface
IMPBC	Impermeable Boundary Condition
MC	Mohr-Coulomb yield criterion
N1	Node 1
N2	Node 2
N3	Node 3
NCS	Norwegian Continental Shelf
OD	Outer Diameter
OH	Open hole
P&A	Plug & Abandonment
PBC	Permeable Boundary Condition
PP&A	Permanent Plug & Abandonment
PWC	Perforate, Wash and Cement
TVD	True Vertical Depth

Greek Symbols

α	Thermal expansion coefficient
$\bar{\sigma}$	Average stress
β	Orientation of the failure plane
δ_{ij}	Kronecker's delta,
$\dot{\epsilon}$	Strain rate

$\dot{\gamma}$	Shear strain rate
ϵ	Strain
ϵ_{ij}	Strain tensor
γ	Shear strain
κ	Mobility
Λ	lamè parameter
λ	Thermal conductivity
μ	Viscosity
ν	Drained Poisson's ratio
ν	Kinematic viscosity
ω	Scalar related to plastic strain
ϕ	Internal friction angle
ψ	Dilatancy angle
ρ	Density
σ	Stress
σ'	Effective stress
τ	Shear stress
σ_{ij}	Stress tensor

Other Symbols

\mathcal{A} Attraction

Roman Symbols

\hat{k}	Permeability used in ABAQUS FEA
\mathbf{A}	set of hardening thermodynamic forces
B	Skempton B
C	Heat capacity
c	Hydraulic diffusivity
c'	Coupling coefficient
C_0	Uniaxial compressive strength

c_0	Thermal diffusivity
c'_0	Coupling coefficient
d	Dimater
E	Young's modulus
e	Void ratio
f	Yield criterion
G	Shear modulus
g	Gravity constant
g	Plastic potential
h	Height
K	Bulk modulus
k	Permeability
n	Porosity
p	Pressure
r	Radius
S_0	Cohesion (inherent shear strength)
T	Temperature
t	Time
Y_0	Tensile strength

Subscripts

0	Initial state
1	Maximum principal stress direction
2	Intermediate principal stress direction
3	Minimum principal stress direction
θ	Tangential
a	Related to radius of a cylinder with uniform temperature change
b	Bulk
ext	external

<i>f</i>	Pore fluid
<i>fr</i>	Framework
<i>H</i>	Maximum horizontal
<i>h</i>	Minimum horizontal
<i>i</i>	Increments in the simulation
<i>int</i>	internal
<i>L</i>	Linear
<i>m</i>	Matrix
<i>max</i>	Maximum
<i>n</i>	Normal
<i>r</i>	Radial
<i>u</i>	Undrained
<i>V</i>	Volumetric
<i>v</i>	Vertical
<i>void</i>	Void
<i>vol</i>	Volumetric
<i>w</i>	Wellbore
<i>z</i>	Axial

Superscripts

<i>e</i>	Elastic
<i>p</i>	Plastic

Chapter 1

Introduction

1.1 Background

Petroleum wells form effective conduits for production of hydrocarbons from reservoirs to the surface. Casing strings and sealing barriers between casing and surrounding formation prevent undesired leakage of subsurface fluids to the surface. Traditionally, sealing barriers are established by pumping cement and displacing it to the casing shoe. The length of the cemented section and the quality of the bond varies. Common problems related to cementing are lost circulation resulting in top of cement below desired depth and poor removal of mud cake that develops into an annular flow path (Mitchell et al., 2011, p. 144). This may leave sections of the well without proper sealing barriers, which may be acceptable during production when the well is under surveillance, but is not sufficient when the well will be permanently plugged and abandoned (PP&A) (Fjær et al., 2016).

NORSOK standard D-010 rev. 4 (2013) states that a permanent well barrier should be impermeable, non-shrinking, resistant to chemicals, wetting, able to withstand mechanical load/impact and provide long term integrity. Additionally, the annular seal must extend over a minimum of 50 m across the full cross section of the well, include all annuli and seal vertically and horizontally. During plug and abandonment (P&A) operations well barriers must often be improved or new barriers must be established to satisfy these requirements. This can be costly in offshore operations. The cost is related to rig time due to operations such as section milling, cutting and pulling of casing (Williams et al., 2009) or establishing a barrier element through e.g. the perforate, wash and cement method (Ferg et al., 2012). Straume (2013) estimate the total P&A time on the Norwegian Continental Shelf (NCS) to 40 years. It is assumed that 15 rigs works full time and an average P&A operation lasts 35 days. With a rig rate of $\$300\,000\text{ d}^{-1}$ this yields a total cost of $\$65.7 \times 10^9$. Evidently, reducing rig time has the potential for huge cost savings.

NORSOK standard D-010 rev. 4 (2013) does not specify which materials possess the well barrier requirements, and allows the operator to choose a material that meets the requirements. In some cases shale has been observed to establish a sealing barrier with the casing where there previously were no bond, and the shale barrier has been found to satisfy all the well barrier requirements specified by NORSOK standard D-010 rev. 4 (2013) (Williams et al., 2009). If this process occurs and can mitigate certain operations it implies enormous cost saving for offshore P&A. Additionally, it is possible that shale barriers have a better sealing capabilities than cement barriers, since cement permeability typically is 100 to 100 000 larger than shale (Kristiansen, 2015), and cement tends to deteriorate (Fjær et al., 2016). Hence, shale is an excellent candidate as permanent well barrier material and is acknowledged by the Petroleum Safety Authority of Norway as an annular barrier for permanent plug & abandonment (PP&A) (Williams et al., 2009).

As of today, mechanisms involved in forming shale as a barrier are not fully understood. Some shale barriers have been observed to form rapidly, some slowly, and other shale formations does not form seals at all. Understanding the driving mechanisms to induce shale barriers is key to huge cost saving. Currently the following displacement mechanisms are believed to cause shale barriers(Williams et al., 2009; Fjær et al., 2008; Bauer et al., 2017)

- Shear or tensile failure
- Liquefaction
- Chemical effects
- Creep
- Heating

These mechanisms may act alone or in combination. The mechanism occurring from heating the borehole wall will be studied in this report.

1.2 Approach

Heating shale formations is expected to lead to a pore pressure increase because thermal expansion of the pore fluid is larger than that of the shale matrix. The pore pressure accumulates in the zones where temperature is changed when hydraulic diffusion is sufficiently low, i.e. in the nano-Darcy range (Li, 1998). Pore pressure increase result in decreasing effective stresses, which in turn may lead to rock failure and plastic deformation that can close the existing annulus between shale and casing.

The plastic deformation resulting from heating the wellbore is evaluated using finite element analysis (FEA). The model was originally made by SINTEF Petroleum Research, and have been further developed and used through the course of this thesis. Material parameters used in the model are based on a literature study of shale parameters to establish confidence in the numerical values, and their influence by temperature.

The resulting reduction of the borehole radius was evaluated based on typical gaps between casing and borehole diameters. Additionally, a sensitivity analysis was conducted to analyze which material parameters had more influence on plastic deformation. The behavior resulting from the finite element analysis was assessed based on expectations from governing theory and deductions resulting from the sensitivity analysis.

1.3 Structure of Thesis

Chapter 2, Theory: Introduction of existing and relevant theory for the thesis. Failure criteria, plasticity and thermoelasticity are central topics.

Chapter 3, Method: Describes the finite element analysis and discuss material properties related to the numerical model.

Chapter 4, Analysis: Presents which data that were extracted from the finite element analysis, describe the sensitivity analysis, and how the data was analyzed. Additionally, hypotheses regarding expected results were discussed.

Chapter 5, Results and Discussion: Results were presented in graphs and tables and discussed in relation to the hypotheses, governing theory and comparing results in the sensitivity analysis. Implications from the simulations in relation to feasibility, and recommendations for further work were discussed.

Chapter 6, Conclusion: Summarizes the most important findings from the finite element analysis and sensitivity analysis.

Chapter 2

Theory

2.1 Inducing Shale as a Barrier

To induce shale as an annular barrier shale formation surrounding a borehole needs to displace radially into the borehole until it seals onto the casing. Figure 2.1 shows a typical case with a $12\frac{1}{2}''$ hole diameter and $9\frac{5}{8}''$ casing diameter. For this situation the 36.5 mm gap, Δr , must be closed, which represent a shear deformation $\frac{\Delta r}{r_w}=23\%$ that the shale formation must undergo (Fjær et al., 2016).

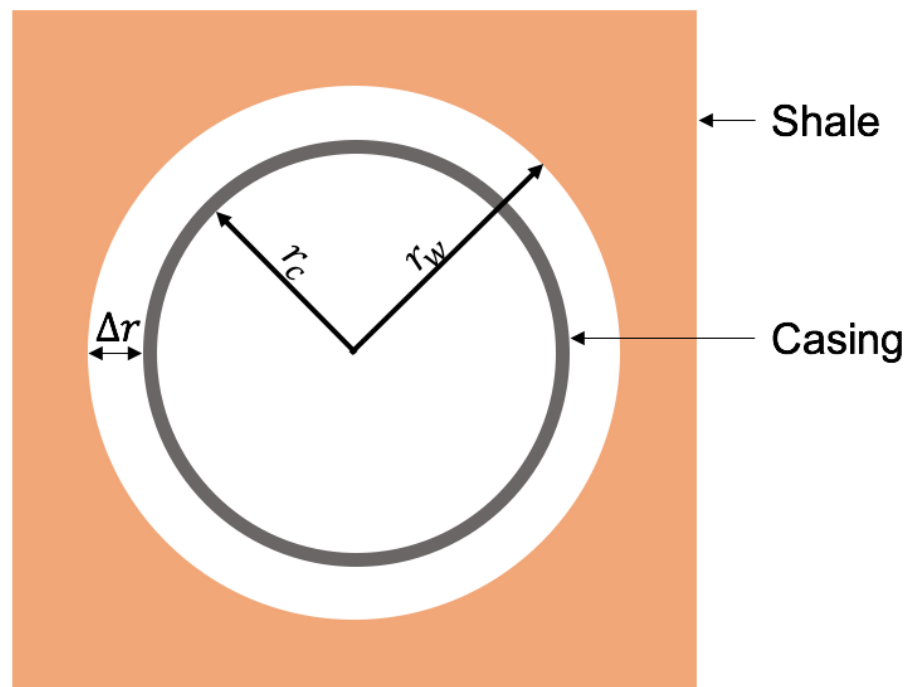


Figure 2.1: Schematic of a horizontal cross section of a borehole with a casing. The aspect ratio resembles a $9\frac{5}{8}''$ casing diameter and $12\frac{1}{2}''$ hole (inspired by Fjær et al. (2016)).

For isotropic horizontal stresses and a linearly elastic formation, shear deformation of the borehole wall due to drillout, is given by

$$\frac{\Delta r}{r_w} = \frac{\sigma_h - p_w}{2G} \quad (2.1)$$

where σ_h is horizontal far field stress, p_w is well pressure, G is shear modulus of the rock, r is radius and r_w is well radius (Fjær et al., 2008, p. 140). Reducing pressure such that $\sigma_h - p_w = 23$ MPa, requires $G = 0.05$ GPa to induce a seal through elastic deformation. However, in many cases such a pressure reduction requires atmospheric pressure inside the well, and the shear modulus of rocks are typically 100-1000 times larger than this value (Fjær et al., 2008, p. 439). This suggest that plastic deformation is required to establish shale barriers.

When a rock sample is subject to sufficiently large stresses failure will occur. Failure implies that the rock sample changes its shape permanently, meaning that plastic deformation takes place. According to (Fjær et al., 2008, p. 55) "rock failure is a complex process, which is still not fully understood", and many current rock failure models are "based on convenient mathematical descriptions of observed behavior, rather than derivations from basic laws of physics". In relation to petroleum wells failure of rock is the root to problems such as borehole instability and solids production, and knowledge of rock failure is used to mitigate these issues (Fjær et al., 2008, p. 55). On the other hand, to induce shale as a barrier, it may be possible to activate failure of the rock surrounding the borehole such that plastic deformation can close the gap between the casing and formation.

2.2 Failure Criteria

2.2.1 Basic Concepts

The stress level a rock can endure before it fails is called the strength of the rock. Stress level depends on stress geometry, thus rock strength can only be specified for a given stress geometry. The most common tests to measure rock strength are called uniaxial and triaxial tests. The triaxial test is performed on a cylindrical specimen, sealed with a watertight rubber, and placed in a cell such that confining pressure can be applied with fluid pressure. A pair of pistons apply a gradually increasing force on the circular end faces of the specimen so that an axial stress is applied. Uniaxial tests are conducted as triaxial tests without confining pressure (Fjær et al., 2008, p. 55). Figure 2.2a show a typical result for axial stress vs. deformation from a uniaxial test and denoting basic concepts, which are defined in the following list (Fjær et al., 2008; de Souza Neto et al., 2008).

Elastic domain: Range of stresses where the behaviour is purely elastic, meaning that releasing stress will allow the sample to return to its original shape. The elastic domain is delimited by the yield stress.

Yield stress: Permanent changes will occur beyond this point such that the sample will not return to its original shape when stress is released .

Uniaxial compressive strength: The peak stress.

Ductile domain: Loading the sample beyond the yield stress causes permanent deformation to the sample, i.e. evolution of plastic strains. The sample is subject to permanent deformation and is still able to support load.

Brittle region: The sample's ability to support stress decrease rapidly as deformation increases.

A triaxial test is often performed by increasing the axial and confining loads simultaneously. The confining pressure is increased until desired level, and then axial stress is increased until failure. This is seen for different confining loads in Figure 2.2b. It is observed that the sample in the triaxial test increases its ability to support load with increasing confining pressures, in addition it becomes less brittle. This illustrates the complexity of rock failure and that it is hard to give a precise definition of failure. From Figure 2.2a it can be argued that the peak stress of the curve represents the failure. However, with increasing confining pressure, the rock is able to withstand loads exceeding this point.

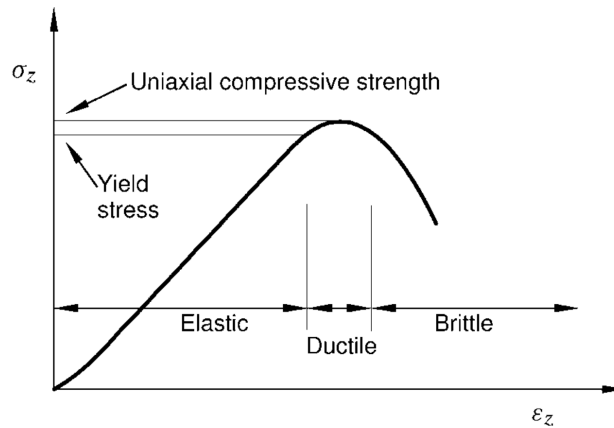
2.2.2 Tensile Failure

Tensile failure is defined by (Fjær et al., 2008, p. 59) to occur "when the effective tensile stress across some plane in the sample exceeds a critical limit". The limit is known as the tensile

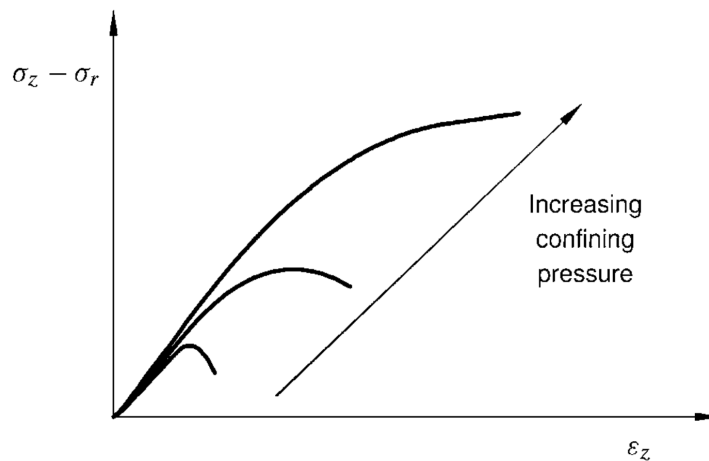
strength of the rock, denoted Y_0 . For isotropic rocks, tensile failure will occur when

$$\sigma'_3 = -Y_0 \tag{2.2}$$

where σ'_3 is effective minimum principal stress.



(a) Axial stress vs. axial deformation in a typical uniaxial test (Fjær et al., 2008, p. 56).



(b) Axial stress minus confining stress vs. axial deformation in a typical triaxial test (Fjær et al., 2008, p. 57).

Figure 2.2: Uniaxial and triaxial tests.

2.2.3 Shear Failure

The most common mode of failure in uniaxial and triaxial tests is shear failure. Shear failure occurs when shear stress overcome the limiting critical shear stress along some plane in a specimen, and as a result a fault zone develops along the same plane. Mohr’s hypothesis states

that the critical shear stress, τ_{max} , depends on the effective normal stress, σ'_n , acting over the failure plane.

Mohr-Coulomb Yield Criterion

The Mohr-Coulomb yield criterion assumes that the critical shear stress is a linear function of normal stress expressed as

$$\tau_{max} = S_0 + \tan(\phi)\sigma'_n \quad (2.3)$$

where τ_{max} is critical shear stress, σ'_n is effective normal stress, ϕ is angle of internal friction and S_0 is cohesion (Fjær et al., 2008, p. 61). Figure 2.3 show the Mohr-Coulomb criterion represented by the failure line, and a Mohr's circle representing the stress state. The parameter \mathcal{A} in Figure 2.3 is called the *attraction*, and defines the distance from the failure line's intersection point to the origin. The attraction is given by

$$\mathcal{A} = S_0 \cot(\phi) \quad (2.4)$$

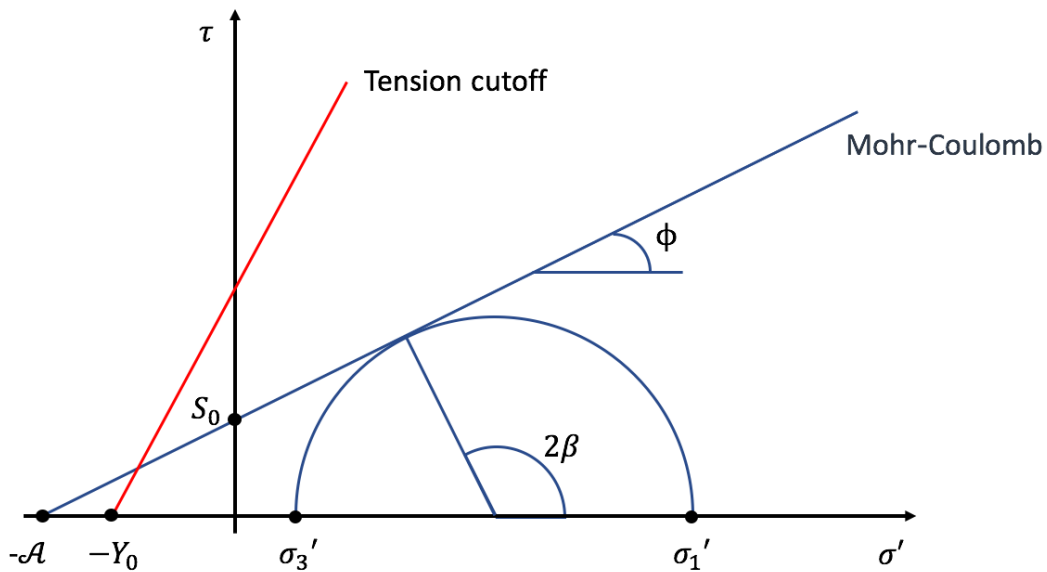


Figure 2.3: Tension cutoff and Mohr-Coulomb yield criterion in $\tau - \sigma'$ space. The Mohr stress circle is drawn, and touches the failure line (inspired by (Fjær et al., 2008, p.62) and (ABAQUS FEA, 2014)).

The attraction is inaccessible due to tensile failure occurring prior to reaching the attraction. Hence, the Mohr-Coulomb shear failure envelope is defined by both the blue Mohr-Coulomb failure line and the red tension cutoff line in Figure 2.3. The red tension cutoff line is drawn to illustrate that the Mohr circle cannot exist to the left of $\sigma' = -Y_0$.

The symbol β in Figure 2.3 is the orientation of the failure plane, and is related to the the internal friction angle by (Fjær et al., 2008, p. 62)

$$\beta = \frac{\pi}{2} + \frac{\phi}{2} \quad (2.5)$$

The Mohr-Coulomb yield criterion rewritten in terms of principal stresses is expressed as

$$f = \sigma'_1 - 2S_0 \frac{\cos(\phi)}{1 - \sin(\phi)} - \sigma'_3 \frac{1 + \sin(\phi)}{1 - \sin(\phi)} \quad (2.6)$$

where σ'_1 and σ'_3 are the maximum and minimum principal effective stress, respectively. f is the symbol of the yield function, such that $f = 0$ represents the onset of shear failure (Fjær et al., 2008).

The uniaxial compressive strength, C_0 , seen in Figure 2.2a, can be obtained from equation (2.6) by having $\sigma'_3 = 0$, which yields

$$C_0 = 2S_0 \frac{\cos(\phi)}{1 - \sin(\phi)} = 2S_0 \tan(\beta) \quad (2.7)$$

Applying the relations in equations (2.5) and (2.7) in equation (2.6) yields a more simple form of the Mohr-Coulomb criterion:

$$\sigma'_1 = C_0 + \tan^2(\beta)\sigma'_3 \quad (2.8)$$

In principal stress space the Mohr-Coulomb criterion is a hexagonal pyramid, seen in Figure 2.4. The advantage with Mohr-Coulomb is that it fits experimental data very well, however, observed from its failure surface there are discontinuities along the ridges, making it difficult to use in modelling. The Drucker-Prager yield criterion has the shape of a right circular cone in principal stress space, making it more suitable for modelling (Li, 1998, p. 39).

2.2.4 Effective Stress in Failure Criteria

The effective stress, σ' , used in the failure criteria above is defined as

$$\sigma' = \sigma - p_f \quad (2.9)$$

where σ is stress and p_f is pore pressure. This definition for rocks undergoing failure is generally accepted in the literature. The effective stress expression including the poroelastic Biot constant, α , is not used because it is derived assuming linearly elastic rock, which is not true for rock at failure (Fjær et al., 2008, p. 76).

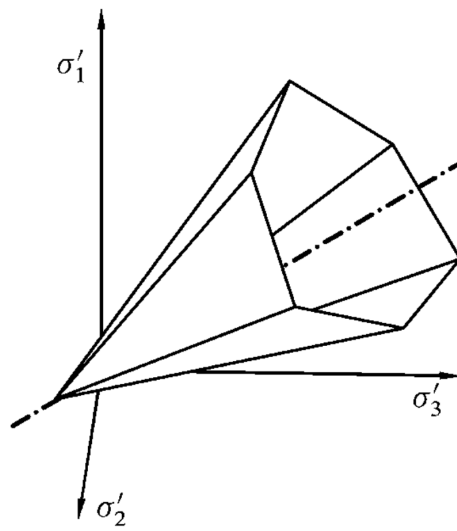


Figure 2.4: Mohr-Coulomb failure surface in principal stress space (Fjær et al., 2008, p. 69).

2.3 Plasticity

Rocks stressed beyond their yield point undergo non-elastic deformation in the ductile region seen in Figure 2.2a. Ductile behaviour of rocks is often described by the theory of plasticity, which is based on four main concepts: (Fjær et al., 2008, p. 81)

1. **Elastoplastic strain decomposition:** the strain tensor, ϵ_{ij} , is assumed to equal the sum of an elastic component, ϵ_{ij}^e , and a plastic component, ϵ_{ij}^p (Fjær et al., 2008; de Souza Neto et al., 2008):

$$\epsilon_{ij} = \epsilon_{ij}^e + \epsilon_{ij}^p \quad (2.10)$$

The elastic strain increment, ϵ_{ij}^e , will disappear when stress is relieved, while the plastic strain, ϵ_{ij}^p , is permanent.

2. **A Yield criterion:** defines a surface in stress space where plastic deformation is initiated (Fjær et al., 2008, p. 82). The yield criterion is negative in the elastic domain and is constant and equal to zero during plastic flow. Thus plastic flow occurs only when

$$f(\sigma_{ij}, \mathbf{A}) = 0 \quad (2.11)$$

where σ_{ij} is the stress tensor and \mathbf{A} is a set of hardening thermodynamic forces (de Souza Neto et al., 2008, p. 50).

3. **A flow rule:** describes the relationship between plastic strain and a given loading situation.
4. **A hardening rule:** describes changes of the yield surface in stress space. Rocks are able to sustain more or less load after initial failure. Consequently, the initial yield surface and the current yield surface may not be the same after some plastic strain (Fjær et al., 2008, p. 82).

Plastic behavior can generally be divided into three types:

- (a) Strain hardening: plastic strain increases when stress increase
- (b) Strain softening: plastic strain increase when stress decrease
- (c) Ideally plastic: plastic strain increase while stress is constant

The failure surface changes with increasing deformation in the case of strain hardening/softening and keeps unchanged in the case of ideal plastic deformation (Li, 1998, p. 36). An example of ideally plastic deformation is shown in Figure 2.5, where the initial linear stress-strain curve is the elastic region, and the horizontal stress-strain curve is the ideal plastic deformation.

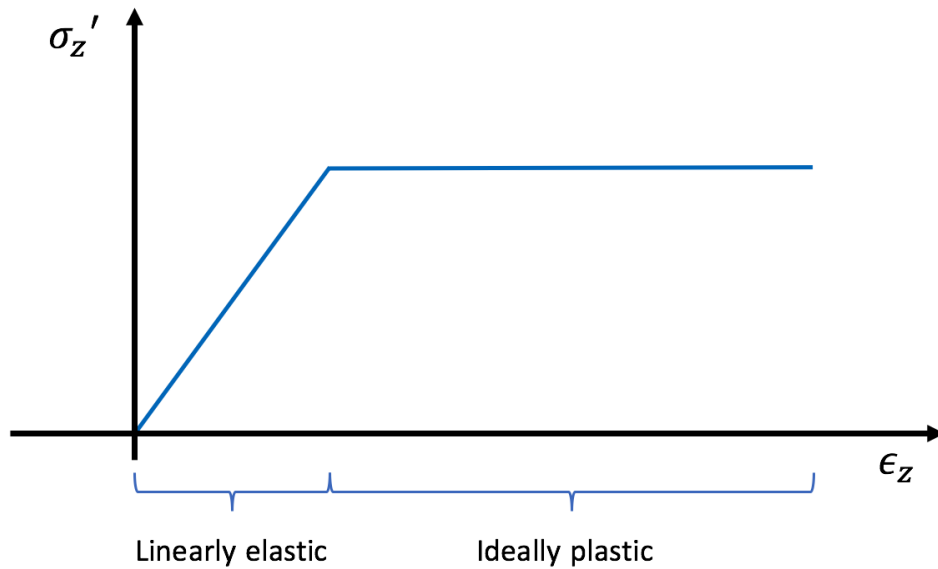


Figure 2.5: Stress-strain curve for linearly elastic then ideally plastic behavior (inspired by Fjær et al. (2008)).

Plastic deformation is a dissipative process, which implies that it follows the thermodynamic law (Fjær et al., 2008, p. 83)

$$\sum_{ij} \sigma'_{ij} d\epsilon_{ij}^p \quad (2.12)$$

where $d\epsilon_{ij}^p$ is the strain increment associated with a stress increment. A simplified expression for plastic strain increment is

$$d\epsilon_{ij}^p = d\omega \frac{\delta g}{\delta \sigma'_{ij}} \quad (2.13)$$

Where ω is a scalar not specified by the flow rule, and g is a scalar function that when differentiated with respect to stresses gives the plastic strains. The function g is called plastic potential, and must obey equation (2.12). Unlike equation (2.12), equation (2.13) is not a thermodynamic law, consequently not all materials follows this rule (Fjær et al., 2008, p. 83).

Some materials have a plastic potential equal their yield surface, $g = f$. These materials are said to follow an *associated (plastic) flow rule*, because the flow is associated with a particular yield criterion. Materials with plastic potential different from their yield surface follows a *non-associated (plastic) flow rule* (Fjær et al., 2008, p. 84)

Associated flow assumes that once a material is brought to its yield surface in a principal stress state, plastic deformation begins. This flow rule has been confirmed by many experiments on metals. However, it overestimate plastic volume expansion for soils and rocks, hence a non-associated flow rule should be used for these materials (Fjær et al., 2008; Li, 1998).

For a plastic potential associated with the Mohr-Coulomb yield criterion, $g = f$ in equation (2.6). For a material with a non-associated flow rule, the plastic potential can be found by

replacing the friction angle in the Mohr-Coulomb criterion with a different angle:

$$g = \sigma'_3 - \frac{1 + \sin(\psi)}{1 - \sin(\psi)} \sigma'_1 + 2S_0 \sqrt{\frac{1 + \sin(\psi)}{1 - \sin(\psi)}} \quad (2.14)$$

where Ψ is called the dilatancy angle.

2.3.1 Dilatency

The phenomenon of inelastic increase in volume of a material undergoing stress is known as *dilatancy*. The concept of dilatancy for granular materials is shown in Figure 2.6, where the material is subject to sufficient stress such that shear distortion occurs in parts of the material. The packing then becomes rearranged such that volume changes. Depending on the initial packing of the material volume may increase or decrease due to shear distortion (Vermeer and de Borst, 1984).

The dilatancy of a material with associated flow can be categorized according to the friction angle, ϕ , of a material as follows (Fjær et al., 2008):

1. $\phi > 0$: The material is positively dilatant (volume increases)
2. $\phi = 0$: The material does not change volume (incompressible plastic) flow
3. $\phi < 0$: The material is negatively dilatant (contracting)

In the case of non-associated flow, where friction angle is replaced with a dilatancy angle, the categorization above is applicable for Ψ greater, equal or less than zero, similar to that of ϕ (Fjær et al., 2008). Dilatancy angle is used to characterize dilatant materials, and represents the "ratio of plastic volume change over plastic shear strain", however this description is only exact for simple shear (Vermeer and de Borst, 1984).

Materials with high dilatancy angle will experience more volume increase than materials with

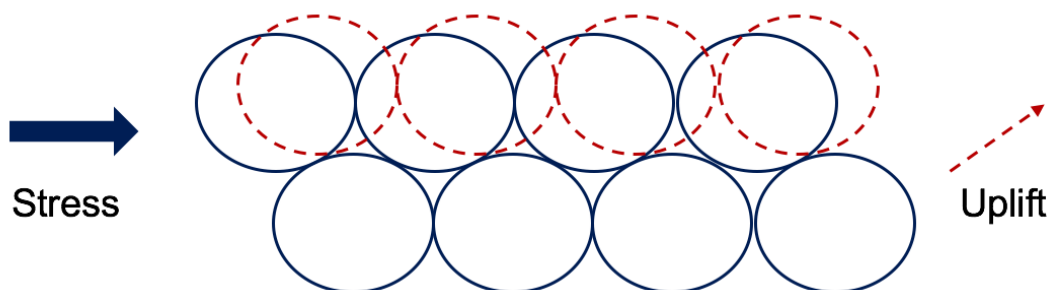


Figure 2.6: Illustration of dilation of a loose granular material subject to shear stress. Blue circles show initial state, and red stippled circles show the rearranged packing of the material (inspired by Vermeer and de Borst (1984)).

lower dilatancy angles when subject to shear distortion. For soils, rock and concrete dilatancy angle is reported to be 0° to 20° , whereas internal friction angle is typically 15° to 45° . Thus dilatancy angle is generally smaller than friction angle. Numerical values for dilatancy angle are 15° for very dense sand and close to zero for clay. Materials will not dilate infinitely, and dilatancy angle gradually goes to zero as shearing no longer causes any volume change (Vermeer and de Borst, 1984). Additionally, with increasing confining pressures dilatancy decays and eventually vanishes (Vermeer and de Borst, 1984; Ding et al., 2016)

The result of a typical triaxial test for loose or cemented granular material is shown in Figure 2.7. The increasing volumetric strain in the ductile region denotes a positive volume change of the specimen, and illustrates the dilatancy of the material. The graphs are divided into three sections based on the stress-strain curve in Figure 2.7a based on the slope: **I**) nearly linear, **II**) monotonically decreasing, and **III**) negative. In terms of plasticity theory, these three sections are related to an elastic region, a hardening region and a softening region, respectively (Vermeer and de Borst, 1984).

Section III in Figure 2.7c shows that there is a linear relation between change in volume and change in axial strain, meaning that the rate of dilation is constant. Furthermore, at the end of the hardening region in Figure 2.7a axial stress increase is almost zero. This implies that elastic strain rate is close to zero, such that all further strain increments are plastic. Consequently, section III in Figure 2.7c is of plastic nature. Based on this observation, the following equation is formulated (Vermeer and de Borst, 1984)

$$\psi = \arcsin \frac{\dot{\epsilon}_{vol}^p}{\dot{\epsilon}_{vol}^p - 2\dot{\epsilon}_3^p} \quad (2.15)$$

where $\dot{\epsilon}_{vol}^p$ is volumetric plastic strain rate, and $\dot{\epsilon}_1^p$ is plastic strain rate in the direction of minimum principal stress. This relation for the dilatancy angle holds for triaxial tests and plane strain conditions. The dilatancy angle in equation (2.15) do not include plastic shear strain. By applying the relations in equations (2.16)-(2.18), the dilatancy angle in equation (2.15) can be expressed as equation (2.19), which shows how dilatancy angle is related to the ratio of plastic volume change over plastic shear strain (Vermeer and de Borst, 1984).

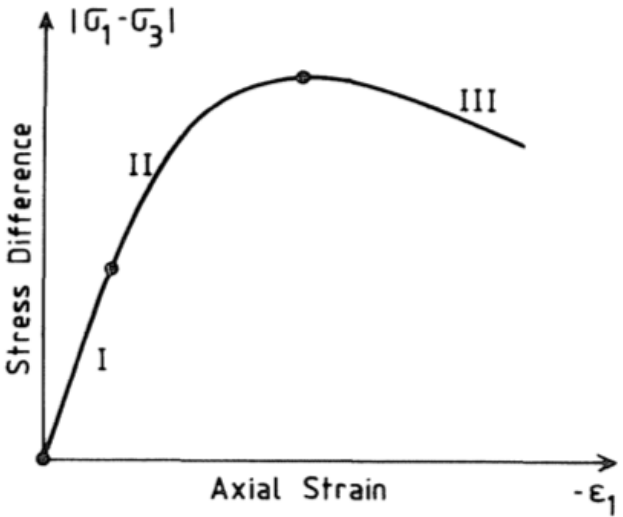
$$\dot{\epsilon}_{vol} = \dot{\epsilon}_1^p + \dot{\epsilon}_2^p + \dot{\epsilon}_3^p \quad (2.16)$$

$$\dot{\epsilon}_2^p = 0 \quad (2.17)$$

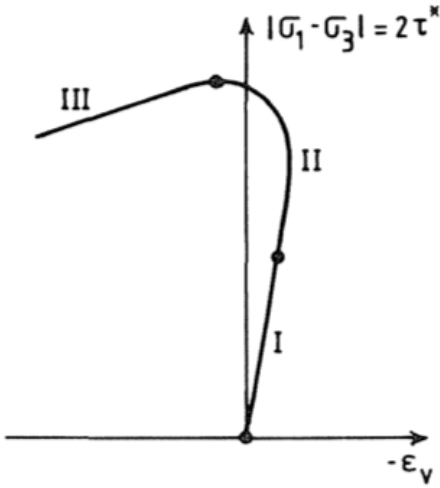
$$\dot{\gamma}^p = |\dot{\epsilon}_1^p - \dot{\epsilon}_3^p| \quad (2.18)$$

$$\psi = \arcsin \frac{\dot{\epsilon}_{vol}^p}{\dot{\gamma}^p} \quad (2.19)$$

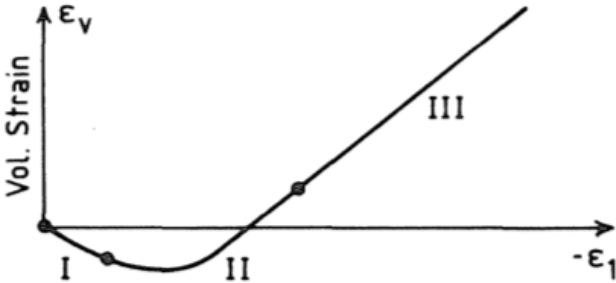
where $\dot{\gamma}^p$ is the shear strain rate and subscripts 1, 2 and 3 refer to the maximum, intermediate and minimum principal stress directions, respectively.



(a)



(b)



(c)

Figure 2.7: Typical triaxial test results for loose or cemented granular material displayed with different axes to illustrate the behavior (Vermeer and de Borst, 1984).

2.3.2 Mohr-Coulomb Yield Criterion Beyond Failure

Fjær et al. (2008) presents a simplified analytic plasticity model using the Mohr-Coulomb criterion to calculate the extent of a plastic zone surrounding a borehole. An ideally plastic formation is assumed where the yield criterion marks the transition from elastic to plastic behaviour. The rock closest to the borehole has experienced shear failure according to the Mohr-Coulomb criterion and acts as a plastic material, while the material outside the plastic zone is intact and in the elastic regime. Furthermore, it is assumed that $\sigma'_r = \sigma'_3$ and $\sigma'_\theta = \sigma'_1$ in the evaluated region, where σ'_r and σ'_θ are effective radial and tangential stress, respectively, around the borehole (Fjær et al., 2008, p. 167).

The resulting stress conditions surrounding the wellbore are shown in Figure 2.8, where R_p denotes the radius of the plastic zone. In contrast, stresses around the borehole for a linearly elastic formation is described in Appendix A, where Figure A.1 show a similar plot, but without the plastic zone. In comparison σ_θ in Figure 2.8 decreases close to the wellbore due to the presence of the plastic zone.

The extent of the plastic zone caused by the Mohr-Coulomb failure criteria depends on the well pressure and the friction angle of the formation. Increasing well pressure will reduce the plastic zone, seen from Figure 2.8 and equation (2.8). Furthermore, the plastic zone reduces as friction angle increases, also seen from equation (2.8) (Fjær et al., 2008, p. 167).

As mentioned Figure 2.8 represents a simplified model of plasticity beyond failure, and is intended to give an overview of expected behavior. More realistic models include softening/hardening properties, which affects the failure criterion with loading, and include a flow potential. These more advanced models are usually implemented in finite element models (Fjær et al., 2008, p. 167).

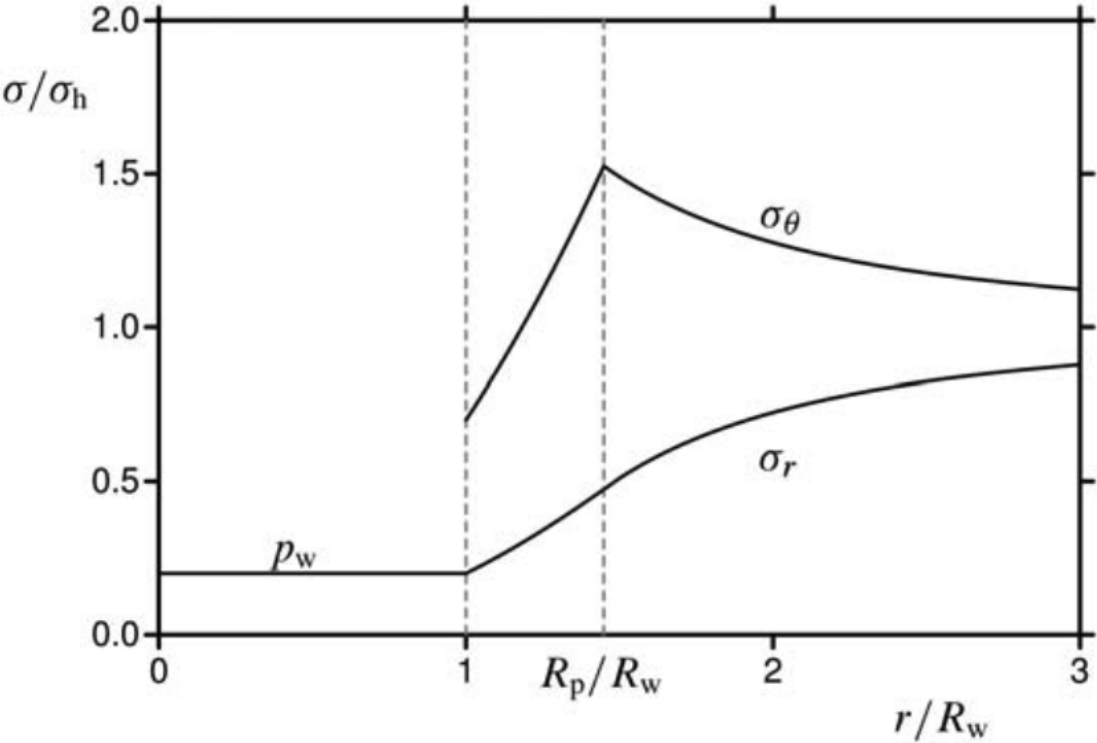


Figure 2.8: Stresses around a borehole with a plastic zone. Mohr-Coulomb failure criteria is assumed in the intact and plastic zone. $C_0 = 0.1\sigma_h$, $p_w = 0.2\sigma_h$, $\phi_f = 30^\circ$ (Fjær et al., 2008, p. 168).

2.4 Thermoelasticity

2.4.1 Thermal Strain

Most materials expand or contract when undergoing temperature change. For an elastic rod, free to expand, the axial thermal strain, ϵ_z , resulting from changing temperature from T_0 to T is given by

$$\epsilon_{z,T} = -\alpha_L(T - T_0) \quad (2.20)$$

where α_L is the coefficient of linear thermal expansion. The minus sign originates from the sign convention of strain. Elongation of a material causes negative strain, thus the minus sign ensures negative strain for a positive change in temperature. (Fjær et al., 2008, p. 24). Typical linear thermal expansion coefficients for shale are in the order $10 - 20 \cdot 10^{-6} K^{-1}$ (Fjær et al., 2008, p. 441). Thermal expansion for fluids are often specified by a volumetric thermal expansion, α_V , which is related to linear thermal expansion by (Fjær et al., 2008, p. 24)

$$\alpha_V = 3\alpha_L \quad (2.21)$$

2.4.2 Thermal Stress

The general relation between stress and strain may be written in compact form as

$$\sigma_{ij} = \Lambda \epsilon_{vol} \delta_{ij} + 2G \epsilon_{ij} \quad (2.22)$$

where coefficients Λ , and G are elastic moduli, respectively known as the lamè parameter and shear modulus. δ_{ij} is kronecker's delta, and subscript i and j can be 1, 2 or 3 representing the x-, y-, and z-axis. Kronecker's delta is given by

$$\delta_{ij} = \begin{cases} 1 & \text{when } i = j \\ 0 & \text{when } i \neq j \end{cases} \quad (2.23)$$

If a material subject to change in temperature is confined it will undergo thermal stress. The stress strain relations including thermal effects is given by

$$\sigma_{ij} = \Lambda \epsilon_{vol} \delta_{ij} + 2G \epsilon_{ij} + 3\alpha_L K (T - T_0) \delta_{ij} \quad (2.24)$$

where K is the bulk modulus (Fjær et al., 2008, p. 25). The contribution of thermal effects is found by subtracting (2.24) from (2.22). The change in stress caused by thermal effects is given by

$$\Delta \sigma_{ij} = 3\alpha_L K (T - T_0) \delta_{ij} \quad (2.25)$$

2.4.3 Thermoporoelastic Effects Around the Borehole

During drilling, rock is replaced with fluid to form a wellbore. The fluid exerts a specified pressure in the wellbore to prevent it from collapsing. This causes two time-dependent poroelastic effects; (1) for permeable wellbore walls fluid pressure diffuses from the well into the formation, and (2) stress concentration around the well is changed, causing an immediate pore pressure increase which reduces with time. The second effect is often referred to as the undrained loading effect (Chen and Ewy, 2005).

Thermal effects must also be considered due to temperature difference between fluid in the well and in-situ formation temperature. Thermal effects induce stresses, seen from equation (2.25), in addition pore pressure changes are induced due to expansion/contraction of pore fluid when temperature diffuses into the formation. The latter temperature effect is highly dependent on whether there is a permeable boundary condition (PBC) or an impermeable boundary condition (IMPBC). An IMPBC prevents fluid pressure invasion into the formation, while temperature distributions remain the same. Consequently, pore pressure change will depend only on the temperature field for an IMPBC. For a PBC both wellbore pressure and temperature has an effect on pore pressure, hence thermal diffusion and hydraulic diffusion are fully coupled (Chen and Ewy, 2005).

The distribution of temperature and pore pressure are controlled by the diffusivity equations. Fully coupled diffusivity equations including both time-dependent poroelastic effects and thermal effects can be expressed as (Chen and Ewy, 2005)

$$\frac{\partial T}{\partial t} = c_0 \left(\frac{\partial^2 T}{\partial r^2} + \frac{1}{r} \frac{\partial T}{\partial r} \right) + c'_0 \left[\frac{\partial T}{\partial r} \frac{\partial p}{\partial r} + T \left(\frac{\partial^2 p}{\partial r^2} + \frac{1}{r} \frac{\partial p}{\partial r} \right) \right] \quad (2.26)$$

$$\frac{\partial p}{\partial t} = c \left(\frac{\partial^2 p}{\partial r^2} + \frac{1}{r} \frac{\partial p}{\partial r} \right) + c' \frac{\partial T}{\partial t} \quad (2.27)$$

where T is temperature, p is pressure, t is time, r is radius, c is hydraulic diffusivity, c_0 is thermal diffusivity, and c'_0 and c' are coupling coefficients. c , c_0 , c'_0 c' are respectively given by

$$c = \frac{2\kappa GB^2(1 + \nu_u)^2(1 - \nu)}{9(1 - \nu_u)(\nu_u - \nu)} \quad (2.28)$$

$$c_0 = \frac{\lambda}{\rho_b C_b} \quad (2.29)$$

$$c'_0 = \frac{\kappa}{n} \quad (2.30)$$

$$c' = \frac{c}{\kappa} \left[\frac{2\alpha_{m,V}(\nu_u - \nu)}{B(1 + \nu_u)(1 - \nu)} + \phi(\alpha_{f,V} - \alpha_{m,V}) \right] \quad (2.31)$$

where ν is drained poisson's ratio, ν_u is undrained poisson's ratio, λ is thermal conductivity, ρ_b

is bulk density of the rock, C_b is heat capacity of the bulk rock, n is rock porosity, and $\alpha_{m,V}$ and $\alpha_{f,V}$ are volumetric thermal expansion coefficient of rock matrix and pore fluid respectively. κ is mobility ratio and B is Skempton B coefficient given respectively as

$$\kappa = \frac{k}{\mu} \quad (2.32)$$

$$B = \frac{\Delta p_f}{\Delta \bar{\sigma}} = \frac{\frac{K_f}{\phi} \left(1 - \frac{K_{fr}}{K_m}\right)}{\frac{K_f}{\phi} \left(1 - \frac{K_{fr}}{K_m}\right) + K_{fr} \left(1 - \frac{K_f}{K_m}\right)} \quad (2.33)$$

where k is permeability, μ is viscosity, $\bar{\sigma}$ is the average stress, and K_f , K_{fr} and K_m are bulk modulus of the pore fluid, framework and rock grains respectively (Chen and Ewy, 2005).

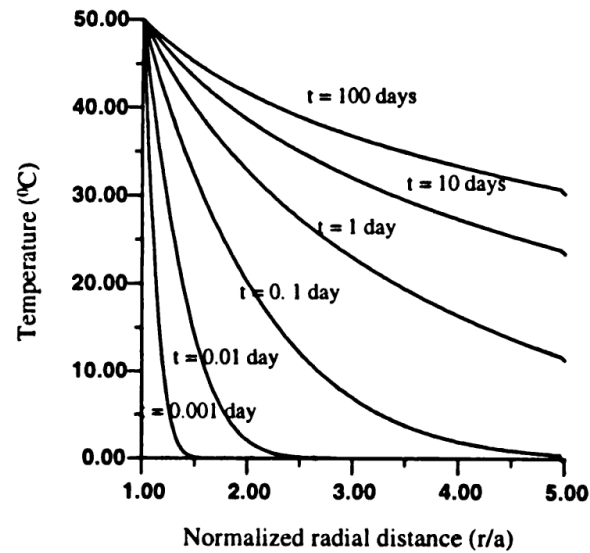
Equation (2.26) incorporates both heat conduction and heat convection to calculate temperature distributions. Thermal diffusivity, c_0 , is multiplied with the second derivative of temperature denoting the contribution of heat conduction to temperature changes. The coupling coefficient, c'_0 , is involved in two parts; the first part includes mass flux and the first derivative of temperature, and represents heat convection on temperature changes, the second part represents the effect of pressure diffusion on temperature changes. In equation (2.27) the hydraulic diffusivity, c , denotes the pore pressure diffusion, and the coupling coefficient, c' , represent the effect of temperature variations on pore pressure changes (Chen and Ewy, 2005).

The differential equations (2.26) and (2.27) can be solved using finite-difference method. However, depending on the relative magnitude between the four coefficients c , c' , c_0 and c'_0 , equations (2.26) and (2.27) may be partially decoupled so that they can be solved analytically in the real-time domain and with laplace inversion (Chen and Ewy, 2005; Li, 1998).

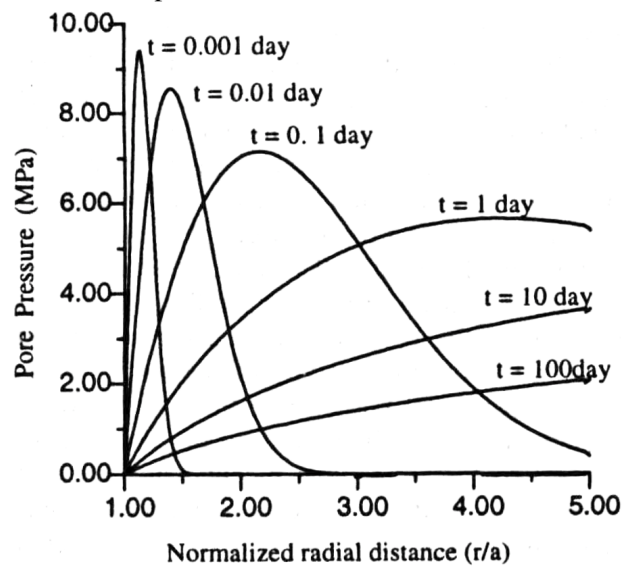
By solving the differential equations, a relation between temperature and pore pressure vs. radial distance from the wellbore is obtained as a function of time. Li et al. (1999) solves the equation for a 50 °C warmer wellbore than formation, and obtain the graphs in Figure 2.9a and Figure 2.9b. The relation between temperature and radial distance from the wellbore is transient, and temperature inside the formation increases with time. The pore pressure effects shown in Figure 2.9b represent a PBC. Maximum induced pore pressure decrease with time and its location moves from close to the wellbore to further into the formation (Li et al., 1999). For an IMPBC maximum is always at the wellbore wall, and decreases with time (Chen and Ewy, 2005).

When $c \gg c'$, pore pressure changes can be considered independent of temperature changes. This is typical for high-permeability formations, and is interpreted as the pore pressure front moving much faster than the temperature front. In this a case equation (2.27) can be partially decoupled, and pore pressure change can be considered steady state Chen and Ewy (2005).

For low-permeability shale hydraulic diffusion, c , may be much smaller than the coupling coefficient, c' . Consequently, transient pore pressure diffusion may be ignored, and pore pressure



(a) Temperature variation near the wellbore



(b) Pore pressure variation near the wellbore for a PBC

Figure 2.9: Effect of 50 °C temperature difference between wellbore and formation illustrated by temperature and pore pressure development with time (Li et al., 1999).

will be a steady-state function of temperature changes for specific radial distances. However this is only applicable for large distances and long time when temperature diffusion reaches a pseudo-steady state distribution. Additionally, $c_0 \gg c'_0$ for low-permeability shale such that the c'_0 term may be ignored in equation (2.26). This allows the partially decoupling of equation (2.26) to

$$\frac{\partial T}{\partial t} = c_0 \left(\frac{\partial^2 T}{\partial r^2} + \frac{1}{r} \frac{\partial T}{\partial r} \right) \quad (2.34)$$

The thermally induced pore pressure is governed by the coupling coefficient, c' . From equation (2.31) it is observed that some of the factors influencing the coupling coefficient are porosity,

thermal expansion of the matrix, and differential between thermal expansion of matrix and fluid. Additionally pore pressure accumulation is governed by the permeability, which can be observed from the c -term in equation (2.27). Thermal expansions between formation-fluid systems are typically the same, whereas porosity and permeability varies. Consequently high thermally induced pore pressures are found in formations with high porosity and low permeability. This is confirmed by Figure 2.10, where thermally induced pore pressure have been plotted for three different rock types with different combinations of porosity and permeability (Li et al., 1999).

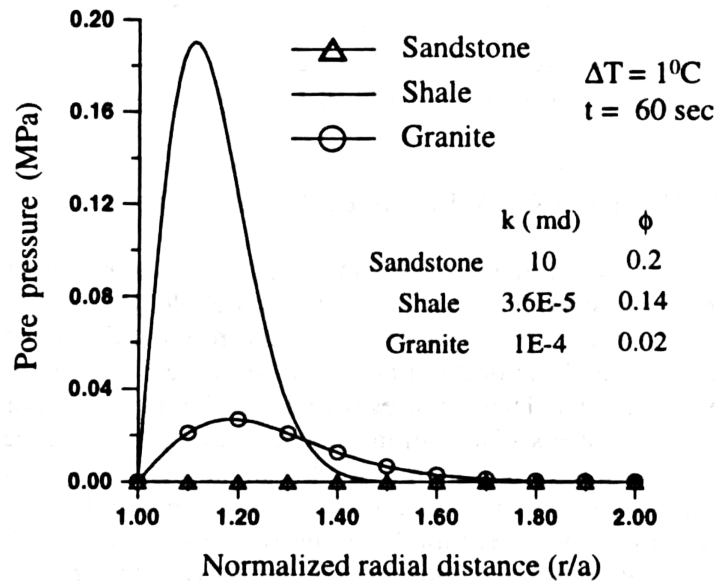


Figure 2.10: Thermally induced pore pressure for different rock types (Li et al., 1999).

2.4.4 Thermally Induced Stress Changes Around the Wellbore

Stress changes at any position caused by temperature change are not a point function, it is rather dependent on the entire temperature field. In agreement with this condition, Perkins and Gonzalez (1984) describe solutions for thermally induced stress changes around a wellbore based on a disk/cylinder-shaped region with altered temperature surrounded by an infinite elastic medium. The model is shown schematically in Figure 2.11, where the disk/cylinder and infinite elastic medium is denoted interior and exterior, respectively. The disk/cylinder has a diameter d , and height h . The interior region has a uniform temperature change, while the exterior region is unaffected. The boundary between the two regions are at $r = r_a$.

The solution to the thermoelastic stresses are found through superposing three vertically aligned cylinders; Two semi-infinite cylinders with an overlap is subtracted from an infinite cylinder. Depending on the ratio d/h , the resulting stresses represent a disk or cylinder shaped region with temperature change ΔT . Stresses are relatively uniform throughout the interior region and

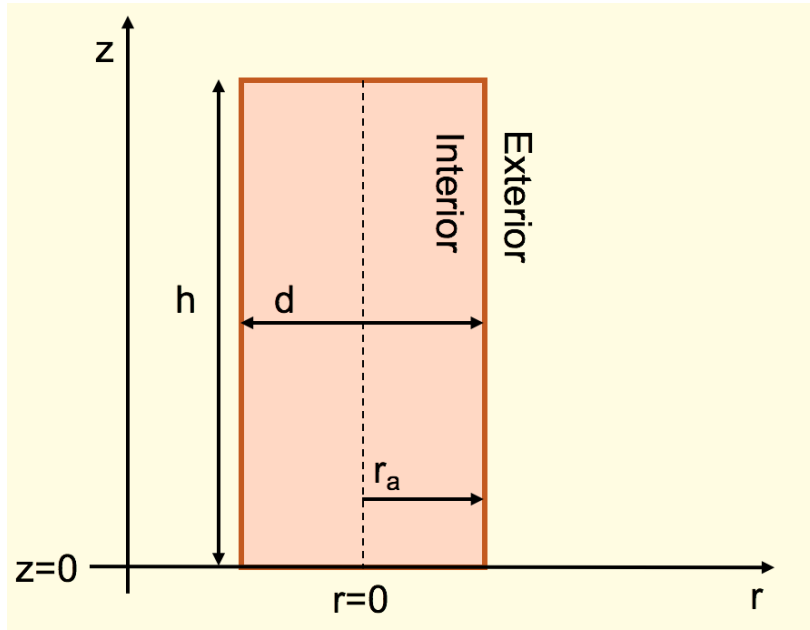


Figure 2.11: Side-view of semi-infinite cylinder inside elastic medium.

stresses in the exterior region decrease rapidly with increasing radial distance from the disk, and with increasing distance in z -direction (Perkins and Gonzalez, 1984).

Analytical solutions for thermally induced stress change exist, however stress change for disk-ratios $0 < d/h < \infty$ are very time consuming to obtain, and it may be sufficient to use approximations in this region. The analytical solutions for the two extreme conditions of an infinite cylinder and an infinite disk are expressed more easily. The thick bed formula is obtained by considering an infinitely long cylinder where $d/h \rightarrow 0$. Similar to the hollow-cylinder model, the infinite cylinder model will be in plane strain conditions. Applying this condition with Hooke's law and Lamé's equation yields a change in horizontal and vertical stress in the interior region, $r < r_a$, respectively as (Perkins and Gonzalez, 1984)

$$\Delta\sigma_{H,int} = \frac{E\alpha_L\Delta T}{2(1-\nu)} \quad (2.35)$$

$$\Delta\sigma_{v,int} = \frac{E\alpha_L\Delta T}{1-\nu} \quad (2.36)$$

where subscript *int* denotes the interior region, and α_L is linear thermal expansion coefficient. In the exterior region, $r > r_a$, the change in radial and tangential stress is a function of radial distance from the center of the cylinder, and expressed by

$$\Delta\sigma_{r,ext} = \Delta\sigma_{Hi} \left(\frac{r_a}{r}\right)^2 \quad (2.37)$$

$$\Delta\sigma_{\theta,ext} = -\Delta\sigma_{Hi} \left(\frac{r_a}{r}\right)^2 \quad (2.38)$$

Where subscript *ext* denotes the exterior region.

The thin bed formula where $d/h \rightarrow \infty$, lateral motion is prevented by shear stresses at the top and bottom of the disk, while vertical stress is unchanged. Based on Hooke's law, change in horizontal stress in the interior region becomes

$$\Delta\sigma_{H,int} = \frac{E\alpha_L\Delta T}{1-\nu} \quad (2.39)$$

2.4.4.1 Annular Elements of Finite Thickness

Thermally induced stress for annular elements can be obtained by further superposition of disks or cylinders with different d/h ratios. Since temperature diffusion into the formation is a transient process, different regions will have different temperatures. This is modeled by having many cylinders with different ΔT to approximate similar conditions as depicted in Figure 2.9a. Figure 2.12 shows an example where several cylinders with different diameters are superposed to form annular elements with altered temperature conditions ΔT_1 , ΔT_2 , ΔT_3 and ΔT_4 (Perkins and Gonzalez, 1984).

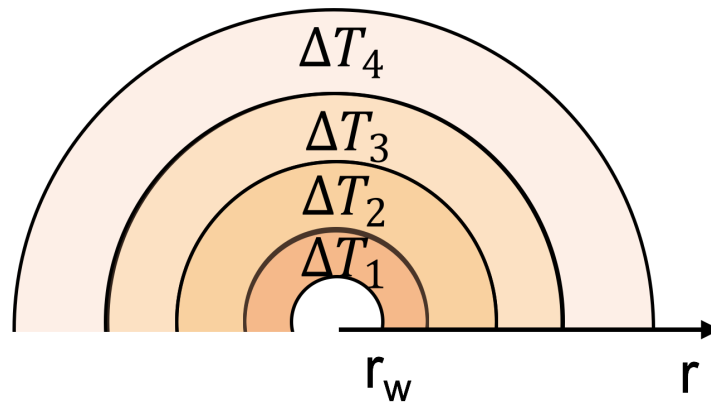


Figure 2.12: Top-view of superposed cylinders inside elastic medium.

Chapter 3

Method

3.1 Finite Element Analysis

Finite element analysis was used to study the effect of heating the borehole wall and whether resulting plastic deformation could be sufficient to form a sealing barrier with the casing. The shape of the model was a rectangular cube with dimensions $4\text{ m} \times 4\text{ m} \times 1\text{ m}$ with a 0.2 m diameter hole in the center representing the borehole. An anisotropic stress state with σ_v , σ_H and σ_h was included in the model to simulate the in-situ stress conditions present around the borehole, where vertical stress is parallel to the borehole. For simplicity, a casing inside the borehole was not included. A schematic of the model is illustrated in Figure 3.1 displaying a horizontal cross section of the model, direction of stresses and dimensions.

The stresses σ_v , σ_H and σ_h are the principal stresses σ_1 , σ_2 and σ_3 , respectively. There are no shear stress perpendicular to the principal stresses (Fjær et al., 2008), thus two axes of symmetry are drawn perpendicular to the horizontal stresses in Figure 3.1. There can not be any displacement perpendicular to the axes of symmetry because there is zero shear stress. This symmetry condition was used to reduce the model to only one of the quadrants, which save time when performing the numerical simulations. The single quadrant is shown in Figure 3.2 with boundary conditions along the axes of symmetry, thus ensuring the symmetry condition is valid. The boundary conditions are denoted $U1 = 0$ and $U2 = 0$, where U refer to displacement, and 1 and 2 refers to the x - and y -axis, respectively. The model extend 1 m into the plane, such that the boundary conditions apply on the surface spanned by the symmetry axes. Furthermore, the model resembles a segment of a longer petroleum well, similar to the hollow cylinder model (Fjær et al., 2008), hence, plane strain conditions apply. Consequently, the bottom and top horizontal planes are subject to symmetry boundary conditions where there is no displacement in the z -direction.

The model was developed using ABAQUS FEA (6.14). The shape, dimensions and mesh size

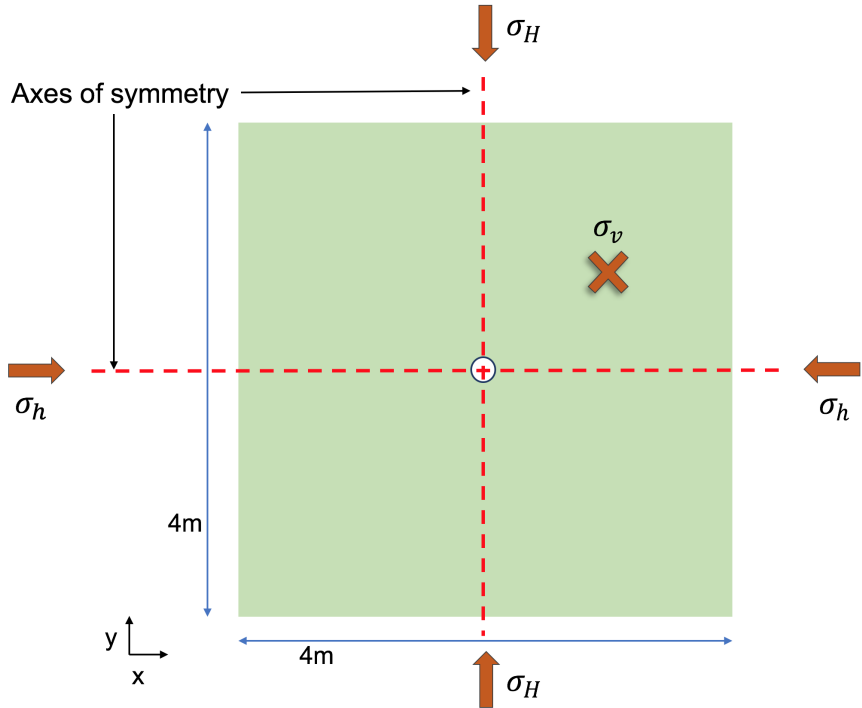


Figure 3.1: Schematic of the numerical model, seen from above displaying dimensions, stress conditions and axes of symmetry.

of the model are shown in Figure 3.3. The model consist of one part and has the shape of a rectangular cube with a quarter of a cylinder extruded in one corner representing the borehole. The origin was placed in the center of the cylinder on the bottom surface. The part was assigned material properties to feature a shale formation. The properties of the material are discussed in section 3.2.

The model was based on conditions at 1500 mTVD. The vertical stress was based on an average overburden density of 2000 kg/m^3 , and the horizontal stresses were lower and unequal to represent normal stress conditions with anisotropic horizontal stresses. Pore pressure was based on an average fluid density of 1000 kg/m^3 , shown in Table 3.3. Pressure equilibrium at the borehole wall was assumed, thus well pressure was set equal to pore pressure. Stress conditions and well pressure are shown in Table 3.1. Relevant predefined fields and loads were applied in the FEA to simulate these conditions.

Table 3.1: Stress conditions defined in the ABAQUS model.

Vertical stress	30 MPa
Maximum horizontal stress	22 MPa
Minimum horizontal stress	18 MPa
Well pressure	15 MPa

The stress state was implemented through both geostatic stress, which is a predefined load inside the model, and pressure loads applied on surfaces in the ABAQUS model. Geostatic stress was

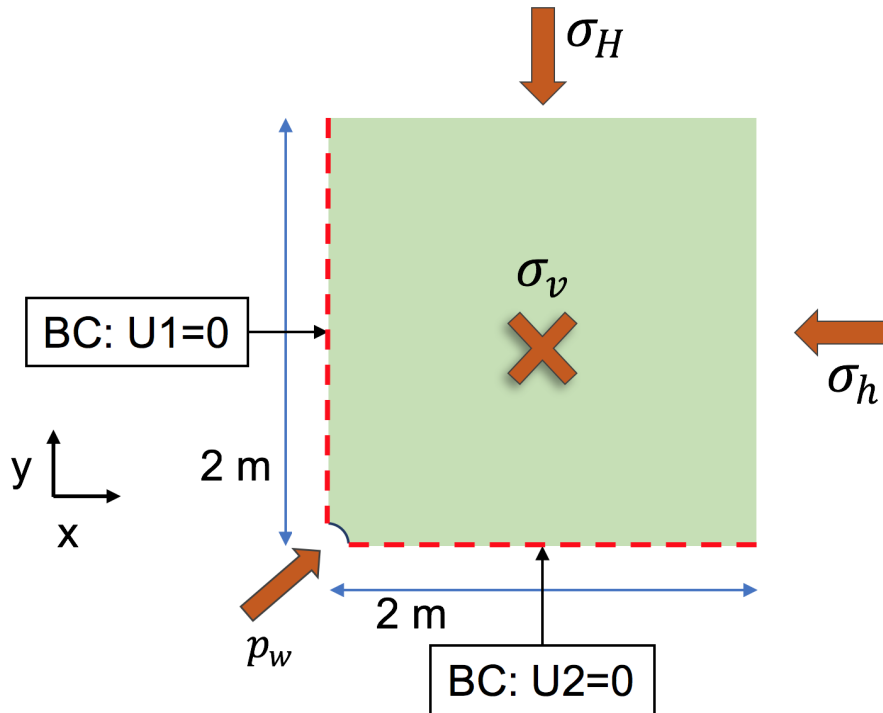


Figure 3.2: Schematic of the model, seen from above, where symmetry conditions have been used to reduce size of model to one quadrant. Dimensions, boundary conditions and direction of stress and pressure are illustrated.

specified with stress magnitudes at the top surface ($z = 1$) and bottom surface ($z = 0$), such that a gradient was set up, which was based on the hydrostatic stress originating from the weight of the material. Two different lateral coefficients were set to describe the anisotropic stress state in the model. Values used in the FEA are displayed in Table 3.2, where it is seen that maximum horizontal stress is in the y -direction. The geostatic stresses describe the initial effective stresses in the model (ABAQUS FEA, 2014). The total stresses and wellbore pressure were modeled by specifying pressure loads at four different surfaces. The magnitude of the pressures are seen in Table 3.1, and the direction and surfaces which the pressures are applied on are shown in Figure 3.2, where the vertical stress is directed into the plane denoted by the X-symbol. To ensure a converging numerical analysis, gravity was applied as a load in the model, such that the geostatic stress and the total stresses comply. Gravity was specified to 9.81 m s^{-1} in the negative z -direction.

Table 3.2: Geostatic stress conditions. Lateral coefficient 1 and 2 refer to x - and y -directions, respectively.

Stress magnitude 1 at $z=1$	-15 MPa
stress magnitude 2 at $z=0$	-15.02 MPa
Lateral coefficient 1	0.2
Lateral coefficient 2	0.47

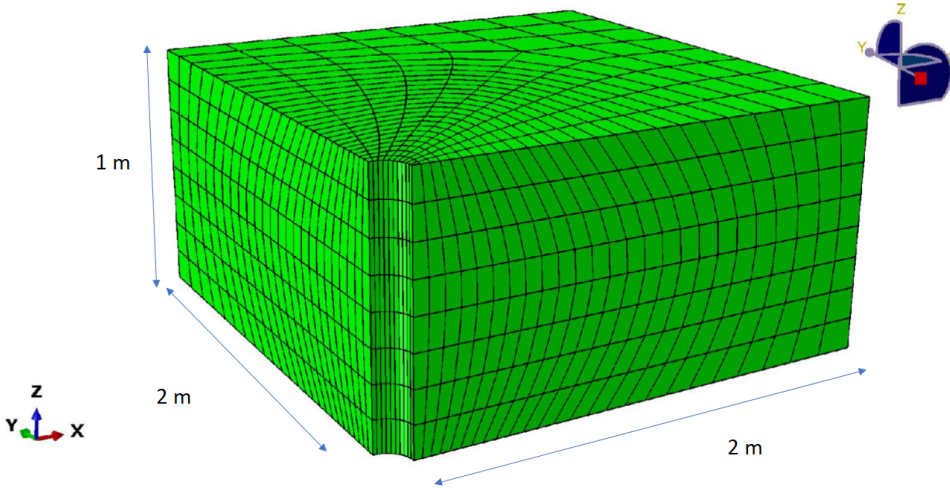


Figure 3.3: Excerpt of the numerical model from the ABAQUS GUI. Modified to show dimensions.

Pore pressure, temperature and void ratio were included as predefined fields and were constant through the entire model at initial conditions. The numerical values used in the model are displayed in Table 3.3. Initial temperature was based on having a geothermal gradient of 2 °C/100m with a surface temperature of 20 °C. The void ratio is discussed in section 3.2.

Table 3.3: Predefined fields in the FEA

Temperature	50 °C
Void ratio	0.33
Pore pressure	15 MPa

The symmetry boundary conditions were defined on appropriate surfaces in the ABAQUS model, where the surfaces were made up of the set of nodes representing the surface in question. The boundary conditions applied in the model are listed below, where U refer to displacement, UR refer to rotational displacement, and the numbers 1, 2 and 3 refers to x , y , z directions, respectively. Table 3.4 show the boundary conditions, and the the nodes defining the surface they apply to.

- XSYMM: Symmetry around the x-axis - $U1 = UR2 = UR3 = 0$
- YSYMM: Symmetry around the y-axis - $U2 = UR1 = UR3 = 0$
- ZSYMM: Symmetry around the z-axis - $U3 = UR1 = UR2 = 0$

Table 3.4: Boundary conditions and surface sets they apply to

Boundary condition	Surface set
XSYMM	nodes in yz-plane at x=0
YSYMM	nodes in xz-plane at y=0
ZSYMM	nodes in xy-plane at z=0
ZSYMM	nodes in xy-plane at z=1

3.1.1 Heating the Borehole

Heating of the borehole was applied through the steps *step-1* and *step-2*. In *step-1* borehole temperature was increased from 50 °C to 200 °C through the course of 5 s. It was used 5 s to ensure sufficient time for the numerical simulation to converge. It is emphasized that 5 s can be an optimistic goal for generating such a temperature increase, however, it was used to mitigate effects originating from the heating process to focus on the effect of having a constant temperature at the borehole wall. The temperature increase defined in *step-1* precedes into *step-2* as a boundary condition with 200 °C at the borehole wall. *Step-2* goes on for 350 000 s, where heat propagates from the wellbore into the material. The analysis was conducted using an ABAQUS input file, which is a text file containing all the data needed to conduct the finite element analysis. The advantage with using input files were that changes could be made quicker than in the ABAQUS GUI, and pore fluid properties could be defined, allowing the development of a porous medium. Heating was defined by Geostatic type steps, which are used in applications with combined heat transfer and pore fluid flow. Thus, a coupled temperature-pore pressure finite element analysis was developed (ABAQUS FEA, 2014).

3.1.2 Development of the Finite Element Analysis

The finite element model was based on a model made by SINTEF petroleum research. The shape, dimensions and mesh were kept the same as SINTEF's FEA, while stress conditions and material parameters were changed to accommodate the conditions described above and the following literature study of shale properties. Additionally, boundary conditions and loads described above were the same, except, SINTEF's model did not include the symmetry boundary condition on the top horizontal surface at $z = 1$. This generated downward displacement at the top of the well and further affected other parameters, which was not in agreement with possible behavior in a petroleum well. The additional boundary condition on the top surface was included through the course of this thesis, and yielded more satisfying results.

3.2 Input Parameters

ABAQUS operates with consistent units in its simulations, thus all input parameters were in SI units. The input parameters were specified in the input file such that material properties were determined for both the matrix and the pore fluid in the FEA such that it represented a porous medium (ABAQUS FEA, 2014). The matrix properties were based on shale properties found in the literature. Since shale formations varies, properties in the model were chosen to resemble a weak shale in terms of strength related parameters. The pore fluid was based on the IAPSO standard seawater, which has the salinity 35 g l^{-1} (Millero et al., 2008). Furthermore, input parameters were assumed independent of temperature influence for simplicity, and for better comparison with the conducted sensitivity analysis, which is described in Section 4.2. The material properties used in the base case are shown in Table 3.5. Input parameters are discussed in the following paragraphs and establish a basis for the sensitivity analysis.

Table 3.5: Material properties used in the finite element analysis

Property	Value
Young's modulus	5.0 GPa
Poisson's ratio	0.33
Bulk modulus of grains	30 GPa
Bulk modulus of fluid	2.4 GPa
Permeability	$5 \times 10^{-14} \text{ m s}^{-1}$
Void ratio	0.33
Friction angle	30°
Dilatancy angle	5°
Cohesion	2.0 MPa
Tension cutoff	2.0 MPa
Absolute plastic strain	0
Shale matrix density	2300 kg/m^3
Pore fluid density	960 kg/m^3
Specific weight of wetting liquid	9400 N/m^3
Linear thermal expansion coefficient of matrix	$2 \times 10^{-5} \text{ K}^{-1}$
Linear thermal expansion coefficient of pore fluid	$2.45 \times 10^{-4} \text{ K}^{-1}$
Thermal conductivity of shale	2.1 W/mK
Thermal conductivity of pore fluid	0.68 W/mK
Specific heat of matrix	900 J K^{-1}
Specific heat of pore fluid	4100 J K^{-1}

3.2.1 Elastic Moduli and Poisson's Ratio

Young's modulus, Poisson's ratio and bulk modulus of grains were based on typical values for weak shale, found in appendix A in Fjær et al. (2008), where drained properties was used in ABAQUS. Temperature effect on bulk modulus of grains is very small, whereas pore fluid bulk

modulus is more influenced by temperature changes. Bulk modulus of seawater varies between approximately 2200 MPa to 2600 MPa for the pressure-temperature conditions in the model (Schön, 2015). It was assumed constant and equal to 2400 MPa in the FEA.

3.2.2 Permeability and Porosity

Permeability for shale formations are typically less than 100 μD , and porosity varies between low values (<5 %) and high values (>30 %) (Schön, 2015). Permeability and porosity is set to 5 nD and 25 % because these values will allow large and accumulating thermally induced pore pressure (Li et al., 1999), which is desired in the model. Permeability has units m s^{-1} in ABAQUS. The relation between permeability in m^2 and m s^{-1} for a porous medium saturated with a single fluid is given in the ABAQUS documentation as (ABAQUS FEA, 2014).

$$k = \frac{\nu}{g} \cdot \hat{k} \quad (3.1)$$

where k is permeability with units m^2 , ν is the kinematic viscosity, g is the gravity constant and \hat{k} is permeability with units m/s . Using equation (3.1) to convert 5 nD yields approximately $5 \times 10^{-14} \text{ m s}^{-1}$, assuming the formation is saturated with seawater.

Similarly, porosity is specified indirectly through void ratio in ABAQUS. Void ratio, e , is a dimensionless property defined as the ratio of void space, V_{void} , to the grain volume, V_m of a porous medium. Void ratio is related to porosity by (Fjær et al., 2008)

$$n = \frac{e}{1 + e} \quad (3.2)$$

which gives a void ratio of 0.33.

3.2.3 Mohr-Coulomb Plasticity Model

The material in the ABAQUS model follows the Mohr-Coulomb plasticity model. The Mohr-Coulomb model is used because it fits very well with experimental data (Li, 1998). It assumes purely elastic behaviour for $f < 0$, and cannot sustain a stress circle that intersects the failure envelope as $f = 0$. Plastic yielding occurs when the material is in a plastic state, $f = 0$, and remains in a plastic state, $\dot{f} = 0$. The failure envelope is made up of the Mohr-Coulomb criterion and tension cutoff, specified by the tensile strength of the material, as illustrated in Figure 2.3. However, the discontinuity between the red and blue failure lines is not applicable for real rocks, where the transition between failure modes is smoother (Fjær et al., 2008). Figure 3.4 is a better representation of the failure envelope in the finite element model because a smooth curve replaces the discontinuity between the tension cutoff and the Mohr-Coulomb criterion.

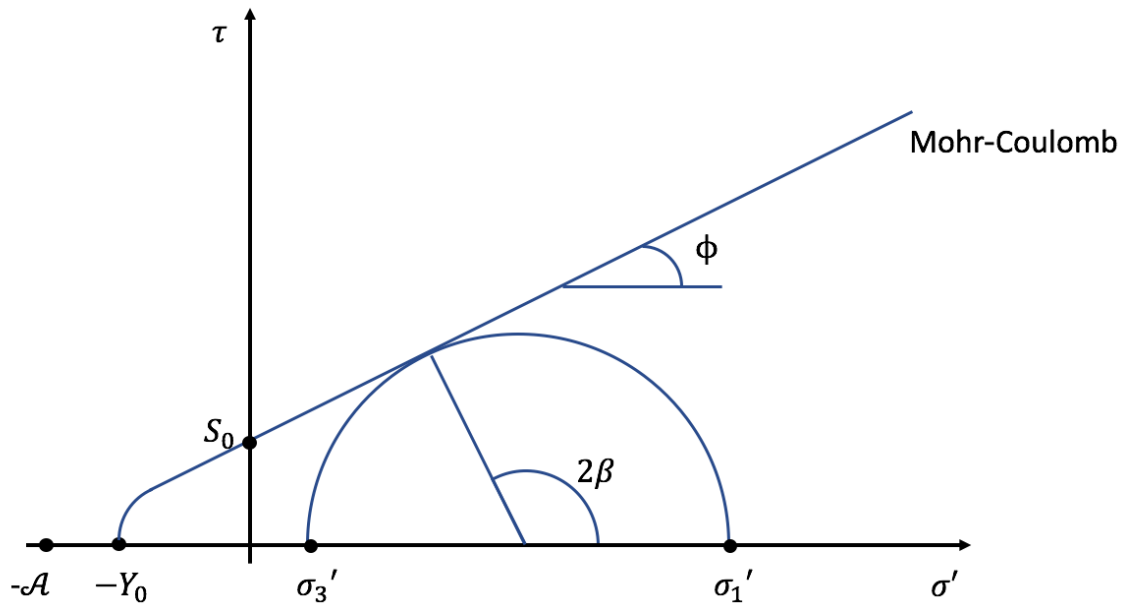


Figure 3.4: Mohr-Coulomb yield criterion in $\tau - \sigma'$ space adjusted for tension cutoff and without discontinuities for modelling. The Mohr circle is drawn, and touches the failure line (inspired by (Fjær et al., 2008, p.62) and (ABAQUS FEA, 2014)).

The Mohr-Coulomb criterion requires a friction angle and cohesion, and the non-associated plastic flow requires the dilatancy angle. The friction angle of shale rocks are typically very low, 10° to 20° , when porosity is large (Fjær et al., 2008), and friction angle increases with decreasing porosity. The porosity in the model was medium range, thus the friction angle was set to 30° . However, some suggest that such a friction angle is the upper bound for clays (Vermeer and de Borst, 1984). Cohesion is calculated from knowing the friction angle. For a weak shale with C_0 equal to 7 MPa (Fjær et al., 2008; Schön, 2015), equation (2.7) yields a cohesion of 2 MPa. Tension cutoff was set to 2 MPa in the model, which is a large tensile strength for a shale formation, however, this value was chosen to focus on shear failure. The dilatancy angle is set to 5° based on an upper bound of lab experiments on different shale facies conducted by Bauer et al. (2017). This dilatancy angle is large based on values presented by Vermeer and de Borst (1984) and small compared to experiments conducted by Ding et al. (2016).

Plastic behaviour of the material is described by specifying the absolute plastic strain occurring at a given loading situation. The material is assumed to behave according to an ideally plastic material. Thus absolute plastic strain is set to zero for the cohesion and the tension cutoff values in the model. This ensures onset of plastic strain when $f = 0$, and since no hardening or softening parameters are defined f is unchanged such that ideally plastic behavior occurs, as illustrated in Figure 2.5.

3.2.4 Density

Density of the material is described by the matrix and pore fluid independently. Matrix density of shale formations depends on elemental composition of the minerals within the rock (Schön, 2015). Matrix density is assumed independent of temperature and pressure, and is 2300 kg/m^3 in the model (Fjær et al., 2008). On the other hand, seawater density depends on salinity, pressure and temperature, however the density is not very pressure dependent since seawater is nearly incompressible (IAPWS-IF97, 2012; Kretzschmar et al., 2008, 2013). It is assumed zero osmotic diffusion between borehole and formation, thus salt concentration is constant in the pore fluid. Calculations within the pressures and temperatures relevant to the finite element analysis confirms that density is dominated by temperature change relative to pressure change (Kretzschmar et al., 2013). Figure 3.5 show seawater density as a function of temperature with pressure constant at 16 MPa, calculated using Kretzschmar et al. (2013) and a sample spacing of 2.5°C . It is observed that seawater density decreases with increasing temperature almost linearly, and at approximately 140°C the slope of the seawater density become more negative. This might be caused by conditions entering a region with slightly different governing equations, however this is unknown due to the black box calculation in Kretzschmar et al. (2013). Average density for temperatures 50°C to 200°C is 960 kg/m^3 , which was used as pore fluid density in the FEA. The average pore fluid density was also used to calculate the specific weight of the wetting fluid in Table 3.5.

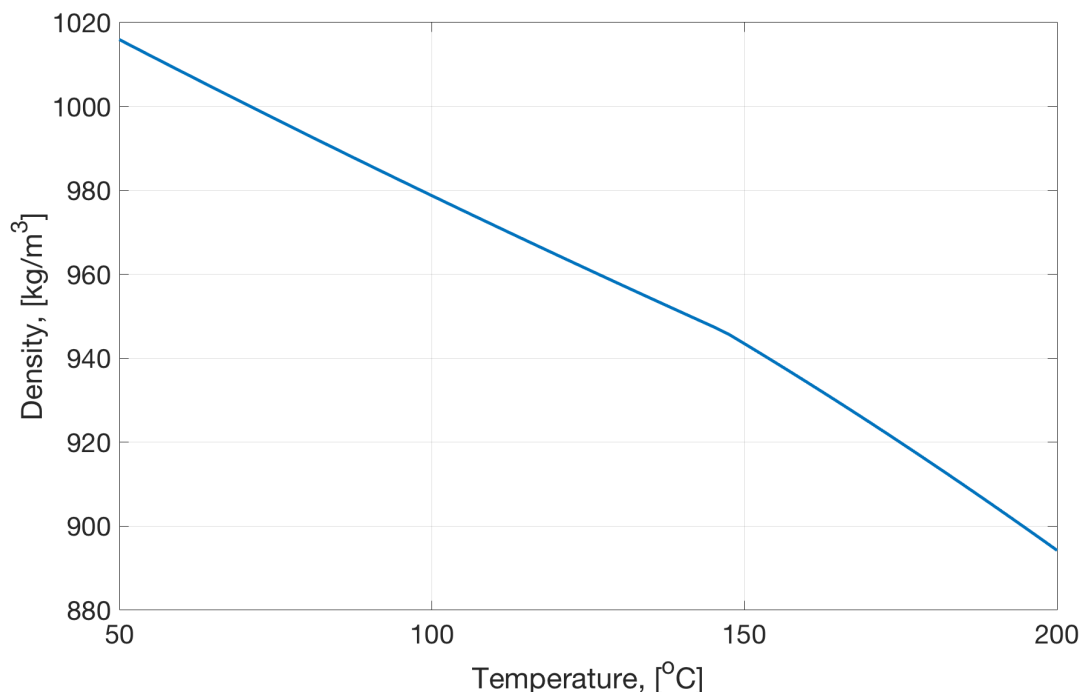


Figure 3.5: Density of seawater vs. temperature. Salinity=35g/l, p=16 MPa (Kretzschmar et al., 2013).

3.2.5 Thermal Expansion Coefficient

Temperature dependence of thermal expansion coefficient of shale is not discussed in detail in the literature (Fjær et al., 2008; Somerton, 1992; Schön, 2015), thus it is assumed independent of temperature. Linear thermal expansion coefficient of shale is reported between $10 \times 10^{-6} \text{ K}^{-1}$ to $20 \times 10^{-6} \text{ K}^{-1}$ for different shale formations (Fjær et al., 2008), and the largest value is used in the model.

Volumetric thermal expansion is given by (Serway and Jewett Jr, 2010, p. 550)

$$\alpha_V = \frac{1}{V} \left(\frac{\partial V}{\partial T} \right)_p \quad (3.3)$$

where V is volume. Seawater density in Figure 3.5 has a non-linear slope in the temperature region applicable in the finite element analysis, thus volumetric thermal expansion coefficient will also vary, seen from equation (3.3). By rewriting equation (3.3) to be expressed in terms of density, and applying the relation in equation (2.21), linear thermal expansion is given by

$$\alpha_L = -\frac{1}{3} \frac{1}{\rho} \left(\frac{\partial \rho}{\partial T} \right)_p \quad (3.4)$$

where ρ is density. The blue line in Figure 3.6 show the linear thermal expansion coefficient of seawater calculated with equation (3.4) based on the data from Figure 3.5. As a reference point, linear thermal expansion coefficient for pure water is also shown by the green line in Figure 3.6. Thermal expansion of water shows a linear trend with increasing temperature, whereas saltwater is approximately constant for $T < 140$, and is linearly increasing for $T > 150$. The difference between thermal expansion coefficient between water and seawater is significant, and shows the importance of using seawater parameters in the finite element analysis.

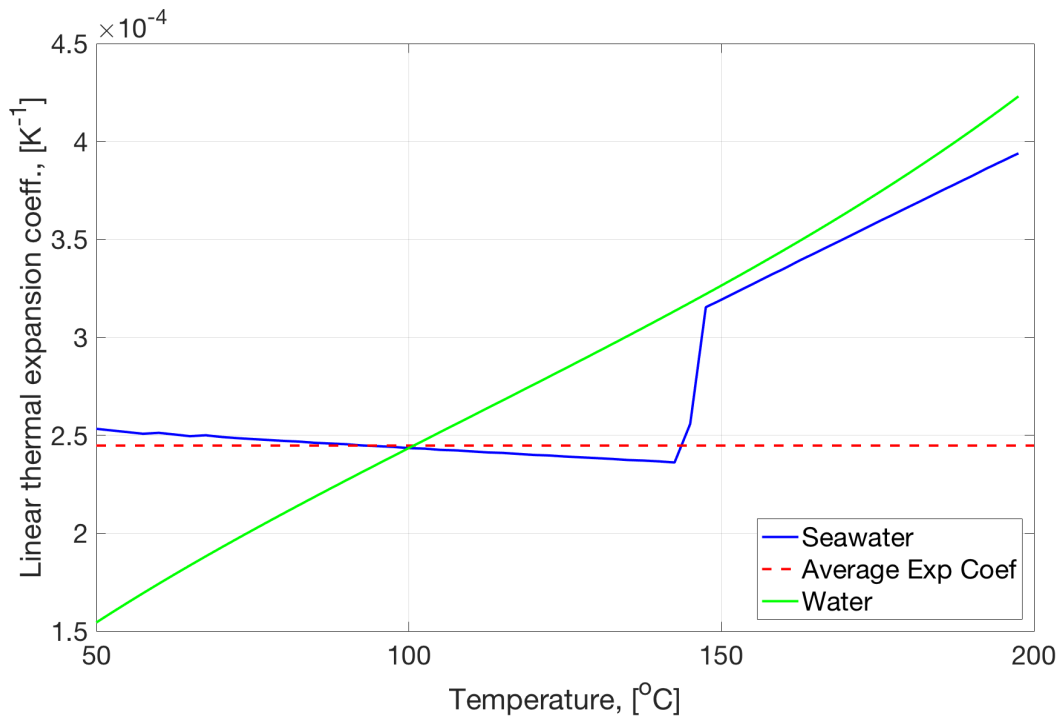


Figure 3.6: Linear thermal expansion coefficient for water (green) and seawater (blue). The stippled red line is the average value of seawater between 50 °C to 140 °C

Thermal expansion coefficient between 50 °C to 140 °C is almost constant. An average thermal expansion coefficient in this temperature range is plotted as a stippled red line in Figure 3.6, and shows that the error of using this average value is very small. Furthermore, Figure 2.9a shows that temperature increase inside the formation is very slow, hence only parts of the model very close to the borehole wall will experience temperatures above 140 °C. Thus the average thermal expansion coefficient displayed by the stippled red line is a good approximation overall, and was used in the ABAQUS FEA.

3.2.6 Thermal conductivity

Thermal conductivity of a liquid-saturated formation depends on thermal conductivity of the dry rock and the liquid, additionally physical properties of the rock has an effect (Somerton, 1992). The input file in ABAQUS allows specification of conductivity of the shale matrix and the pore fluid independently. Table 3.6 shows conductivity of seawater with salinity 35 g L⁻¹. The temperatures displayed in the table include the majority of temperatures in the ABAQUS simulation, and it is observed that conductivity variation with temperature is relatively small. The average value 0.676 ≈ 0.68 W/mK was used in the model.

Thermal conductivity of shale varies, but a mean value of 2.07 W/mK is presented by Schön (2015), based on 377 shale samples. The thermal conductivity of a porous medium is given by

(Evans, 1977)

$$\lambda_b = \lambda_f^\phi \cdot \lambda_m^{1-\phi} \quad (3.5)$$

where λ_b , λ_f and λ_m are thermal conductivity of the bulk rock, pore fluid and rock matrix, respectively. With 0.68 W/mK for seawater, equation (3.5) yields a thermal conductivity of 1.57 W/mK for the formation fluid system. This value is in line with the conductivity values for saturated shale formations at elevated pressures in Fjær et al. (2008), confirming that (2.07≈)2.1 W/mK is an appropriate thermal conductivity value for the shale matrix.

Table 3.6: Conductivity of seawater (Jamieson and Tudhope, 1970)

Temperature °C	Conductivity mW/mK
60	649
80	666
100	678
120	685
140	688
160	686
180	681

3.2.7 Heat Capacity

Heat capacities for several rock matrices as a function of temperature are shown graphically in Figure 3.7. Heat capacity of shale show a linear trend between 50 °C and 200 °C. These values are extracted and shown in Table 3.7. The average heat capacity in this temperature range is 900 J/kgK, and is used in the ABAQUS model.

At the pressure-temperature conditions simulated in the finite element analysis, seawater remains within its liquid state. Change in isobaric heat capacity of seawater is very small for different pressures relevant in the model, and is therefore assumed independent of pressure change (Kretzschmar et al., 2013). Isobaric heat capacity of seawater and water are shown graphically in Figure 3.8. The heat capacities are calculated based on IAPWS-IF97 (2012) for water and Kretzschmar et al. (2013) for seawater, where pressure is constant and equal to 16 MPa. The seawater has a lower heat capacity than water, which is another argument for using seawater properties in the model. At approximately 140 °C, the slope of the seawater increases. Like in Figure 3.5 it might be caused by p-T conditions entering another set of governing equations. Numerical values for heat capacity of seawater are shown in Table 3.7, and the average value, (4118 J/kgK≈)4100 J/kgK is used in the finite element analysis.

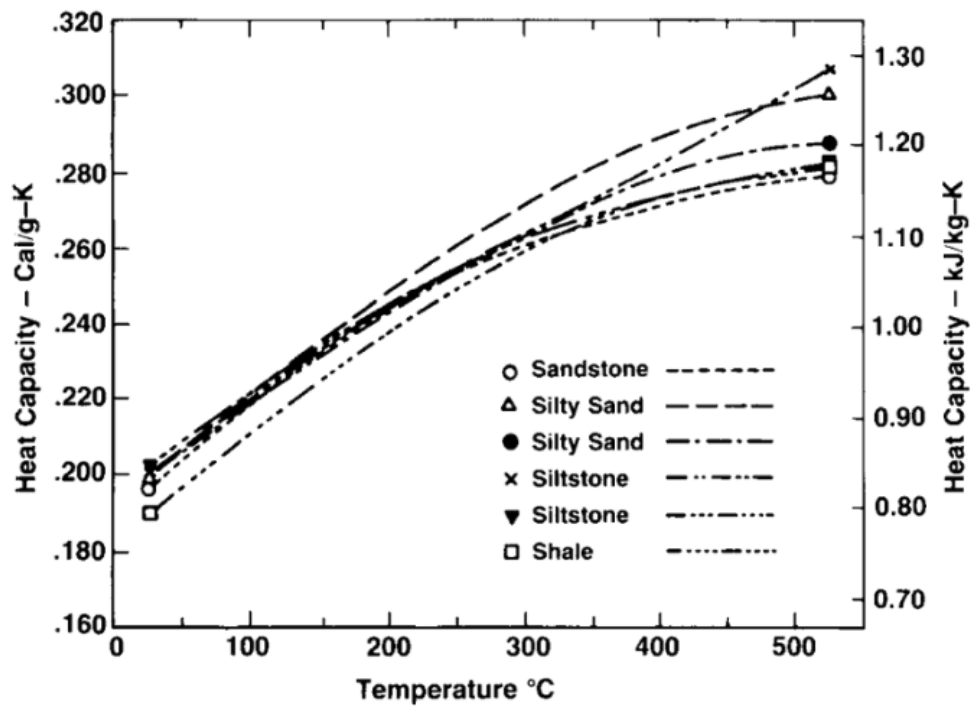


Figure 3.7: Experimental heat capacity of rocks as a function of temperature (courtesy (Somerton, 1992, p. 11))

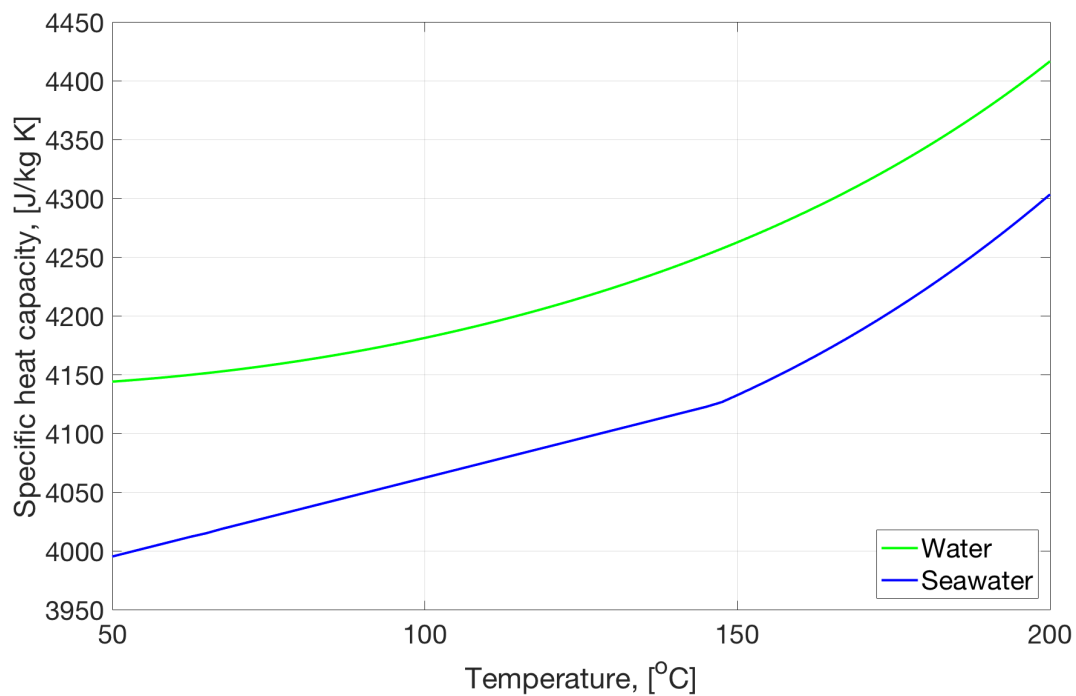


Figure 3.8: Calculated heat Capacity of seawater (blue) and water (green) as a function of temperature. Pressure=16 MPa

Table 3.7: Heat capacity of shale matrix and seawater at different temperatures

Temperature °C	Matrix heat capacity J/kgK	Seawater heat capacity J/kgK
50	810	3996
75	840	4029
100	870	4063
125	900	4096
150	930	4133
175	960	4205
200	990	4304

Chapter 4

Approach

4.1 Data

The analysis was based on results from the ABAQUS FEA simulations. Output parameters in ABAQUS are calculated for every iteration in the simulation. The iterations do not have a constant time step, thus neither do the output parameters. Furthermore, output parameters are given at all nodes in the finite element analysis. These are displayed graphically in the ABAQUS GUI as color coding onto the 3D model. The following list of output parameters is studied in the analysis.

- Temperature
- Pore pressure
- Radial strain
- Radial plastic strain
- Radial Displacement
- Stress components: radial, tangential and axial
- Void ratio

A path was created to plot the data as a function of radial distance. To minimize potential boundary effects it was placed diagonally in the middle of the model with Cartesian coordinates $(x = 0, y = 0, z = 0.5)$ to $(x = 2, y = 2, z = 0.5)$. Output parameters were exported for every 20th increment, located on the path with samples every 1 cm, which allowed evaluation of parameters as a function of time and distance from the borehole wall. ABAQUS uses the open-source scripting language Python, and a Python script was created to automate extraction of data into txt-files with a list of x - and y -data, where y -values are the parameter evaluated and x -values are the distance on the path. Additionally, three nodes on the borehole wall were

extracted to evaluate radial displacement with time. The nodes are depicted in Figure 4.1, with coordinates shown in the caption, and were selected to display possible anisotropy effects. The txt-files were loaded into a database in MATLAB for analysis. This was useful because a comparison between parameters in different cases was easier, and data assessment, such as calculating derivatives, was possible.

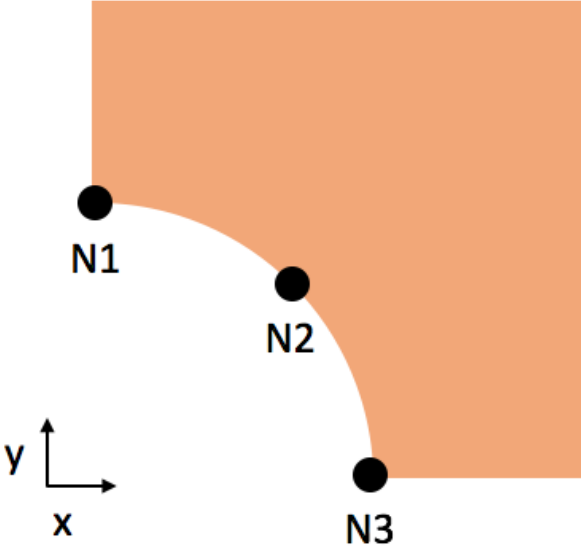


Figure 4.1: Nodes at the wellbore where displacement is evaluated over time. $N1=(x = 0, y = 0.1, z = 0.5)$, $N2=(x = 0.0707, y = 0.0707, z = 0.5)$ $N3=(x = 0.1, y = 0, z = 0.5)$

4.2 Sensitivity Analysis

In addition to the base case described in Section 3.2, six additional cases were simulated, and are listed below. Each of the cases was based on the base case where one parameter or condition was changed. Comparison between the base case and the variation cases were examined to better understand important mechanisms for providing deformation that lead to a sealing barrier.

1. Case 2: Elastic parameters only

The following input parameters related to the Mohr-Coulomb yield criterion were removed from the model.

- Cohesion
- Absolute plastic strain
- Friction angle
- Dilatancy angle
- Tension cutoff

2. Case 3: Reduced Pore pressure and well pressure

To accommodate these changes some of the initial and boundary conditions were changed according to the setup of the base case in Section 3.1. The values were specified to:

- $p_f = 10 \text{ MPa}$
- $p_w = 10 \text{ MPa}$

3. Case 4: Higher dilatancy angle

- $\psi = 15^\circ$

4. Case 5: Lower permeability

- $\hat{k} = 1 \times 10^{-16} \text{ m/s}$

5. Case 6: Reduced Thermal expansion coefficient of matrix

As described in Section 3.2 linear thermal expansion coefficient of shale matrix is in the range $10 \times 10^{-6} \text{ K}^{-1}$ to $20 \times 10^{-6} \text{ K}^{-1}$, and the lower value was chosen in this case:

- $\alpha_{L,m} = 10 \times 10^{-6} \text{ K}^{-1}$

6. Case 7: Temperature dependent variables

From the discussion in Section 3.2 it is evident that many of the input parameters are temperature dependent, however, they were assumed independent of temperature to isolate the effect of changing the variables. Case 7 includes temperature dependency to study the effect of assuming temperature independent variables. The Temperature dependent parameters and their values are described in the list below

- Pore fluid density, according to table 4.1
- Linear thermal expansion coefficient of pore fluid, according to table 4.2
- Specific heat capacity of pore fluid and matrix, according to table 3.7

ABAQUS assumes a linear relation between the data points in the tables, which is a good approximation seen from the discussion in Section 3.2. The remaining parameters are assumed independent of temperature similar to the base case in table 3.5

Table 4.1: Pore fluid density for different temperatures used in case 7, calculated from Kretzschmar et al. (2013)

Density kg/m ³	Temperature °C	Density kg/m ³	Temperature °C
1016	50	∴	∴
1008	60	958	130
1000	70	951	140
993	80	943	150
985	90	934	160
979	100	925	170
972	110	915	180
965	120	905	190
∴	∴	894	200

Table 4.2: Linear thermal expansion coefficient of pore fluid for different temperatures used in case 7. The same values as in Figure 3.6

$\alpha_{L,f}$ 10 ⁻⁴ K ⁻¹	Tempearture °C
2.53	50
2.36	140
3.20	150
3.94	200

4.3 Sealing Potential

4.3.1 The Geomechanical Concept

Heating the borehole wall will set up a transient temperature profile into the formation around the borehole, consequently, pore pressure and earth stresses are expected to increase. Assuming pore pressure increase is more important than the change in earth stresses, effective stresses will reduce and shift the Mohr circle towards the failure envelope, which eventually causes the formation to yield, resulting in plastic deformation. The aim is to study the induced deformation caused by increasing temperature in a material similar to that of a shale and evaluate the sealing potential based on the magnitude of radial deformation into the wellbore.

4.3.2 Temperature Effects on Pore pressure and Earth Stress

Pore pressure and earth stresses increase with temperature. The FEA assumes plane strain conditions, hence, change in earth stresses are calculated by equations (2.35) and (2.36), for horizontal and vertical earth stress respectively, and show that the relation between stress and temperature change is given by

$$\frac{\Delta\sigma_v}{\Delta T} = c'_v = \frac{\alpha_{L,m}E}{1-\nu} \quad (4.1)$$

$$\frac{\Delta\sigma_h}{\Delta T} = c'_h = \frac{1}{2}c_v \quad (4.2)$$

where c'_v and c'_h are coefficients for vertical and horizontal stress respectively.

The coupling coefficient c' in equation (2.27) give the relation between temperature and pressure change and is calculated from equation (2.31). Unfortunately, ABAQUS does not include undrained Poisson's ratio, such that c' can not be calculated analytically like Chen and Ewy (2005) describes. However, the coupling coefficient can be estimated indirectly by finding the relation between pressure and temperature through

$$c' = \frac{\frac{\partial p}{\partial t}}{\frac{\partial T}{\partial t}} \approx \frac{p_{i+1} - p_{i-1}}{T_{i+1} - T_{i-1}} \quad (4.3)$$

where numerical differentiation approximation is used, and subscript i refers to increments in the simulation. This relation is only applicable in a purely elastic region, and where diffusion is so low that it is possible to decouple equations (2.26) and (2.27). The pressure-temperature relation in equation (4.3) was estimated based on data from the ABAQUS simulations.

4.4 Hypotheses

Hypotheses regarding the analyses were made in advance of viewing and interpreting results to reduce confirmation bias, and expose potential errors when producing the results. Hypotheses and reasoning for expectations related to the analyses are described below.

4.4.1 Predictions for the Sensitivity Analysis

Hypotheses were formulated for the sensitivity analysis regarding general behavior and how displacement at the borehole wall compares with the base case. The hypotheses are discussed separately for each of the cases and the predictions with respect to displacement are summarized in Table 4.3.

Table 4.3: Prediction whether displacement at the borehole wall in the sensitivity analysis will be higher or lower compared to the base case

Case	Higher	Lower
2		X
3	X	
4		X
5	X	
6	X	
7	X	

4.4.1.1 Case 2: Elasticity

All strains are elastic and based on Hooke’s law, such that displacement at the borehole wall is expected to be small compared to the base case. Without a yield criterion there will not be any constraints regarding stresses or pore pressure, and if thermally induced pore pressure is very large it is expected that strain will be notable, although not sufficient to form a barrier.

4.4.1.2 Case 3: Reduced Pore Pressure and Well Pressure

In case 3 pore pressure and well pressure is reduced which lead to a larger stress concentration around the borehole. Mohr circles at the borehole wall for case 1 and 3 are compared in Figure 4.2, where the cyan and red Mohr circles represent case 1 and 3, respectively, and assume linearly elastic stress conditions. At the borehole wall, effective radial stress is zero in case 1 and 3, while maximum principal stress was the maximum of equations (A.2) and (A.3), which yield a larger Mohr circle in case 3. When including the yield criterion, seen by the diagonal blue line

in Figure 4.2, both Mohr circles become inaccessible with respect to the failure envelope, and since both cases must have zero effective radial stress on the borehole wall, both Mohr circles develop into the green circle in Figure 4.2, where maximum effective stress is calculated using equation (2.8). Because case 3 has a larger elastic Mohr circle than case 1, case 3 has greater potential for yielding which is expected to result in more plastic deformation. Furthermore, this tendency was expected to persist into the formation close to the borehole. Consequently, more displacement was expected at the borehole than the base case.

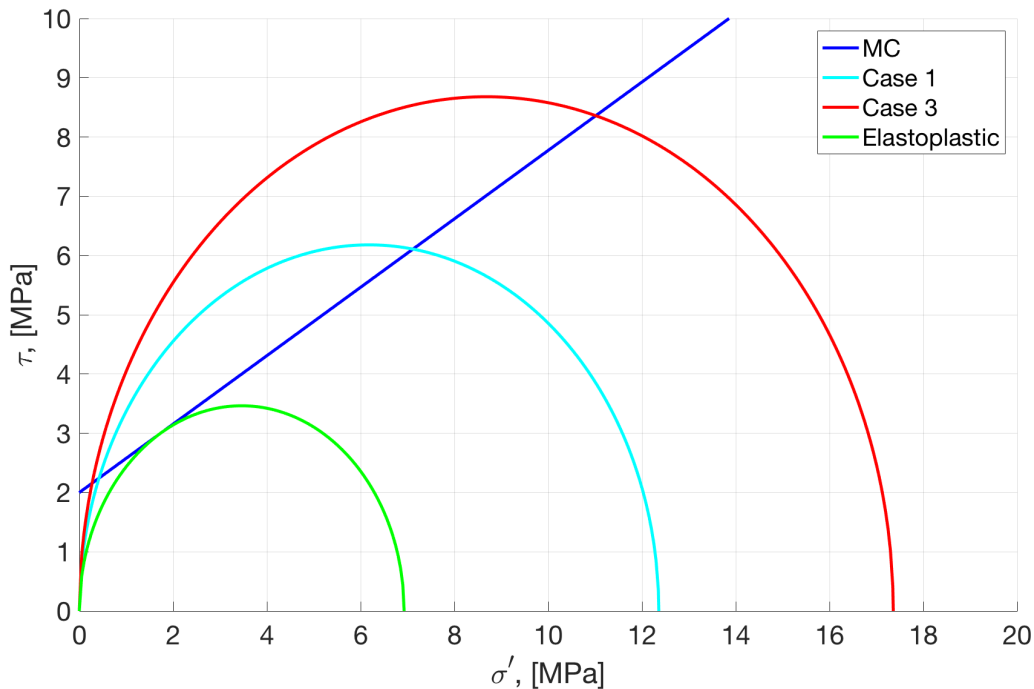


Figure 4.2: Mohr circles for case 1 and 3 at the borehole wall, in direction $\theta = 0$, for a linearly elastic formation compared with the failure envelope. Both case 1 and 3 are represented by the green Mohr circle when the yield criterion is included.

4.4.1.3 Case 4: Higher Dilatancy Angle

When the model reaches its yield criterion dilation was expected to be larger, and lead to more pore volume increase. This should be observed by a larger void ratio in case 4. Larger pore volume counteracts thermally induced pore pressure, which in turn will lead to less plastic deformation. On the other hand, more dilation implies more volume which would displace into the well. However, the former effect is expected to be dominant leading to less displacement at the borehole wall in case 4.

4.4.1.4 Case 5: Lower Permeability

The expected effects from reducing permeability were lower hydraulic diffusion and more accumulation of pore pressure. More pore pressure is expected to be accumulated close to the borehole, leading to more yielding in this zone. With increasing distance from the well, less pore pressure was expected because there would be less contribution from hydraulic diffusion and less yielding would materialize in this zone. Assuming the accumulated pore pressure will lead to more yielding, it was expected that case 5 has more displacement at the borehole wall than case 1. Although a large difference is not expected since permeability in case 1 is already very low.

4.4.1.5 Case 6: Reduced Thermal Expansion Coefficient of Matrix

When thermal expansion coefficient is lower temperature influence on earth stress is also lower. From equations (4.1) and (4.2) it was observed that increase in earth stresses is proportional to the thermal expansion coefficient of the matrix such that temperature influence on earth stresses in case 6 are half of that in case 1. Thus, pore pressure change was expected to be more dominant in case 6 leading to more plastic deformation and displacement at the borehole wall.

4.4.1.6 Case 7: Temperature Dependent Parameters

Specific heat capacity of both pore fluid and matrix increase with temperature. Low specific heat leads to faster temperature increase and the opposite for high specific heat. Specific heat capacity in case 1 was based on an average over the relevant temperature window in the model, which causes lower specific heat capacity in case 7 in the zone where the temperature front is. This effect was expected to lead to faster temperature propagation than in case 1.

The linear thermal expansion coefficient of pore fluid in case 1 is the red stippled line in Figure 3.6, while case 7 is represented by the blue line. For low temperatures, case 7 yields nearly the same value as in case 1, whereas for large temperatures case 7 yields a larger value, which make the average linear thermal expansion coefficient in case 7 larger than in case 1. Areas with high temperatures will have larger specific heat capacities that cause a slower temperature increase, but the linear thermal expansion coefficient of the pore fluid will also be much larger and potentially overcome this effect. Change in pore fluid density is in line with thermal expansion and was not expected to cause any significant effects beyond those mentioned above.

Based on the proposed behavior, more plastic deformation was expected, and thus, more displacement at the borehole wall. In the far away field, lower specific heat leads to more increase in temperature and pore pressure, and close to the borehole more pore pressure increase was expected due to larger thermal expansion coefficient of the pore fluid.

4.4.2 Stress Anisotropy Influence on Displacement

The stress concentration surrounding the borehole vary with the θ -direction due to differences in horizontal stresses. Figure 4.3 depict Mohr circles in the $\theta = 0^\circ$ and 90° directions on the borehole wall. They were calculated based on stress conditions in the base case and a linearly elastic formation, where maximum and minimum principal effective stress was found through equations (A.1), (A.2) and (A.3) and the condition in equation (2.9). The diagonal line represents the yield criterion in the FEA, and indicate that both Mohr circles represent inaccessible stress conditions. Moreover, the Mohr circle in $\theta = 90^\circ$ is larger, demonstrating that the potential for plastic deformation is highest in this direction. The difference between the Mohr circles was largest on the borehole wall, and with distance away from the borehole it decrease and approach zero in the far away field. Consequently, it was expected more displacement in the $\theta = 90^\circ$ -direction.

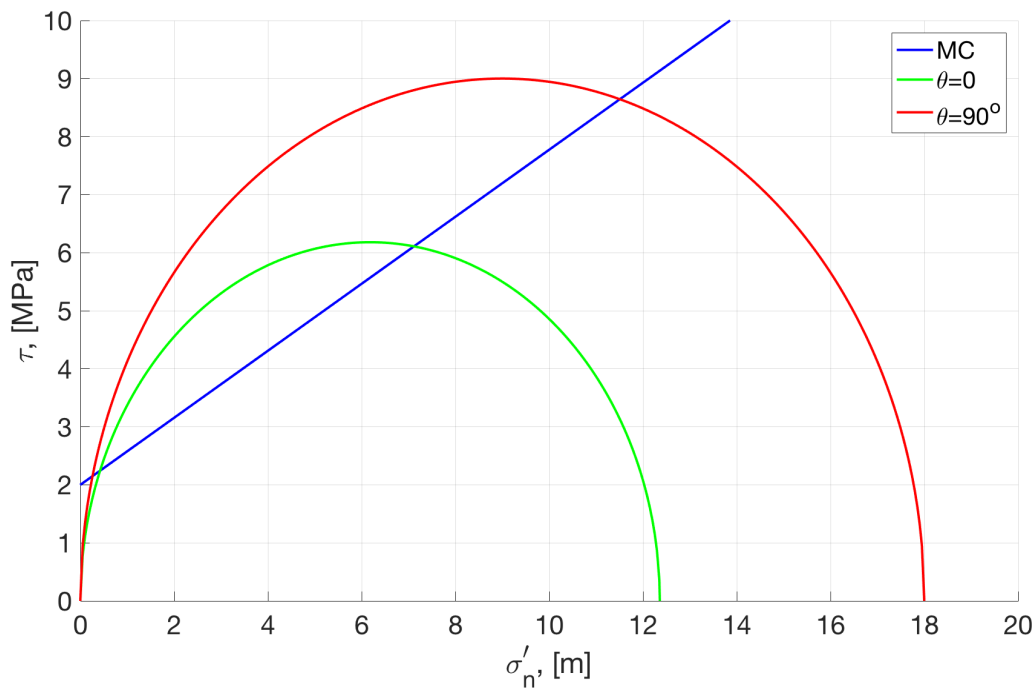


Figure 4.3: Mohr circles displaying stress conditions in $\theta = 0^\circ$ and 90° on the borehole wall for case 1. The Mohr circles are calculated from equation (A.1), (A.2) and (A.3). The diagonal line represents the yield criterion in the FEA.

4.4.3 Pressure-Temperature Relation

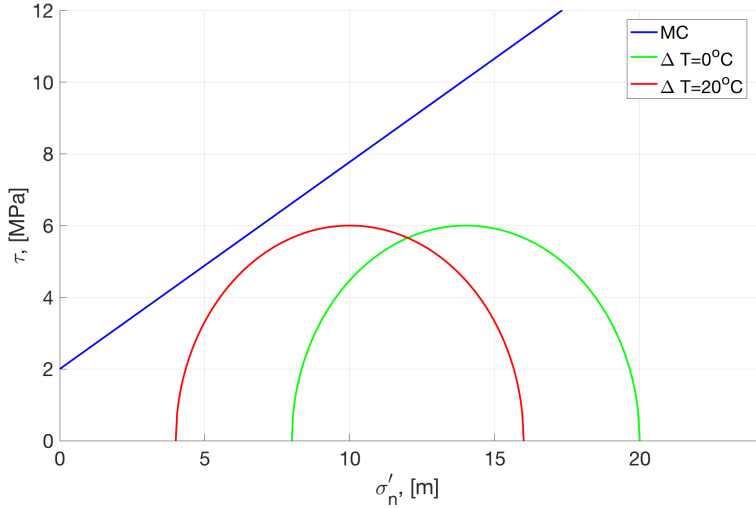
Chen and Ewy (2005) introduces thermally induced pore pressure for a shale formation at 1219.2 mTVD with $c' = 0.31 \text{ MPa } ^\circ\text{C}^{-1}$ found analytically. Bauer et al. (2017) performed experiments on core plugs from four different shale facies that were heated with undrained triaxial stress

state conditions. Pore pressure change relative to temperature increase was estimated to be $0.07 \text{ MPa } ^\circ\text{C}^{-1}$ to $0.22 \text{ MPa } ^\circ\text{C}^{-1}$. Albeit, the total stress acting on the samples were held constant, thus, change in earth stresses were excluded, ignoring the Skempton B effect on pore pressure, implying that the pressure-temperature relation is likely to be higher. Additionally, stress conditions in these experiments reached the failure envelope resulting in plastic deformation and expanding core plugs, which counteracts pore pressure increase. The expected pressure-temperature relation in the FEA was assumed to be similar to those presented by Chen and Ewy (2005); Bauer et al. (2017), and a moderate value of $c' = 0.2 \text{ MPa } ^\circ\text{C}^{-1}$ was used as a prediction. Furthermore, coefficients for change in earth stresses were calculated using equations (4.1) and (4.2) with values in Table 3.5, giving $0.15 \text{ MPa } ^\circ\text{C}^{-1}$ and $0.075 \text{ MPa } ^\circ\text{C}^{-1}$, respectively.

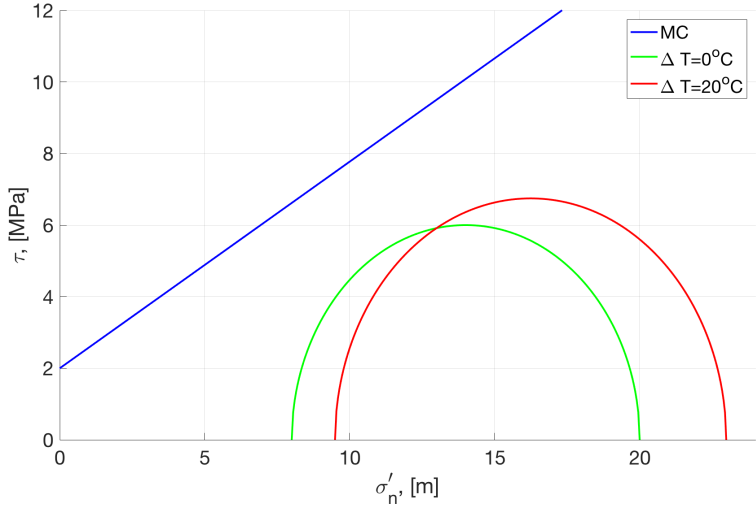
4.4.4 Proximity to Failure

The aforementioned coupling coefficient for pore pressure and coefficients for vertical and horizontal stresses are put into context in Figure 4.4, where the effect of 20°C temperature increase on stress conditions in the far away field is illustrated using Mohr circles, with an initial pore pressure 10 MPa and stress conditions as in Table 3.1. The isolated effect on pore pressure is seen in Figure 4.4a, where the Mohr circle shifts to the left because the change in minimum and maximum principal effective stress reduce the same amount. Earth stress increase is displayed in Figure 4.4b, where the Mohr circle shifts to the right because stresses increase, and the radius grows because vertical stress increases more than horizontal stress. Both effects are shown in Figure 4.4c where the Mohr circle grows in size and moves to the left because pore pressure change is larger than stress change. A similar tendency was expected to develop in the FEA, where the Mohr circle shifts towards the failure envelope while growing in size, which leads to a greater potential for plastic deformation.

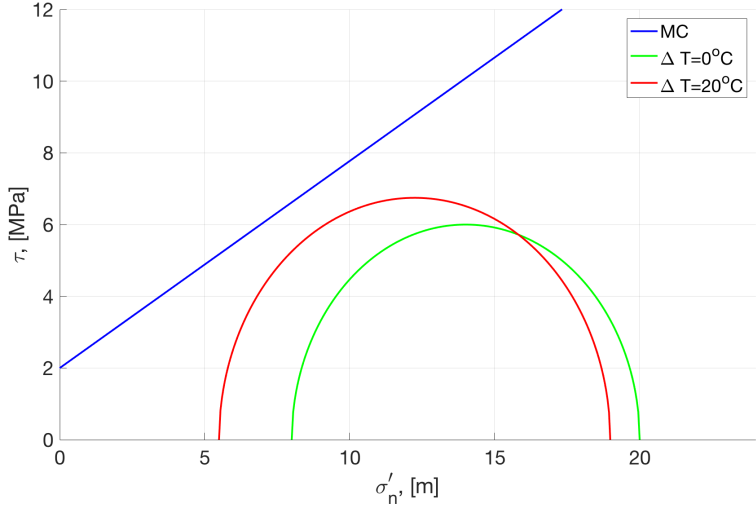
Stress conditions in the model change with radial distance from the borehole, such that the required change in temperature to reach the failure envelope varies with distance. Proximity to failure, with respect to the yield criterion, is the required change of a parameter to cause the Mohr circle to intersect with the failure envelope. Proximity to failure for the base case is illustrated by the blue graph in Figure 4.5, showing how much pore pressure change is required for the Mohr circle to intersect the failure line as a function of distance in the $\theta=0^\circ$ direction. It is calculated based on increasing pore pressure incrementally until the Mohr circle intersects the failure line. Maximum and minimum effective stresses are based on equations (A.1), (A.2) and (A.3) with the relation in equation (2.9). Proximity to failure is zero at the borehole wall, with distance it increases rapidly to a maximum value at $r = 0.18 \text{ m}$ from the borehole wall, and a slower decrease until a constant value is reached is observed beyond the maximum. The zone with the constant value represent the far away field, which is unaffected by the stress redistribution. The required increase in pore pressure is generally small, indicating that the



(a) Only pore pressure is affected by temperature



(b) Only stresses are affected by temperature



(c) Both stresses and pore pressure are affected by temperature

Figure 4.4: Temperature effects on pore pressure and total stress shown isolated and in combination by Mohr circles and relative to the Mohr-Coulomb yield criterion in $\tau - \sigma$ space. $p_f = 10$ MPa and stress conditions are the same as in table 3.1

stress state in the base case is already close to the failure envelope, leaving a large potential for plastic deformation if temperature increase leads to large pore pressure increase. The peak at $r = 0.18$ m implies that the base case would be less receptive to shear failure in this area close to the borehole than in the far away field. Furthermore, the graph shows that failure is already occurring close to the borehole, which is in agreement with the Mohr circles in Figure 4.3 and 4.2. This occurs due to the change in stress concentration due to drillout, and is normal in petroleum wells. The result is usually a more ovally shaped borehole (Fjær et al., 2008).

The proximity to failure graph was based on pore pressure increase, however, the effect of temperature change was included in the upper right corner by the use of the Mohr-Coulomb criterion at radii 0.18 m and 1 m to illustrate the effects close to the borehole in the stress concentration zone, and in the far away field. The previously assumed temperature relation for stresses and pore pressure was used to calculate the change in the Mohr circles and resulted in the required temperature increase $10\text{ }^{\circ}\text{C}$ at the peak, and $3\text{ }^{\circ}\text{C}$ in the far away field. The expected temperature profile was based on Figure 2.10, where the temperature is large at the borehole wall and rapidly decreases into the formation. Thus, it was expected that the temperature near the borehole would be much greater than $10\text{ }^{\circ}\text{C}$, and that parts of the far away field would experience more than $3\text{ }^{\circ}\text{C}$ increase through 4 days of heating. Consequently, substantial plastic deformation was expected near the borehole, and to some extent beyond the initial stress concentration, therefore, notable displacement was expected into the borehole.

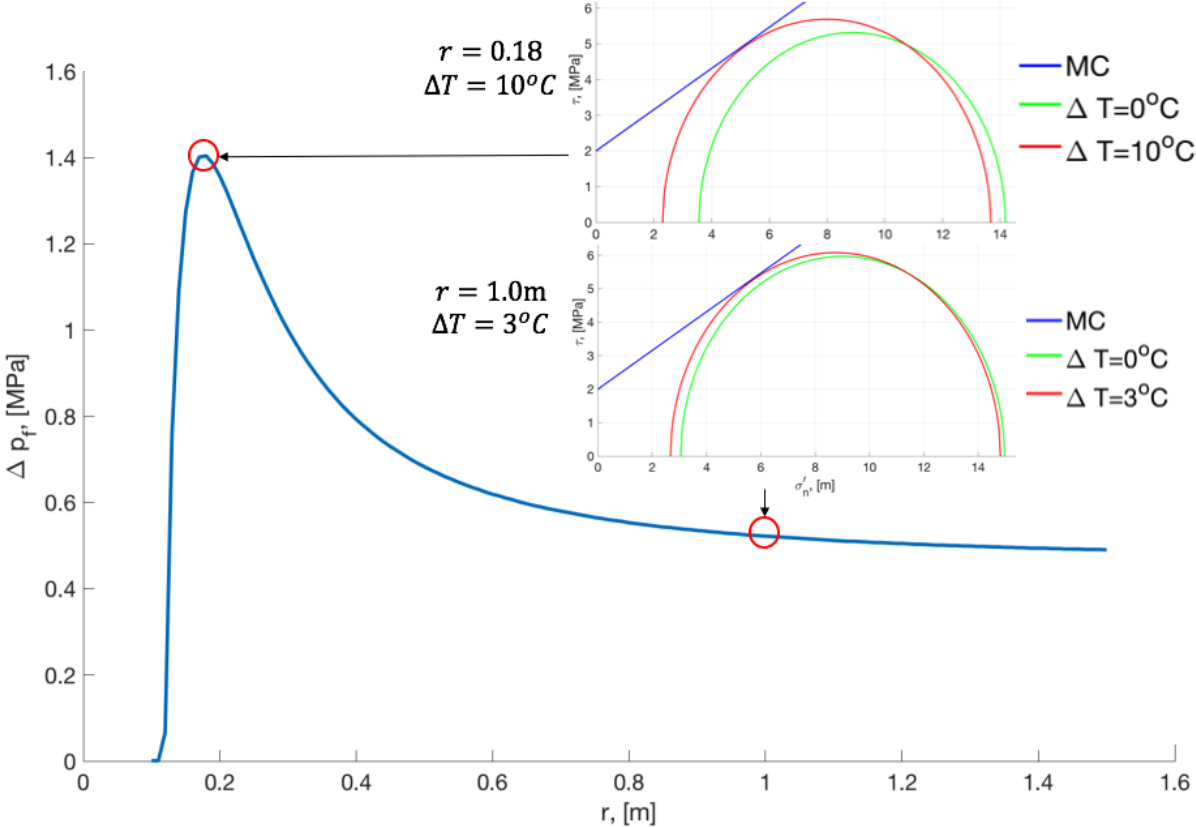


Figure 4.5: Proximity to failure with respect to pore pressure increase in direction $\theta=0^\circ$. Mohr circles in the upper right corner display evaluation of temperature effects at $r = 0.18$ m and 1.0 m

Chapter 5

Results and Discussion

5.1 Output Parameters from the Simulations

The six figures, 5.1-5.6, display temperature, radial displacement, pore pressure, void ratio, radial strain, and radial plastic strain resulting from simulating the base case in ABAQUS FEA. The parameters are shown as a function of distance along the diagonal path, where zero on the x-axis is on the borehole wall. Three increments at 2 h, 24 h and 97.2 h are plotted to illustrate development through time. The following paragraphs describe the behavior of these parameters for the base case. Results from the sensitivity analysis are included in Appendix B, depicting the same output parameters and set up as the base case. Generally, the behavior of parameters was very similar in all cases, but deviations from the base case are pointed out and form the basis for further analysis.

Temperature profile is illustrated in Figure 5.1. Temperature is constant at the borehole wall where heat is applied and the surrounding formation is gradually being heated up with time. Temperature is largest near the borehole, and rapidly decrease with radial distance from the borehole. This is in line with the expected transient behavior described in Section 2.4.3.

Radial displacement is displayed in Figure 5.2. It is largest in magnitude at the borehole wall, where it is negative and in the direction of the well. With increasing distance from the borehole the magnitude of displacement decrease until it reaches zero, it then increases in magnitude in the direction away from the borehole. Rapid changes in displacement are observed close to the borehole, but where displacement is moving away from the borehole changes are slower and eventually, displacement converge to a positive value. With time displacement increase in magnitude everywhere, except around the point where displacement is zero. Hence, the model is expanding with a center at approximately 0.25 m from the borehole wall. The center of expansion varies for the cases in the sensitivity analysis. Radial displacement is positive at the boundary, which implies that the finite element model in this report is too small. At a given

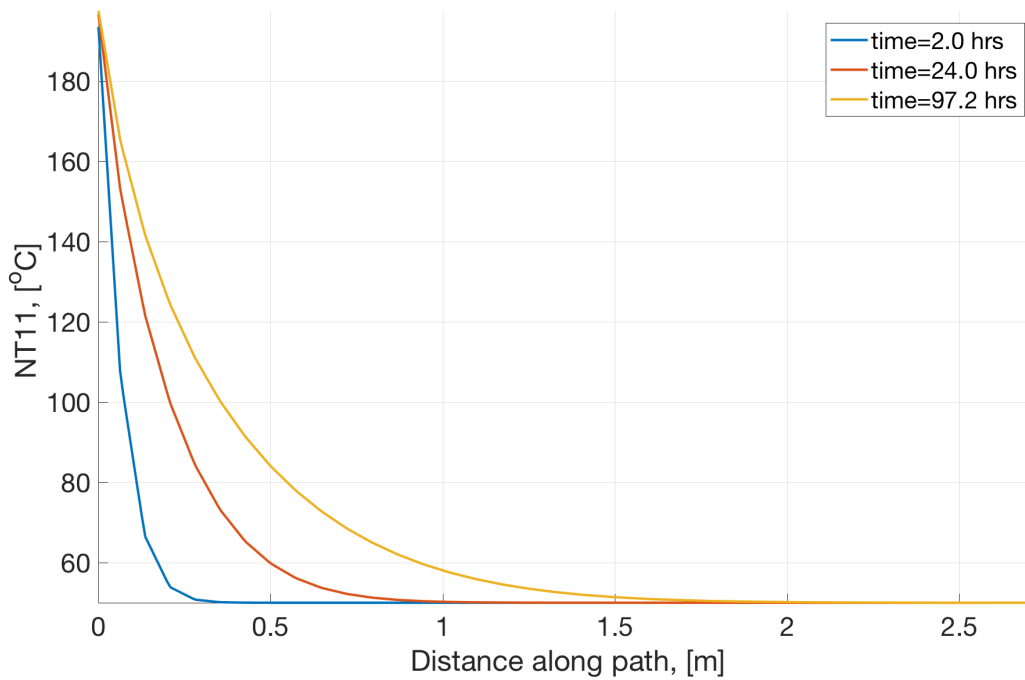


Figure 5.1: Case 1, Temperature profile in the formation resulting from the ABAQUS FEA. $r_w = 0.10$ m, $T_0 = 50$ °C

distance away from the borehole there will be formation unaffected by the influence of heating at the borehole, and the boundaries in the model should resemble conditions in that region. This may cause some artifacts in the results.

Pore pressure is depicted in Figure 5.3. Drainage effects are observed at the borehole boundary and close to the borehole, in line with a permeable boundary condition. Pore pressure increase with time and a peak develops near the borehole. The peak increases during the early time, but there is no significant increase after 24 h indicating that there is an upper bound for pore pressure. The upper bound extends into the formation with time, which may be explained by temperature progressing into the formation. Pore pressure rapidly decreases beyond the peak, reach values below the initial pore pressure and then converge at the initial pore pressure.

Case 3-7 exhibit very similar behavior as the base case, while considerable deviations were found in case 2. Pore pressure in case 2 is illustrated in Figure B.3, where a huge pore pressure peak, exceeding 90 MPa, is generated near the borehole at early times. This peak decay with time and progress into the formation. Case 2 is purely elastic, implying that the difference with the other cases is associated with the yield criterion. Consequently, the upper bound arise from the yield criterion, where further pressure increase is associated with inaccessible stress states. The material dilates during yielding, where pore space increase and counterbalance pore pressure increase, and may explain the emergence of the upper bound. Furthermore, pore pressure converges at the initial pore pressure beyond the peak in case 2. Hence, the values below the initial pore pressure in the other cases seem to be related to the yield criterion.

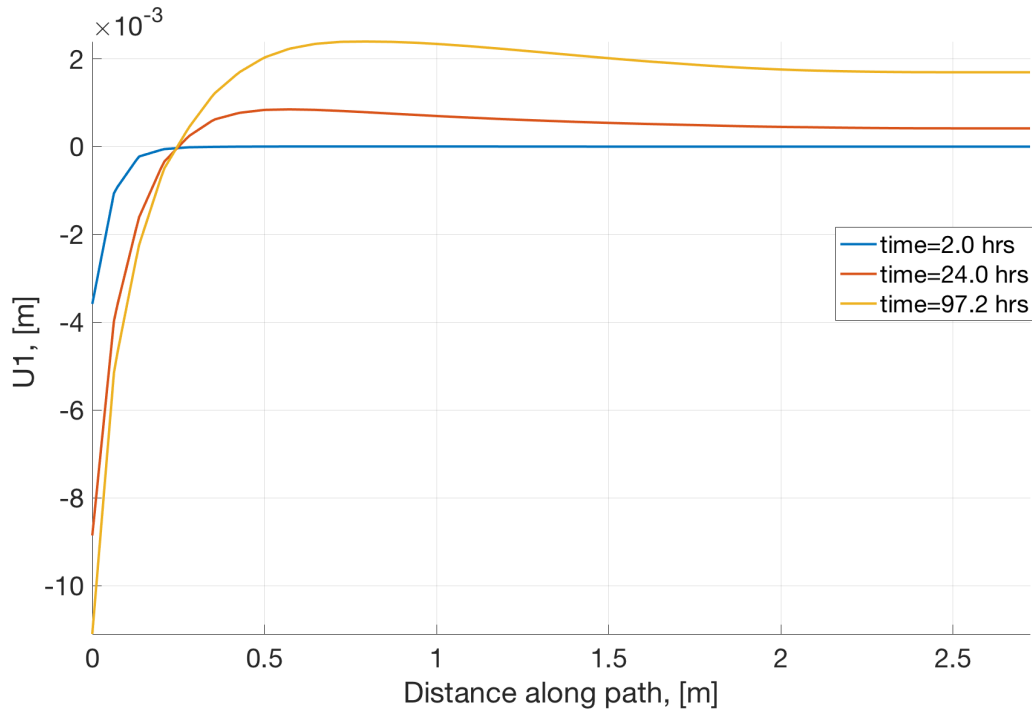


Figure 5.2: Case 1, Radial displacement in the formation resulting from the ABAQUS FEA. $r_w = 0.10$ m.

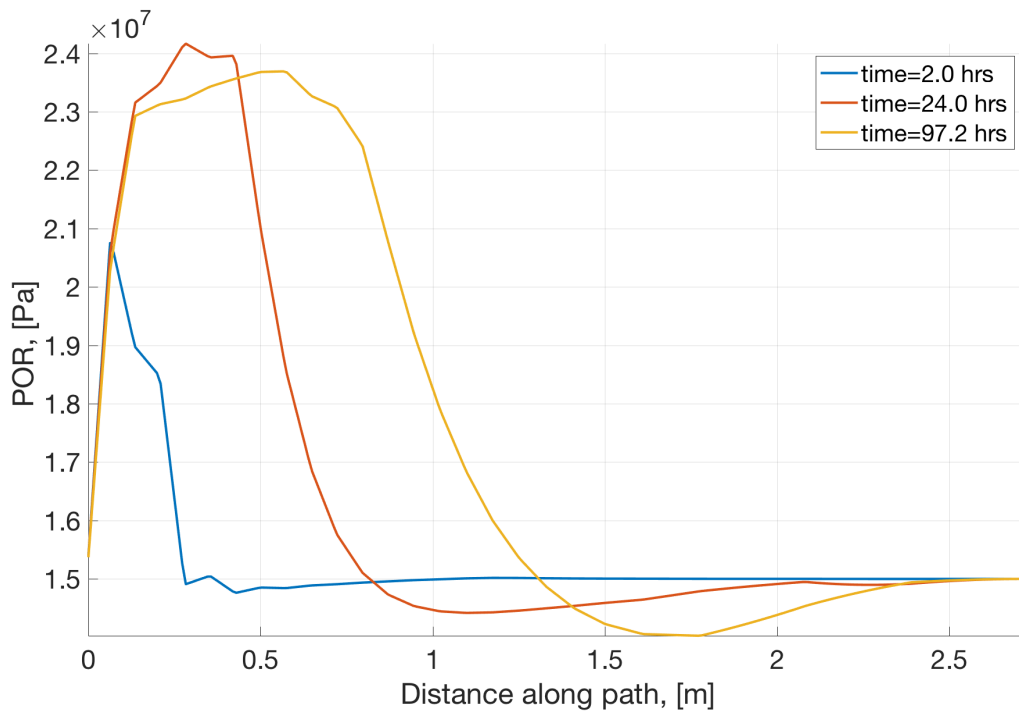


Figure 5.3: Case 1, Pore pressure distribution in the formation resulting from the ABAQUS FEA. $r_w = 0.10$ m, $p_{f0} = 15$ MPa.

The pore pressure distribution in case 4, seen in Figure B.14, depict values below the initial pore pressure that are even lower than in case 1. Whereas case 3 does not depict as low pressure

values as the base case, seen in Figure B.8. The yield criterion in case 4 is different from the base case, while case 3 has different stress conditions. These observations strengthen the hypothesis that the minimum pore pressure values are caused by the yield criterion. Moreover, it is possible that the pore pressure attaining values below the initial value is related to the radial displacement. From Figure 5.2 it is observed that the model expands, which is a possible reason for the pore pressure decrease.

Development of the void ratio is depicted in Figure 5.4. Change in the void ratio is large and positive close to the borehole, and decrease with distance from the borehole. Void ratio increase with time, in line with expectation as yielding causes dilation of the material.

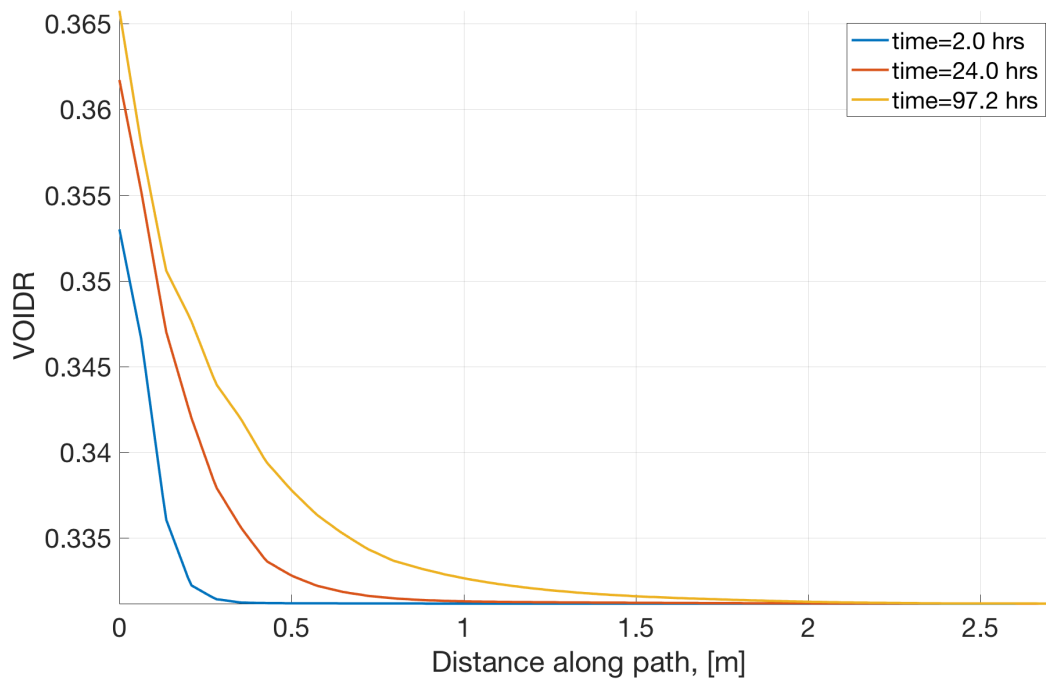


Figure 5.4: Case 1, Void ratio distribution in the formation resulting from the ABAQUS FEA. $r_w = 0.10$ m, $e_0 = 0.33$.

The total radial strain and radial plastic strain are depicted in Figure 5.5, and Figure 5.6, respectively. The graphs exhibit very similar behavior, and the small difference between the total strain and the plastic strain indicate that the elastic strain is very small compared to the plastic strain. The graphs have their maximum at the borehole wall, decrease swiftly with distance from the borehole and converge to zero. The total radial strain attains negative values, with an order of magnitude 1×10^{-4} , before it converges to zero, while plastic strain is always positive. This suggests that there is a small compression inside the formation. This phenomenon is also seen in the other cases, although larger magnitudes are seen for the elastic case 2 in Figure B.5. It is observed that case 2 has larger pore pressure peaks than the other cases, and the negative total strain always occurs at radial distances from the borehole that is higher

than the pressure peak. This suggests that the pore pressure peak compress parts of the deeper formation.

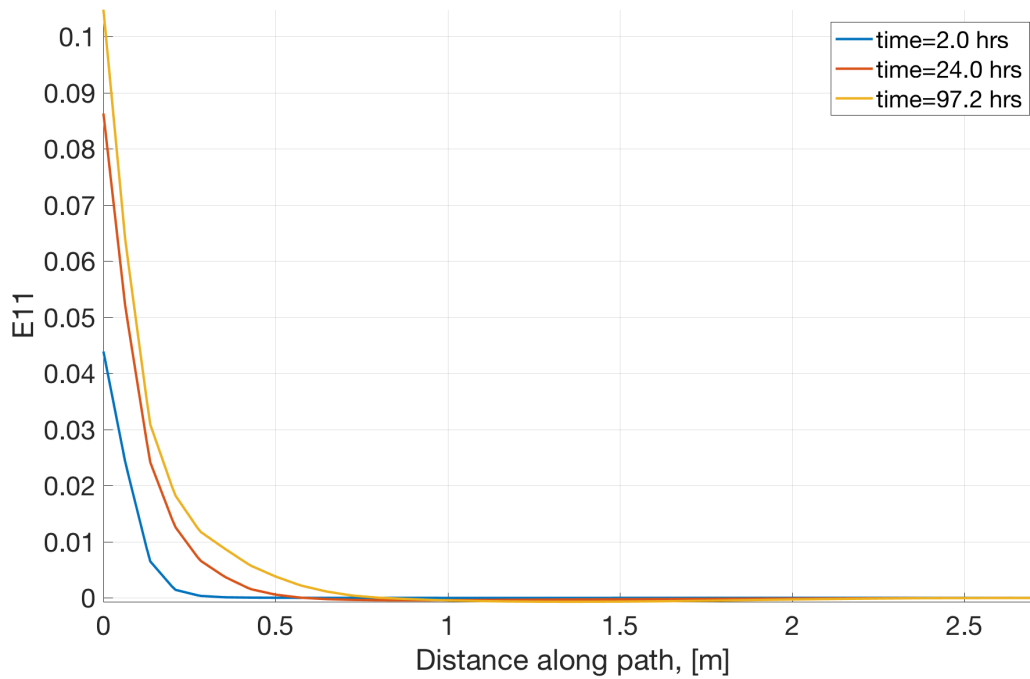


Figure 5.5: Case 1, total radial strain in the formation resulting from the ABAQUS FEA. $r_w = 0.10$ m.

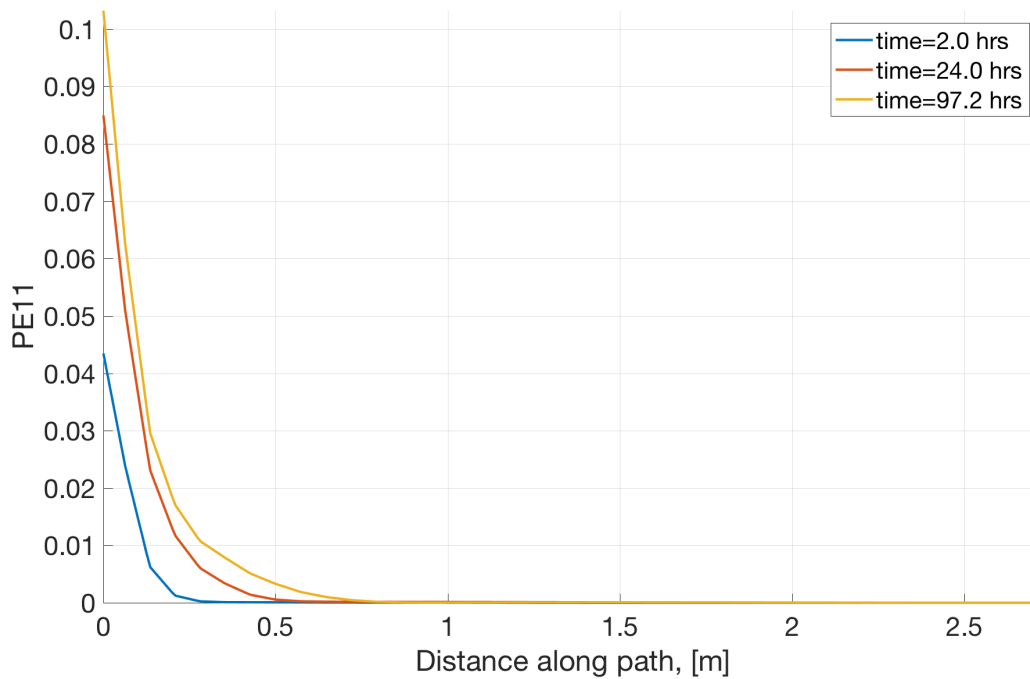


Figure 5.6: Case 1, Radial plastic strain in the formation resulting from the ABAQUS FEA. $r_w = 0.10$ m

5.2 Sealing potential

5.2.1 Displacement in the Base Case

Radial displacement of the borehole wall as a function of time is depicted in Figure 5.7, where the three nodes in Figure 4.1 are plotted. Negative radial displacement is in the direction into the borehole, and the radial displacement increase with time, however the largest changes are observed for early times. During the first 34 h borehole radius decrease with 1 cm, while the last remaining 64 h only yield 1.5 mm. The three nodes plotted show very similar displacement through the entire simulation indicating small anisotropy effects.

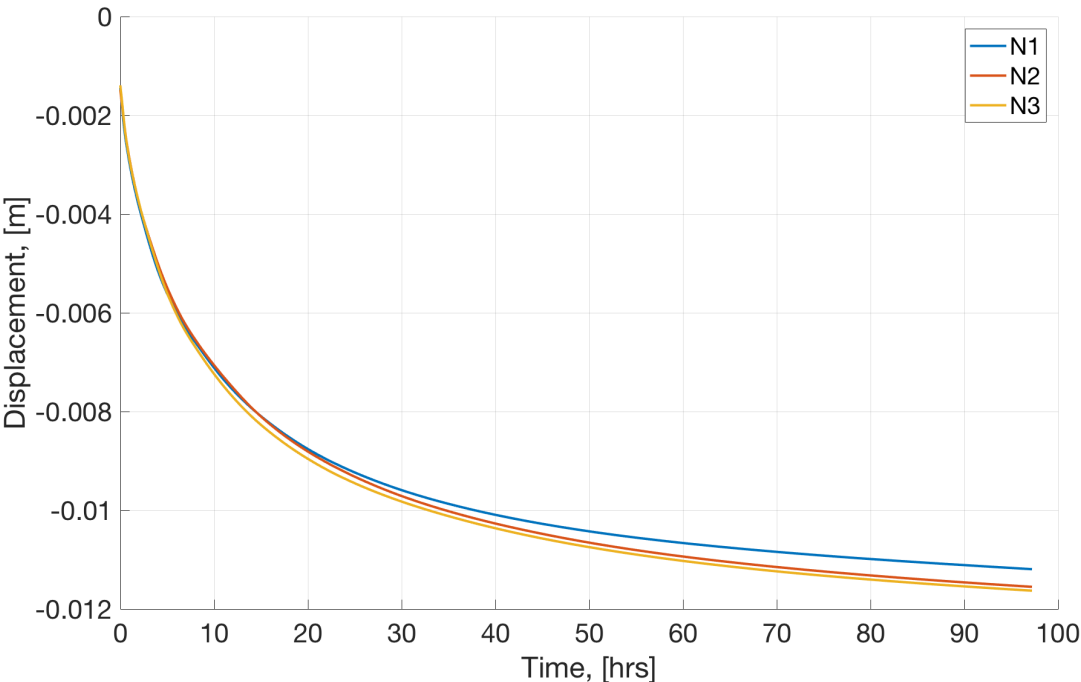


Figure 5.7: Case 1, Displacement at nodes N1, N2 and N3 vs. time

The total radial strain is essentially plastic, thus displacement primarily originates from plastic deformation. Plastic strain is significantly larger close to the borehole, indicating that extensive yielding occurs in this zone and generate the majority of the displacement into the borehole. Development in pore pressure is correlated with plastic strain, where the extension of the upper bound is associated with significant plastic strain. Thus, the decreasing trend of the plastic strain indicates that the upper bound extends slower with time, and explain why displacement rate decrease with time.

5.2.2 Displacement in the Sensitivity Analysis

Figure 5.8 compares displacement at the middle node, N2, over time for all the cases. A similar behavior as the base case is observed for the other cases, except case 2 which is close to zero throughout the four days of heating. Compared to the base case, case 3 and 7 yields a larger displacement, case 5 and 6 show almost the same displacement and case 4 is lower. Numerical values of displacement are given in Table 5.1 for displacement at 97.2 h at the three nodes N1, N2 and N3. Compared with predictions in Table 4.3 all predictions except case 5 and 6 were correct.

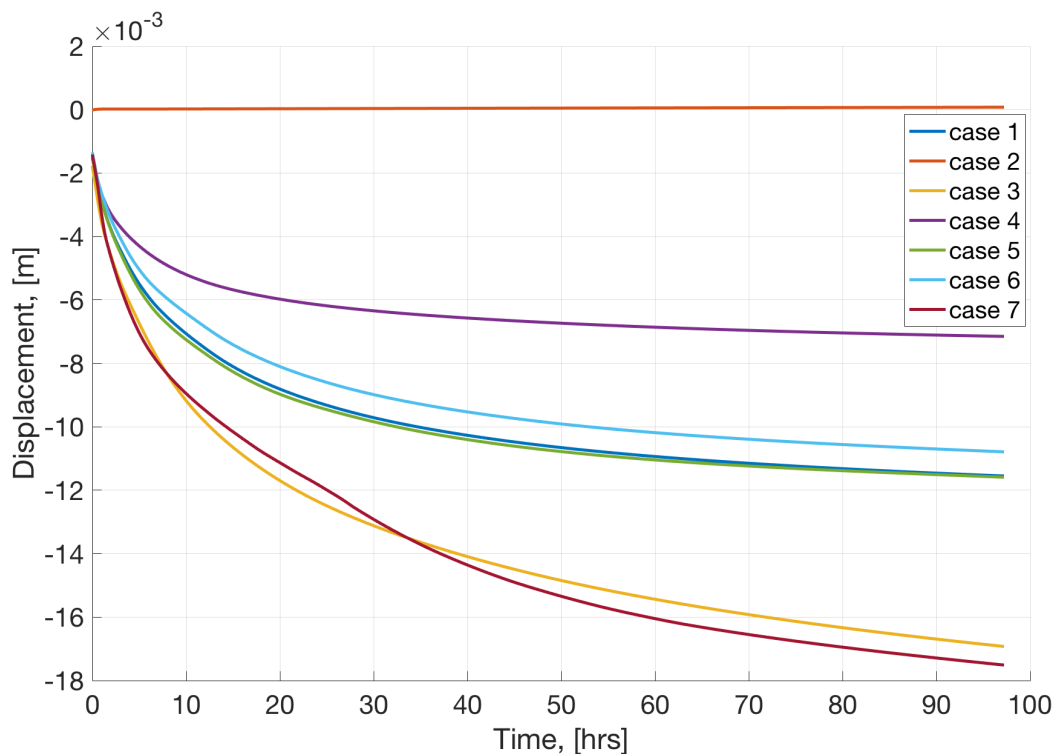


Figure 5.8: Displacement at N2 vs. time for all cases

Table 5.1: Displacement at 97.2 h for N1, N2 and N3. Positive values are directed into the borehole.

Case	Node 1	Node 2	Node 3
	U_r [mm]	U_r [mm]	U_r [mm]
1	11.19	11.55	11.63
2	-0.0797	-0.0754	-0.0795
3	16.6	16.93	16.97
4	7.35	7.15	6.78
5	11.54	11.59	11.39
6	10.42	10.79	10.87
7	16.43	17.51	18.11

The purely elastic case 2 generated very low displacement, which was in line with expectations. Moreover, the negative values illustrate that the borehole enlarges due to the temperature increase around the borehole. Radial displacement in case 2 is shown in Figure B.2, where displacement increase with distance away from the borehole and indicate that the material, is expanding. With an expanding material it is also expected that the borehole would become larger, which is observed in Table 5.1.

As expected, case 3 with lower initial pore pressure and well pressure, exhibit larger displacement than the base case, in agreement with the hypothesis. Close to the borehole plastic strain in case 3, shown in Figure B.11, was larger than in case 1, suggesting that the stronger stress concentration in case 3 generate more plastic deformation and has a greater potential for establishing a shale barrier than the chosen base case.

In line with predictions, the higher dilatancy angle in case 4, results in lower displacement than case 1. The void ratio for case 4, displayed in Figure B.15, was greater than the change in void ratio in case 1. The larger pore volume counteracts pore pressure increase, which in turn result in less plastic strain, seen in Figure B.17. This suggests that increasing dilatancy angle reduce the potential for thermal stimulation of shale barriers.

The lower permeability in case 5 results in very similar displacement as the base case. There was expected some difference in pore pressure behavior due to the lower permeability, and these are observed from the pore pressure distribution in case 5, seen in Figure B.20. Several spikes are observed in the zone close to the borehole, and the average value of these spikes are larger than the average pore pressure peak in case 1, whereas, in the far away field (1.0 m to 1.5 m) there is also a difference where case 1 is larger. This was in line with the hypothesis; pressure accumulation close to the borehole and less hydraulic diffusion to the far away field. The larger pore pressure close to the borehole corresponds with the slightly higher plastic strain in this zone, and the lower pore pressure in the far away field with the slightly lower plastic strain in case 5. This suggests that the additional pore pressure close to the borehole compensate for that in the far away field with respect to plastic deformation.

The effect of increasing permeability has not been included as a case in the sensitivity analysis. However, from a theoretical point of view, this would not allow pore pressure accumulation, which in turn would not reduce effective stresses and generate plastic deformation.

The reduced linear thermal expansion coefficient of the matrix in case 6 lead to a slightly lower displacement than case 1, which was not expected. Comparison between case 1 and 6 show a difference in pore pressure; the high-pressure zone near the borehole in case 1 attain higher values than case 6, while in the far away field case 6 depict larger pore pressure. Plastic strains show the same trend. The difference in pore pressure was largest nearby the well, where the upper bound for pore pressure was generally 0.4 MPa lower than in case 1, while in the far away field case 6 was approximately 0.2 MPa higher, which may contribute to causing

the slightly lower displacement in case 6. The reduced thermal expansion coefficient of the matrix was expected to result in lower earth stress. Assuming this takes place, the lower pore pressure observed suggest that it is affected by lower stress. A possible explanation is that thermally induced stress generate more pore pressure since the additional stress acting on the matrix develop a compressing force on pores leading to rising pore pressure in the nearly incompressible pore fluid. The pore pressure change related to changing earth stresses. This is similar to the effect of the Skempton B-coefficient, which characterize the change in pore pressure response for a given change in mean stress, shown in equation (2.33). However, this only applies for undrained conditions (Fjær et al., 2008, p. 35). Further investigation with respect to the ABAQUS FEA and the thermal expansion coefficient of the matrix is required to understand the difference in displacement between case 1 and 6.

The temperature dependency in case 7 resulted in more displacement than the base case, in agreement with the hypothesis. There is a difference between temperature profiles between case 1 and 7, seen from Figure 5.9, which illustrate temperature in case 1 subtracting case 7 at 2 h, 24 h and 97.2 h. Generally, the temperature is higher in case 7 than in case 1, and temperature increase propagates slightly deeper in case 7. The bottom point on the three graphs represent the maximum difference, and it decays and propagates into the formation with time. This indicates that temperature increase in case 7 was fast in the beginning and slowed down with time, which perfectly corresponds with specific heat capacity increasing with time. With slower temperature increase less thermal influence was expected, however, plastic strains were larger at all distances relative to the base case, as illustrated in Figure B.35. This observation suggests that the increased linear thermal expansion coefficient of the pore fluid compensate for slower temperature rise.

5.2.3 Influence of Stress Anisotropy

Effects of stress anisotropy are observed from Table 5.1, where displacement is different between the three nodes, and generally larger in the direction where $\theta = 90^\circ$, in agreement with the hypothesis. Figure 5.10 is an excerpt from the ABAQUS GUI and depicts the radial displacement of case 1 at 97.2 h. The excerpt shows a cutout of the lower 0.5 m of the model to mitigate possible boundary effects. Radial displacement is largest on the borehole wall, directed into the borehole. In the far away field displacement is directed away from the borehole in the x -direction, and decrease towards the y -direction where radial displacement is directed into the borehole at all distances, however with smaller magnitude than in the x -direction. Excerpts for case 2-7 are included in Appendix B.4.1. Generally, the other cases exhibit the same behavior as case 1, although with varying intensity in x - and y -directions. However, radial displacement in case 4 with higher dilatancy angle, seen in Figure B.48, depict displacement moving away from the borehole also in the y -direction. Furthermore, radial displacement in case 2 with elastic

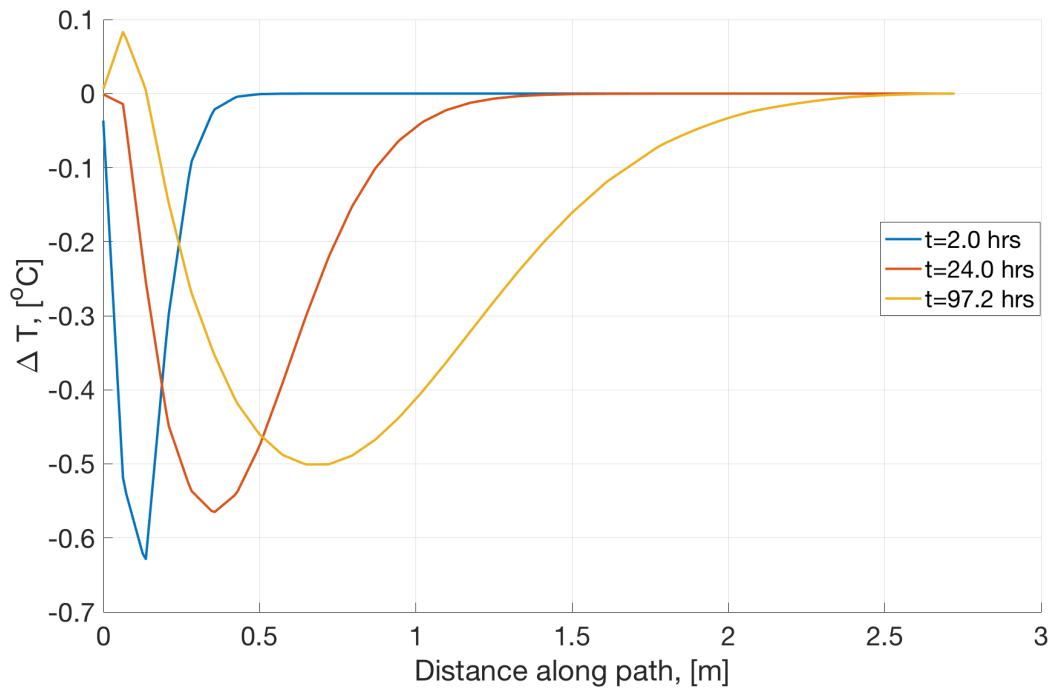


Figure 5.9: Temperature profile in case 7 subtracted from case 1 at 2 h, 24 h and 97.2 h

conditions, displayed in Figure B.46, depict a very small difference between x - and y -directions. The yield criterion is changed in case 4 and is not included in case 2, which indicate that the yield criterion influence variations in displacement around the borehole.

The larger displacement in the x -direction than y -direction, seen from the red and green areas in Figure 5.10, may be a result of shear deformation. The pore pressure increase cause deformation of the material, where the counter force in the x -direction is smaller than in the y -direction, resulting in the larger deformation in x -direction towards the minimum horizontal stress. In comparison, a ductile cube subject to a vertical force would generate shear deformation in x - and y -directions, however, if the cube is restricted in the y -direction, all shear deformation would develop in the x -direction. Furthermore, the spatial depiction of radial displacement show that all boundaries are influenced at 97.2 h, which repeats the implication that the size of the numerical model is too small. A larger model where this effect is considered could potentially generate even more displacement into the borehole, and should be further studied.

The larger dilatancy angle in case 4 generated an area in the far away field where radial displacement in the y -direction was in the direction away from the borehole. The larger dilatancy angle implies more volumetric plastic strain per plastic shear strain, such that more deformation should occur in both x - and y -direction, and may explain the radial displacement away from the borehole towards the maximum horizontal stress in case 4. Furthermore, displacement of the borehole wall was largest at node 1, in contrast to the other cases. Why this occurs in case 4 is currently not understood, and further investigation is required to understand this result.

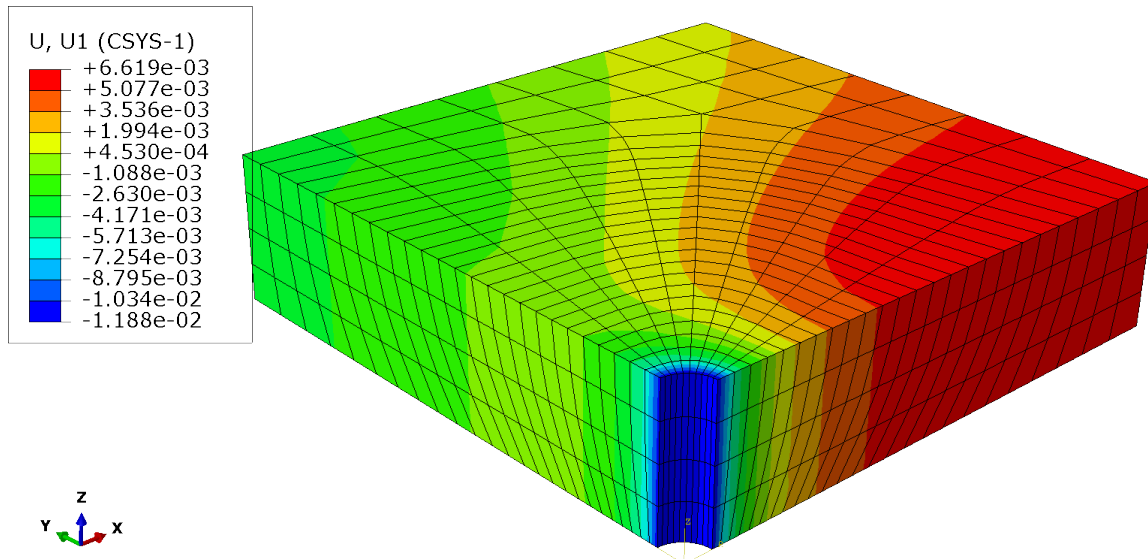


Figure 5.10: Excerpt of ABAQUS FEA model for Case 1 displaying radial displacement at 97.2 h for a cutout of the lower 0.5 m of the model

The smallest relative difference between displacement at N1 and N3 in Table 5.1 were in case 3 and 5 with 2.2% and 1.3%, respectively, and the largest were in case 4 and 7 which generated 8.4% and 9.3%, respectively. This suggests that case 3 and 5 were less sensitive to stress anisotropy than the other cases. Comparing radial plastic strain between case 3, 5 and 7, observed in Figure B.11, Figure B.23 and Figure B.35, respectively, revealed that case 7 extend deeper into the formation than any other case, while case 3 and 5 were limited by plastic strains primarily developing near the borehole. It is possible that the extension of radial plastic strain into the formation has an effect on displacement around the borehole.

An excerpt of radial plastic strain in case 1 at 97.2 h is displayed in Figure 5.11 to illustrate the spatial extent of radial plastic strain for the lower 0.5 m of the model. The radial plastic strain is largest at the borehole wall and develops deeper in the direction of minimum horizontal stress. Additionally, plastic strain is larger in the direction of minimum horizontal stress, both on the borehole wall and deeper into the formation. Excerpts for case 3-7 are included in Appendix B.4.2. Overall the other cases demonstrate the same behavior as the base case with some variation in magnitude. The spatial extent of radial plastic strain is larger in the direction of minimum horizontal stress, which generally, correlate with displacement on the borehole wall. However, with higher dilatancy angle in case 4, displacement at the borehole wall is largest in the direction of maximum horizontal stress, while plastic strain is larger in the direction of minimum horizontal stress. This suggests that additional effects are influencing the displacement around the borehole, and further evaluation is required to discover them.

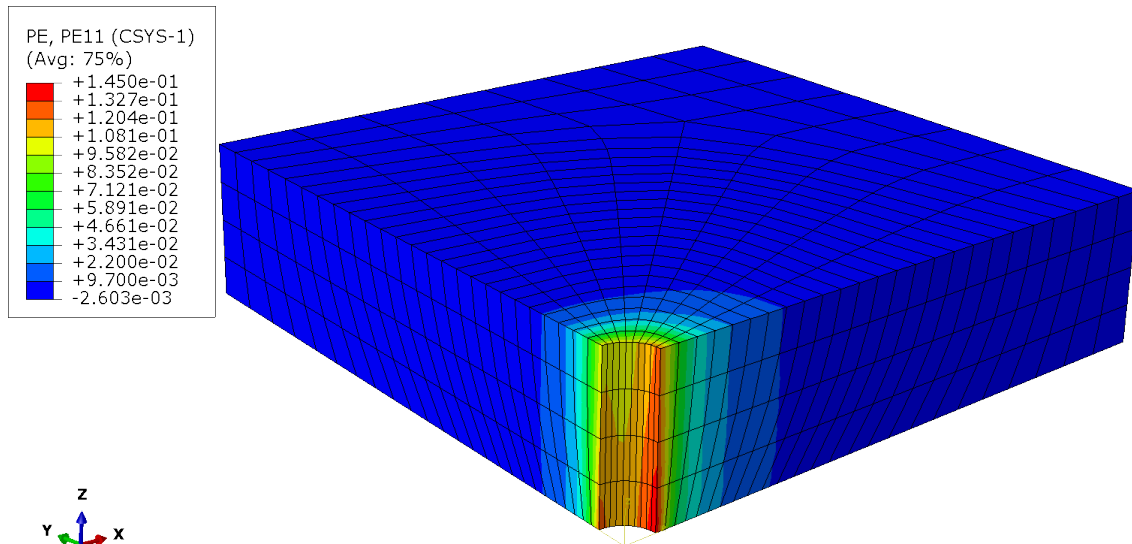


Figure 5.11: Excerpt of ABAQUS FEA model for Case 1 displaying radial plastic strain at 97.2 h for a cutout of the lower 0.5 m of the model

5.2.4 Combining Annular Pressure Reduction and Heating to Stimulate Shale Barriers

Case 3 represents a variation of the base case with reduced pore pressure and well pressure. With time, a large pore pressure increase occurs close to the well and reach an upper bound. The upper bound is approximately the same as in case 1 due to the identical yield criterion. Thus, case 3 exhibit similar stress conditions as case 1 close to the wellbore, but with reduced well pressure, analogous to a case where only well pressure is reduced. Case 3 resulted in higher displacement at the borehole wall, which suggests that heating combined with reducing well pressure is an even more effective stimulation technique for shale barriers than heating alone.

Stress conditions for case 1 and 3 are illustrated in Figure 5.12 and Figure 5.13, respectively. Pore pressure and radial, tangential and axial stress resulting from the simulation at 24 h are plotted together to display stress conditions along the diagonal path. To display progress with time, the same set up at 2 h and 97.2 h is included in Appendix B.2 for both cases. The blue vertical line denoted *Yield Limit* signify where plastic strain becomes zero, such that everywhere left of the blue line has reached the yield criterion. The red stippled vertical line marks the distance from the borehole wall that is three times the borehole diameter.

The general behavior in stress conditions in case 1 and 3 was very similar. High pore pressure and extensive yielding were taking place close to the borehole, leading to very low effective stresses in that region. With increasing distance from the well effective stress approach the far field stress, in line with the theory for plastic behavior with the Mohr-Coulomb yield criterion in

Section 2.3.2. Compared to stress conditions surrounding a borehole with intact rock, exemplified in Figure A.1, the stress conditions are evidently different to the left of the yield limit, and especially close to the borehole. With increasing time, the zone of extensive yielding moves into the formation, and at 97.2 h it is observed to surpass the red stippled line for both case 1 and 3. When only pressure reduction in the well is affecting stress conditions, plastic deformation is limited to the zone of stress redistribution in the well, which usually extend from the borehole wall to a distance of 2 to 3 borehole diameters into the formation. Hence, the red stippled line denotes the maximum extent of the stress redistribution due to drillout. This indicates that heating the borehole cause plastic deformation to develop deeper and has the potential to generate more displacement at the borehole wall.

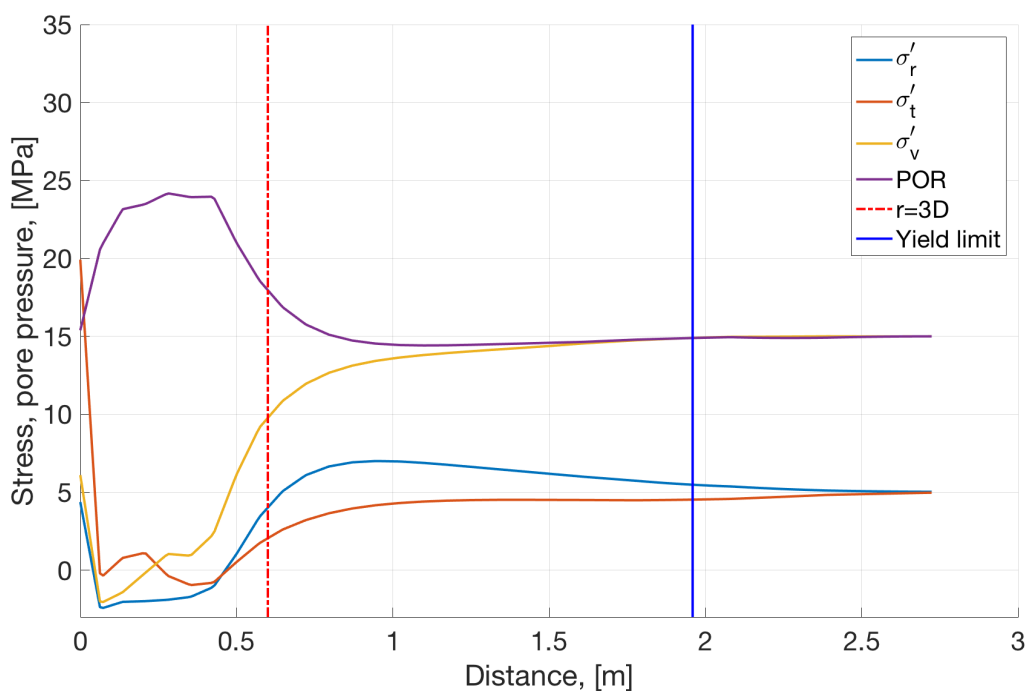


Figure 5.12: Effective stresses in r -, θ - and z -direction and pore pressure on the diagonal path at 24 h in case 1. The red stippled vertical line marks distance from the borehole wall equal 3 times borehole diameter, and the blue vertical line signify where plastic strain is zero

The yield limit in case 3 was closer to the borehole than in case 1, suggesting that case 3 is less susceptible to failure in the far away field. Far field stress conditions in case 1 was very close to the failure envelope, seen in Figure 4.5, whereas the lower pore pressure in case 3 shift the Mohr circle to the right, which explain why there is such a large difference in the blue yield limit line between the two cases. Plastic strain in case 1, depicted in Figure 5.6, shows that there is very little yielding in the far away field, even though the yield limit is deep into the formation. This implies that plastic strains in both case 1 and 3 are primarily generated near the borehole.

The difference between pore pressure in case 1 and 3 is seen in Figure 5.14, at 2 h, 24 h and 97.2 h, where case 3 is subtracted from case 1. During the early time, the difference is

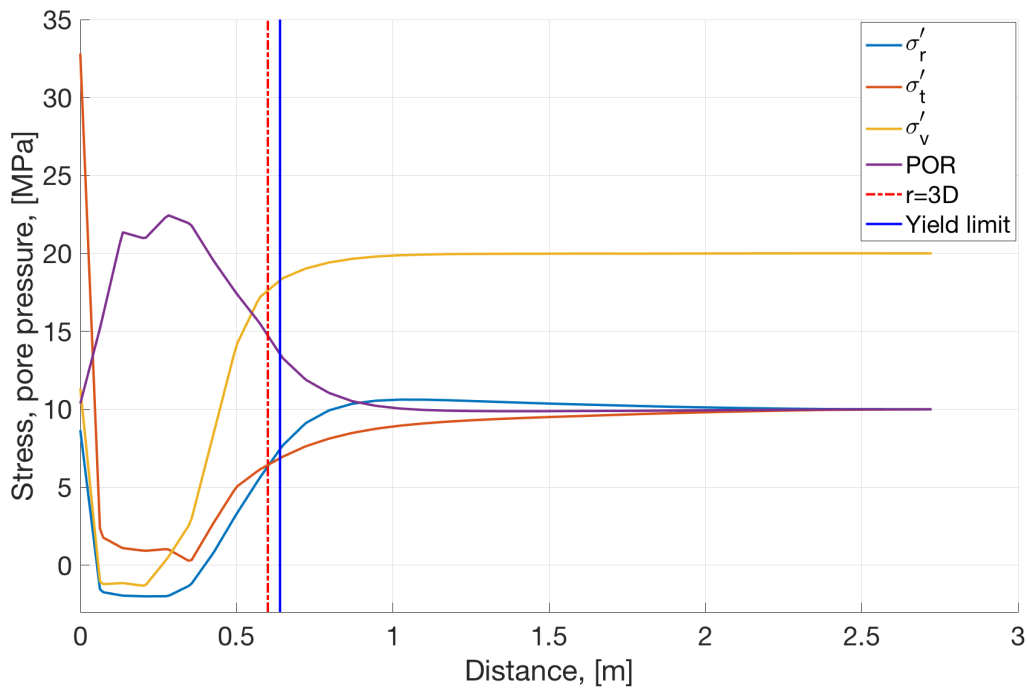


Figure 5.13: Effective stresses in r -, θ - and z -direction and pore pressure on the diagonal path at 24 h in case 3. The red stippled vertical line marks distance from the borehole wall equal 3 times borehole diameter, and the blue vertical line signify where plastic strain is zero

approximately the same as the pressure reduction in case 3: 5 MPa. With time case 1 reaches its upper boundary close to the borehole, while case 3 experience further pressure increase to reach the upper boundary. At late time there is approximately no difference in pore pressure between the two cases, which coincide with the theory since both cases have the same yield criterion. With distance from the well the difference approach the initial pressure difference between the cases. This was expected, as pore pressure is less affected by temperature and the yield criterion at increasing distance from the well. The rate of plastic deformation was expected to be largest when pore pressure had reached its upper bound. Case 3 took longer to reach its upper bound compared to case 1, which suggest that the stronger stress concentration has a larger influence on increasing displacement at the borehole wall.

Reducing pore pressure shift the Mohr circle to the right, further away from the failure envelope, while increasing pore pressure shifts it to the left, closer to failure. While, decreasing well pressure lead to stronger stress concentration and increasing it has the opposite effect, seen from equations (A.1)-(A.3). This suggest that a case where well pressure is reduced while initial pore pressure is unchanged would lead to even more displacement because the pore pressure peak near the borehole would be reached faster.

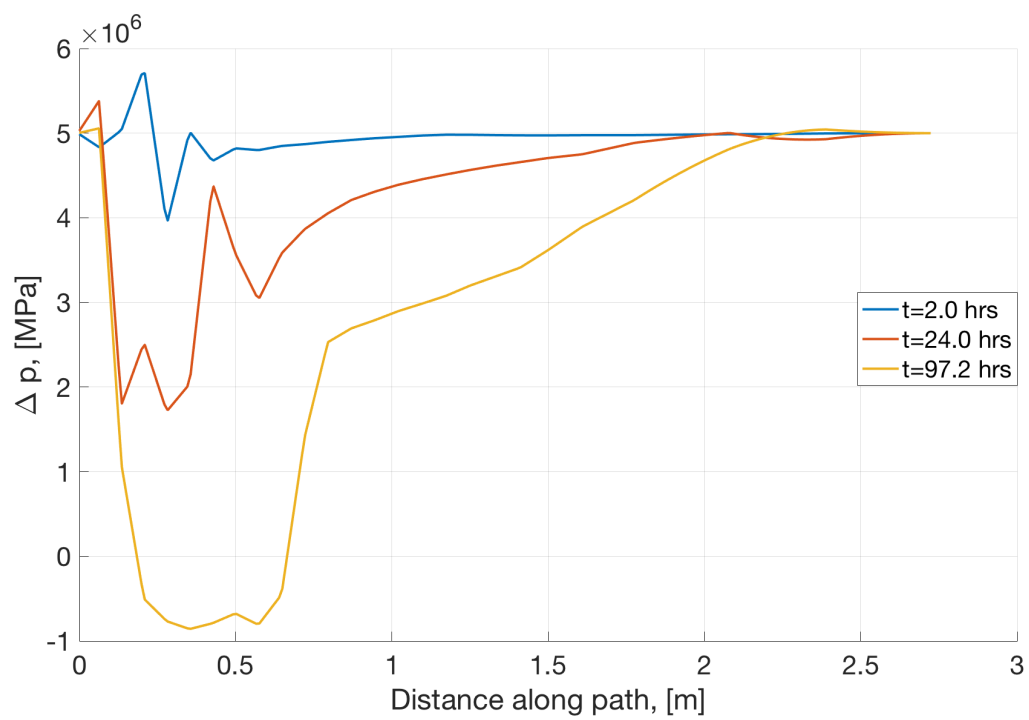


Figure 5.14: Pore pressure difference between Case 1 and 3 at 2 h, 24 h and 97.2 h

5.3 The Pressure-Temperature Relation

The relation between pore pressure and temperature, referred to as the coupling coefficient, is illustrated in Figure 5.15 for case 1. It was calculated based on equation (4.3) with data as described in Section 4.1, and a minimum temperature increase of $0.05\text{ }^{\circ}\text{C}$ was specified as a minimum to calculate the coefficient. For $r \leq 0.55\text{ m}$ the coupling coefficient decrease with time until it is approximately zero, while $r \geq 0.55\text{ m}$ increase at first, then is constant and eventually decrease until it is approximately zero. The decrease with time is repeated at all radii, implying that some of the trends seen for deeper radii may be hidden in radii close to the well.

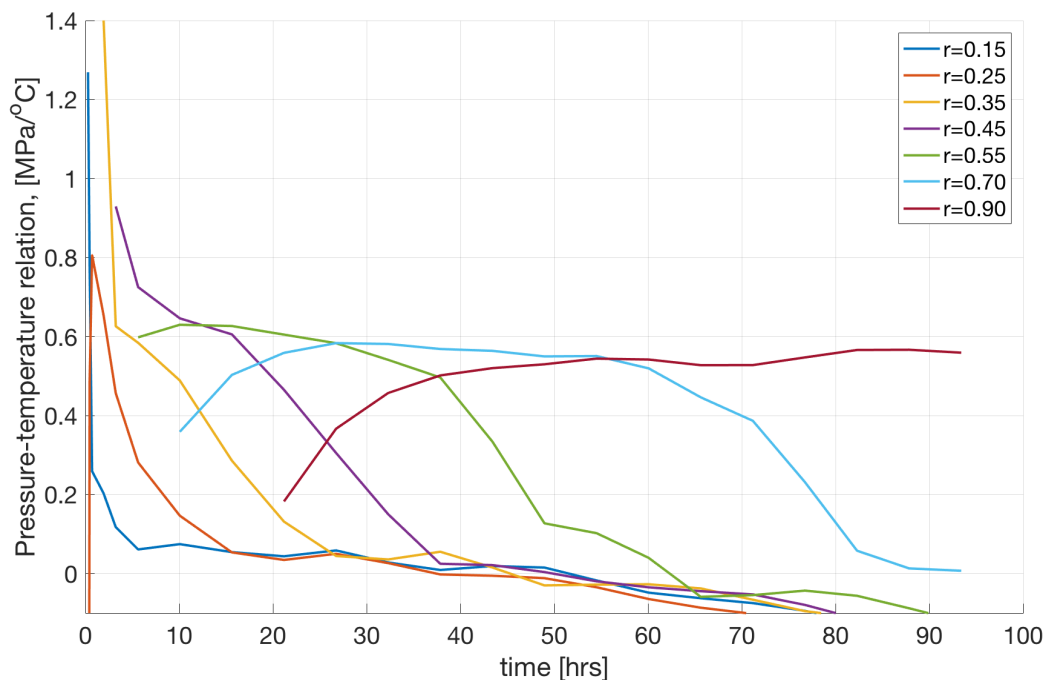


Figure 5.15: Pressure-temperature relation, for case 1 at different radii from the borehole wall as function of time

The coupling coefficient would be constant at all radii if pore pressure change exclusively is affected by thermal expansion, but it varies with time, such that other effects must have been present. Three main effects are assumed to influence the coupling coefficient; thermally induced pore pressure, pore pressure diffusion and the yield criterion. Pore pressure diffusion develop due to differences in pressure and may decrease pore pressure where thermal expansion has caused a large pressure increase, and increase pressure where thermal effects are less dominant and adjacent to high pore pressure zones. It is plausible that pressure diffusion generate the peak at early time close to the the well. The peak is larger than any coupling coefficient at later time indicating that pore pressure increase originates from more than only thermal expansion. Yielding is expected to reduce the coupling coefficient since pore volume increase counteracts further pressure increase. The decreasing coupling coefficient is believed to be caused by

yielding, and where the coupling coefficient is approximately zero extensive yielding is assumed to take place as pore pressure is at its upper bound while temperature is still increasing.

For $r \geq 0.55$ m the coupling coefficient exhibit almost constant values before it eventually decrease. The stress condition for case 1, illustrated in Figure 5.12, show that yielding has already occurred at these radii. However, plastic strains are very small and so are pressure differences in this region, indicating that there is limited yielding and hydraulic diffusion. Thus, these constant values of the coupling coefficient might resemble an estimate of the pressure-temperature relation only affected by thermal expansion.

The finite element analysis features very low permeability, which should promote low hydraulic diffusion. Pressure increase at the temperature front is expected to be dominated by thermal expansion leading to a constant coupling coefficient at early time. However, it is increasing before it reach a nearly constant value. Figure 5.3 illustrates noticeable change in pore pressure across the entire model after one day, while the temperature front has only reached 0.9 m from the borehole wall. This may be a numerical artifact caused by the model being too small. However, as the coupling coefficient increase before it attains the constant value, it is possible that the yield criterion is influencing the coefficient. The sensitivity analysis was used to investigate this claim. The coupling coefficients for all the cases are included in Appendix B.3, illustrated graphically with the same method as the base case in Figure 5.15. Generally, all cases exhibit the same tendency as described for case 1, but case 2 and 3 deviate slightly.

Case 2 is purely elastic such that its deviations from the base case highlights effects of the yield criterion, and is observed in Figure B.40. The decreasing coupling coefficient, which is proposed to be caused by yielding in case 1, is also present in case 2, but only for radii very close to the borehole, seen from $r = 0.15$ m and 0.25 m. The decrease might be affected by the large increase in radial strain close to the borehole. Furthermore, at $r = 0.15$ m the decreasing coupling coefficient continues to decrease below zero, this was also the case for all radii $r \leq 0.15$ m, indicating that the pore pressure derivative must be negative. The pore pressure in case 2 has a maximum close to the wellbore at early time, and with time it decays and progress into the formation, seen from Figure B.3, which mean that all radii to the left of the pressure peak will get decreasing and eventually negative pressure derivatives and coupling coefficients. Thus, it is likely that the decreasing trend in case 2 is primarily caused by the moving pore pressure peak. Radii deeper into the formation, $r \geq 0.35$ m, show an increasing coupling coefficient, and then a constant value, and no decreasing trend. These radii are to the left of the pore pressure peak at all times, which suggest that the decreasing trend at these radii in case 1 is caused by yielding. Moreover, the constant coupling coefficient at these radii are larger than in case 1. The only difference between case 1 and 2 is the yield criterion, such that the same thermal expansion is expected, thus the difference in the constant coupling coefficients might be caused by yielding.

As discussed in Section 5.2.4 case 1 is yielding deep into the formation, whereas case 3 is

primarily yielding near the well. The coupling coefficient for case 3, seen in Figure B.41, exhibit a similar trend as that of case 1, however, two plateaus are observed for the constant value. The upper plateau exist where plastic strain is zero and has the same value as case 2, and the lower plateau exist where plastic strain is non-zero and is equivalent to the constant value in case 1. This indicate that the constant value in case 1 is affected by yielding, and that the constant coupling coefficient in case 2 and higher plateau in case 3 are better estimates of the pressure-temperature relation only affected by thermal expansion. The relation is approximately $0.85 \text{ MPa } ^\circ\text{C}^{-1}$, and compared to the analytically derived coupling coefficients for earth stresses, $0.15 \text{ MPa } ^\circ\text{C}^{-1}$ and $0.075 \text{ MPa } ^\circ\text{C}^{-1}$, temperature influence on pore pressure is dominant. In turn, the Mohr circle has a greater tendency to shift to left towards the failure envelope, indicating that heating is an effective mechanism to cause plastic deformation in the finite element model evaluated in this report.

5.4 Temperature Reduction After Stimulation

The finite element analysis has shown that heating the borehole wall generate displacement into the borehole. Assuming heating the borehole induce sufficient displacement to establish a sealing barrier with the casing, it is important that the formation does not recede after the stimulation when temperature return to its in-situ state as that would impair the feasibility of the stimulation technique. This was investigated by adjusting the base case to include a temperature decrease succeeding the four days of heating. Analogous to the method used to model heating, two steps were used to model cooling. One step changed the temperature on the borehole wall from 200 °C to 50 °C during five seconds, and the next step held the temperature constant at 50 °C as a boundary condition on the borehole wall for another 350 000 s. The resulting radial displacement when all steps were included is illustrated in Figure 5.16. The behavior for the first 97.2 h is the same as previously described, but an abrupt change is observed the moment temperature decrease, and with time displacement converge to a constant value. This indicate that reducing temperature back to in-situ conditions increase displacement and the displacement is permanent, which implies that thermal stimulation of shale barriers is a feasible stimulation technique. The abrupt increase in displacement may be explained by elastic deformation where cooling the formation result in a contraction of the material, consequently the borehole shrink in size. This is the opposite effect of that seen for displacement of the elastic case 2.

It is emphasized that radial displacement related to cooling the formation is the only output parameter that has been evaluated because it provide a direct answer to whether thermal stimulation of shale barriers is feasible. However, when the energy source in the well stop providing heat to the surrounding formation there are still large amounts of energy stored in the formation. This may cause continued temperature convection and change conditions after the stimulation has ended. It has already been established that the numerical model in this thesis is too small and may lead to numerical artifacts in the results, and especially for the late times of the model, such as during the temperature reduction. Consequently, further investigation of formation cooling should be evaluated to study these effects.

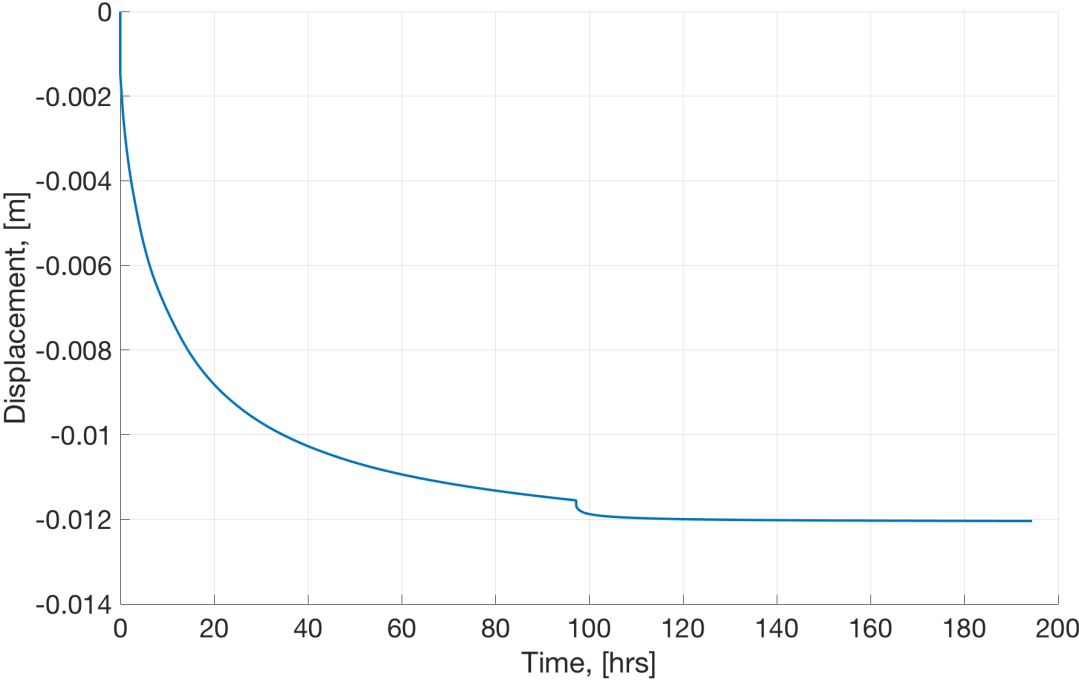


Figure 5.16: Radial displacement in the base case including heating and temperature reduction.

5.5 Implications from the Finite Element Analysis

5.5.1 Stimulating Shale Barriers

The finite element analysis show that heating the wellbore promote large pore pressure increase and extensive yielding close to the wellbore such that shale formation displaces into the borehole. Case 7 includes temperature dependency for many of the input parameters and, for this reason, is believed to pose the most realistic situation, compared to the other cases. The magnitude of radial displacement into the borehole in case 7 was 16.4 mm to 18.1 mm, and with the borehole radius 100 mm this represents an average shear deformation, $\Delta r/r_w$, of 17.25%. The magnitude of the shear deformation is put into context in Figure 5.17 with a schematic of a horizontal cross section of a well where displacement resulting from case 7 is included. The red stippled circle show the size of the original borehole, the grey circle is the casing and the colored area in between represents the amount of shale that has displaced into the borehole. The size of the borehole and casing is based on the ratio between a 12^{1/2}" hole diameter and a 9^{5/8}" casing diameter, and displacement from the simulation is scaled to fit this aspect ratio. The final borehole size is based on displacement at nodes N1 and N3. The white gap outside the casing is the remaining annulus succeeding 4 days of heating for the specified borehole-casing dimensions. The remaining gap is not very large, and illustrate the effectiveness of heating the borehole to displace formation into the borehole. Table 5.2 displays typical dimensions for borehole and outer casing diameters going through the overburden on the NCS, and the corresponding shear deformation required to form a barrier around the casing. The average shear deformation resulting from case 7 is included in the bottom of the table for comparison, and depict that shear deformation from the simulation is not sufficient to form a barrier in any of the borehole-casing configurations in Table 5.2, although it is very close in the 8.5 inch borehole. Consequently, the finite element analysis in this thesis does not provide a setup that predicts development of a sealing barrier in the shale formation subject to heating.

Table 5.2: Required shear deformation to seal typical borehole diameter and casing sizes. †: Average value

Open Hole Diameter [in]	Casing Diameter [in]	Required Shear Deformation [%]
17.5	13 ^{3/8}	23.6
12.5	9 ^{5/8}	23.0
8.5	7.0	17.6
Case 7		
7 ^{7/8}	NA	17.25 †

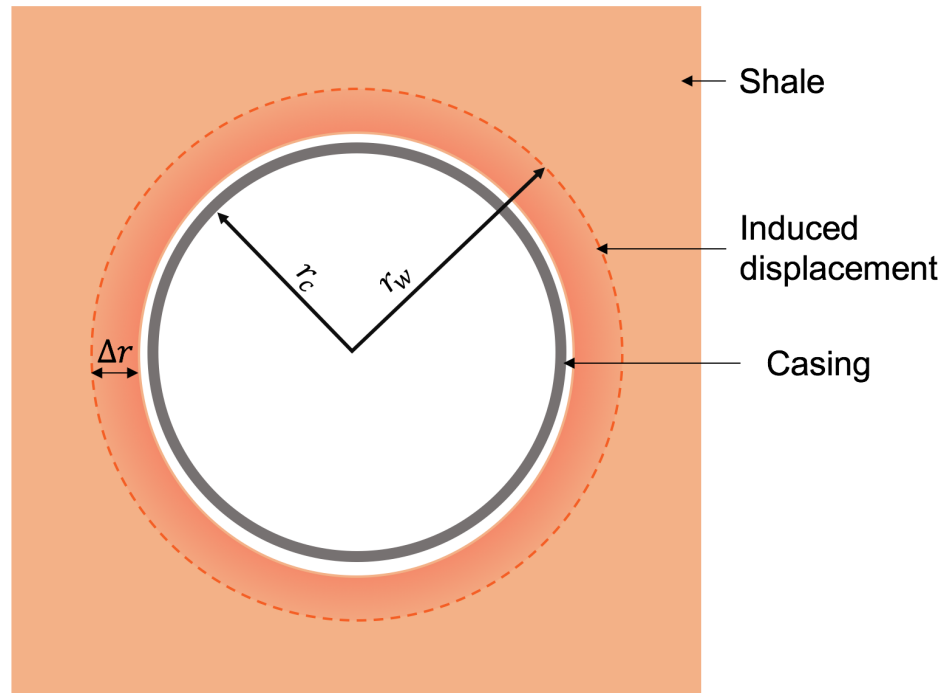


Figure 5.17: Schematic of a horizontal cross section of a well displaying heating induced shale displacement in case 7

5.5.2 Candidate Selection

The sensitivity analysis highlight possible changes to the model that might lead to sufficient displacement. Well pressure and pore pressure reduction shows a significant displacement increase, implying that other stress conditions might be more suitable to form a sealing barrier. It is also expected that combining well pressure reduction with heating would lead to even more displacement. A lower dilatancy angle suggest more displacement at the borehole wall, and according to Vermeer and de Borst (1984) and Bauer et al. (2017) the dilatancy angle of shale formations are generally lower than that used in this FEA. It also appears that a larger thermal expansion coefficient of the matrix may cause higher displacement. Albeit, case 1 and 6 represent the upper and lower reported values for thermal expansion coefficient of shale matrices (Fjær et al., 2008), and illustrate that the additional displacement is limited.

The yield criterion in the simulations represent weak shale formations, and might not be appropriate for most shale formations. The effect of a stronger yield criterion has not been studied in this thesis, but it is expected to provide less displacement into the borehole due to less plastic deformation. Ultimately, properties of shale formations in the overburden of petroleum wells determine whether they will pose good candidates.

Softening and hardening behavior are associated with shale, but were not included in the FEA for simplicity. It is expected that softening and hardening, respectively, will lead to additional and reduced displacement. Their significance is not studied in this thesis, but might be important

in the context of thermal stimulation of shale barriers. Additionally, the succeeding temperature drop at the borehole when heating ends may hold potential for further development of displacement. There are large amounts of energy stored in the formation, casing and annular fluid, which may lead to moderate temperature development and possibly supplementary displacement when heating ends. Hence, the transition between heating and temperature decrease should be further studied to understand the behavior surrounding the borehole when the active stimulation has ended. These examples show that mechanisms that are not included in the current FEA could lead to more or less displacement. Consequently, these and other mechanisms should be evaluated to determine whether thermal stimulation of shale barriers is a feasible.

5.5.3 Thermal Considerations

The analysis of the coupling coefficient suggest that pore pressure increase with 0.85 MPa for every 1 °C increase for the specified material in the base case, as long as rock failure is not taking place. According to the theoretical change in earth stresses described in Section 2.4.4, change in pore pressure dominate that of earth stresses, and is the driving mechanism behind development of plastic deformation. The thermally induced pore pressure observed is larger than that reported by Chen and Ewy (2005); Bauer et al. (2017). Although, properties of the shale facies in the experiments conducted by Bauer et al. (2017) were not specified and were conducted with undrained conditions. However, it is possible that the simulation yields a value that is too large. A finite element analysis correlated with comparable laboratory experiments could be a applicable benchmark to test whether the pressure-temperature relation in ABAQUS FEA is realistic.

Heating the borehole from 50 °C to 200 °C is very energy intensive and energy requirements will vary with time due to heat dissipating into the casing, annular fluid and the formation where the temperature distribution changes with time. A possible scenario, where energy requirements are moderate, consist of using electricity available on the rig, offshore platform or similar. ESP pumps installed in petroleum wells can supply as much as 750 kW through an electrical cable (Bearden, 2007, p. 648), hence, it is theoretically possible to use heating elements that provide heat in the borehole with equivalent power. Another possible energy source, where more energy is required, is to use exothermic reactions to produce heat in the borehole, such as thermite, which is currently evaluated as a P&A method on its own (Log, 2016). It is emphasized that investigation of energy requirements is not a focus area in this thesis, but these considerations are included to introduce possible operational challenges.

The finite element analysis assume homogeneous properties, however, the 50 m interval where the alleged shale barrier is forming is expected to feature heterogeneous properties. Consequently, different magnitudes of displacement may arise throughout the length of the interval and lead to trapped volume, as depicted in Figure 5.18, where a vertical cross section of a well show shale

displacing into the borehole. The low permeability in the shale may cause a pressure increase in the trapped volume that will prevent further displacement. Several such areas with trapped volume can arise throughout the 50 m barrier interval, and pose an operational challenge for thermal stimulation of shale barriers.

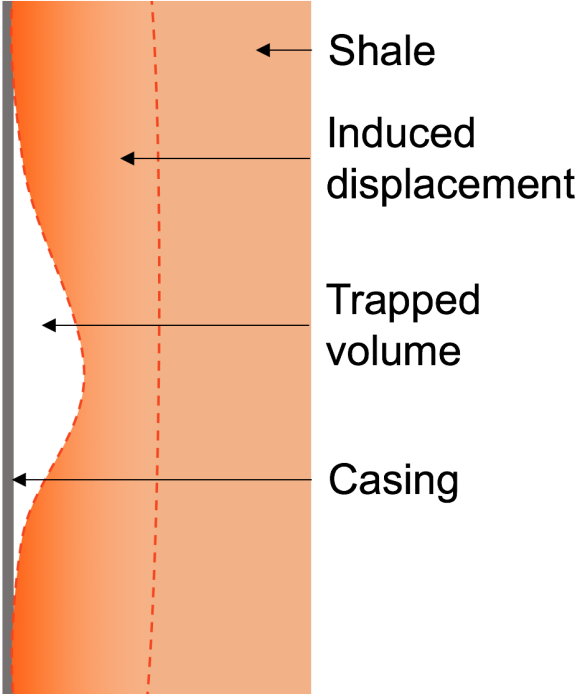


Figure 5.18: Schematic of well cross section highlighting the hypothetical issue with trapped volume due to heterogeneous shale

Thermal stimulation of shale barriers may require as much as 150 °C increase or even more, and heat will dissipate into the casing. The temperature increase on the casing will induce additional axial load because it is constrained from extending. Substantial axial load may lead to wellhead growth or buckling, which can impair well integrity (Mitchell et al., 2011). Consequently, analysis of well integrity should be evaluated in advance of thermal stimulation of the shale barrier. Potentially, this evaluation may lead to an upper bound of temperature in the stimulation, and the new temperature limit must be taken into consideration with respect to the feasibility.

5.5.4 Operational Considerations

In current offshore P&A operations PWC is a common method for establishing a cross sectional barrier. This method use approximately six days to establish a 50 m cross sectional well barrier, and there is a goal to reduce this time to 2 d to 3 d. However, this procedure requires a drilling rig, which is very costly (Rodriguez et al., 2016). The finite element analysis in this report

represent a thermal stimulation spanning over four days. If thermal stimulation of shale barriers will be conducted with a tool that demands a rig, the duration of heating must be lower than 2 d to compete with existing technology in offshore operations. On the other hand, if a tool is developed that can induce shale barriers without the need of a rig, for instance through wireline or coiled tubing, then the duration of heating can be longer and it has the potential for huge cost saving in offshore operations.

5.6 Recommendations for Further Work and Improvements

The ABAQUS model was originally made by SINTEF, where some further developments were implemented in this thesis, described in section 3.1. Through this development and from evaluation of results some possible weaknesses related to the model have been discovered. These are discussed below along with proposals for improvements.

Output parameters, such as radial displacement and radial plastic strain, have been observed to change at the boundaries during the end of the simulation. These effects may have influenced other parameters, such as the pore pressure development where values below the initial condition were observed. This implies that the size of the model is too small, and future models should be larger to avoid boundary effects. As radial displacement generally was positive at the boundaries, it is possible that a larger model would generate more displacement into the borehole as the radial displacement in the far away field converge to zero.

The input parameters in the model are based on typical shale properties, however, benchmarking the FEA is beneficial to validate that the input properties correctly models the behavior of a shale when subject to heating. It is proposed to conduct laboratory experiments on shale samples and develop a finite element model with corresponding properties and conditions. This may reveal shortcomings related to the input parameters and behavior of the model. Furthermore, if the model is able to accurately predict laboratory experiments it strengthens the credibility of the model, and may save cost in potential field tests and future experiments.

A simple setup of temperature reduction was included in the FEA of the base case to study the effects of cooling the borehole when heating ends. Only the displacement resulting from the temperature reduction was reviewed, however, other parameters must be evaluated to understand the mechanisms occurring during this process. Furthermore, the cooling process in this report specify a simplified boundary condition of 50 °C at the borehole wall, which imply that a cooling element must be placed in the well to actively cool the formation, and this is not the intention. If the heating ends, and the borehole is left to equilibrate with the surrounding formation, there will be large amounts of energy stored in the formation, casing and annular fluid leading to a transient temperature reduction. In-situ temperature is found in the far away field, hence temperature will continue to dissipate into the formation, from the warm area near the borehole to the colder far away field. Consequently, the slower temperature reduction may induce even more shale displacement around the borehole, and should therefor be examined.

Including a casing in the finite element analysis is beneficial. This allows direct evaluation of the barrier through the contact between casing and shale material, forces developing on the casing may also be reviewed with respect to well integrity, and possible arching effects resulting from varying displacement around the borehole may be assessed. This will further increase the authenticity of the model and expose possible issues related to interaction between casing and the deforming shale formation.

The finite element model use a plasticity model resembling ductile behavior, thus brittle behavior and conceivable fractures are not evaluated. The high pore pressure increase combined with low radial stress drastically increase the potential for fractures occurring around the circumference of the borehole, known as spalling Li (1998). These fractures would lead to pore pressure reduction during the stimulation, but more importantly, impair the sealing ability of the shale barrier. Thus, brittle behavior should be studied to learn how these effects may be avoided.

A more extensive sensitivity analysis should be conducted to understand which shale properties that are favored to induce a sealing barrier through heating. For instance, softening and hardening effects, different heating schemes at the borehole wall, and more temperature dependent parameters should be included in the model. Furthermore, combining well pressure reduction with heating was suggested as a more effective stimulation technique than heating alone. This hypotheses should be further tested, and the feasibility of this should be evaluated from an operational perspective.

Chapter 6

Conclusion

A shale formation in hollow cylinder geometry subject to heating on the cylinder wall have been evaluated using finite element analysis to simulate thermal stimulation of shale barriers. Important findings are listed below.

- Heating the borehole wall over time induced extensive yielding leading to significant displacement into the borehole.
- Plastic deformation extended deeper into the formation than the initial stress redistribution, indicating that heating is a more effective stimulation technique than reducing well pressure.
- Heating associated pore pressure increase was more important than earth stress increase, resulting in lower effective stress and stress conditions shifting towards the failure envelope.
- A simple simulation of temperature reduction after heating showed that the established shale deformation due to heating does not recede when temperature reduces to its in-situ state.
- Under certain conditions it is highly plausible that heating a borehole in a shale formation will induce sufficient displacement to form a sealing barrier, however, simulations in this report did not generate sufficient displacement.
- Some output parameters were observed to change on the boundaries implying that the size of the finite element model was too small.

The sensitivity analysis conducted on input parameters resulted in the following observations.

- Strong stress concentration surrounding the borehole and lower dilatancy angle were associated with increasing the potential for obtaining an annular seal.
- Thermal expansion coefficient of the matrix is believed to have a limited effect on displacement, where higher values suggest slightly larger displacement.

- Permeability in the nano-darcy range is essential for pore pressure accumulation, and a permeability lower than this did not show any significant effects on the displacement of the borehole wall.
- Combining annular pressure reduction and heating is suggested as a more effective stimulating technique than heating.
- Including temperature dependent parameters depicted significant changes in displacement compared to the base case where parameters were assumed. independent of temperature
- Stress anisotropy resulted in varying displacement around the borehole, and in general, there was more displacement in the direction of minimum horizontal stress.

The results of the finite element analysis show that heating induced shale barriers is a promising stimulation technique, but further development of simulations, laboratory experiments, and field test are required to verify its feasibility.

References

- ABAQUS FEA, 2014. ABAQUS 6.14 Documentation. Dassault Systèmes, Providence, RI, USA.
- Bauer, A., Stenebråten, J. F., Li, L., Fjær, E., 2017. Can heating-induced creep result in shale barriers for p&a applications. In: 51st US Rock Mechanics symposium. American Rock Mechanics Association.
- Bearden, J., 2007. Production Operations Engineering. Vol. 4 of Petroleum Engineering Handbook. Society of Petroleum Engineers, Ch. 13: Electrical Submersible Pumps, pp. 625–711.
- Chen, G., Ewy, R. T., 2005. Thermoporoelastic effect on wellbore stability. SPE Journal 10 (02), 121–129.
- de Souza Neto, E. A., Peric, D., Owen, D. R. J., 2008. Computational Methods for Plasticity. John Wiley & Sons, Incorporated, Chichester.
- Ding, X., Wang, Z., Zhang, G., Li, S., Lin, Q., Jun. 2016. Dilation of shales under triaxial compression. In: 51st US Rock Mechanics symposium. American Rock Mechanics Association, Houston, Texas.
- Evans, T. R., 1977. Thermal properties of north sea rocks. The Log Analyst 18.
- Ferg, T. E., Lund, H.-J., Mueller, D., Myhre, M., Larsen, A., Andersen, P., Lende, G., Hudson, C., Prestegaard, C., Field, D., may 2012. More-effective plug-and-abandonment cementing technique. Journal of Petroleum Technology 64 (05), 132–135.
- Fjær, E., Folstad, J. S., Li, L., jun 2016. How creeping shale may form a sealing barrier around a well. In: 51st US Rock Mechanics symposium. American Rock Mechanics Association, Houston, Texas.
- Fjær, E., Holt, R. M., Horsrud, P., Risnes, R., Raaen, A. M., 2008. Petroleum Related Rock Mechanics, 2nd Edition. Vol. 53 of Developments in petroleum science. Elsevier, Amsterdam, The Netherlands.
- IAPWS-IF97, 2012. Revised release on the iapws industrial formulation 1997 for the thermodynamic properties of water and steam.

-
- Jamieson, D., Tudhope, J., 1970. Physical properties of sea water solutions: thermal conductivity. *Desalination* 8 (3), 393–401.
- Kretzschmar, H. J., Herrmann, S., Feistel, R., Wagner, W., Miyagawa, K., Harvey, A. H., Cooper, J. R., Hiegemann, M., Blangetti, F. L., Orlov, K. A., Weber, I., Singh, A., 2008. The iapws industrial formulation for the thermodynamical properties of seawater.
- Kretzschmar, H. J., Herrmann, S., Kunick, M., Posselt, J., 2013. Zittau's fluid property calculator. [accessed 30.04.2017].
URL https://web1.hszg.de/thermo_fpc/index.php
- Kristiansen, T. G., Oct. 2015. Why shale could be used as a permanent well barrier element. In: P&A Forum. Norsk Olje & Gass, Sola, Norway.
- Li, X., 1998. Thermoporomechanical modelling of inclined boreholes. Ph.D. thesis, University of Oklahoma, Norman, USA.
- Li, X., Cui, L., Roegiers, J.-C., 1999. Temperature induced pore pressure and stresses and their potential impacts on wellbore stability. In: 9th ISRM Congress. International Society for Rock Mechanics, Paris, France, pp. 441–445.
- Log, O., Oct. 2016. Centrica experience with cap rock barrier on canadian land wells. In: P&A Forum. Norsk Olje & Gass, Sola, Norway.
- Millero, F. J., Feistel, R., Wright, D. G., McDougall, T. J., jan 2008. The composition of standard seawater and the definition of the reference-composition salinity scale. *Deep Sea Research Part I: Oceanographic Research Papers* 55 (1), 50–72.
- Mitchell, R. F., Miska, S. Z., Aadnoy, B. S., Barker, J. W., Cunha, J., III, A. W. E., Kastor, R. L., Kelessidis, V. C., Maglione, R., Ozbayoglu, E., Powers, J., Sweatman, R., 2011. *Fundamentals of Drilling Engineering*. Vol. 12 of Spe Textbook Series. Society of Petroleum Engineers, Richardson, TX, USA.
- NORSOK standard D-010 rev. 4, 2013. Well integrity in drilling and well operations.
- Perkins, T. K., Gonzalez, J. A., Apr. 1984. Changes in earth stresses around a wellbore caused by radially symmetrical pressure and temperature gradients. *Society of Petroleum Engineers Journal* 24 (2), 129–140.
- Rodriguez, D., Norum, E., Delabroy, L., Oct. 2016. Perf/wash/cement, best practice: Pwc qualification matrix. In: P&A Forum. Norsk Olje & Gass, Sola, Norway.
- Schön, J. H., 2015. *Physical properties of rocks: Fundamentals and principles of petrophysics*, 2nd Edition. Vol. 65 of *Developments in Petroleum Science*. Elsevier.
- Serway, R. A., Jewett Jr, J. W., 2010. *Physics for Scientists and Engineers with modern physics*, 8th Edition. Cengage Learning, Inc, Belmont, CA, USA.

-
- Somerton, W. H., 1992. Thermal properties and temperature-related behavior of rock/fluid systems. Vol. 37. Elsevier.
- Straume, M., Jun. 2013. Plug and abandonment seminar. In: P&A Forum. Norsk Olje & Gass, Sola, Norway.
- Vermeer, P. A., de Borst, R., 1984. Non-associated plasticity for soils, concrete and rock. *Heron* 29 (3), 1–42.
- Williams, S. M., Carlsen, T., Constable, K. C., Guldahl, A. C., Mar. 2009. Identification and qualification of shale annular barriers using wireline logs during plug and abandonment operations. In: SPE/IADC Drilling Conference and Exhibition. Society of Petroleum Engineers, Amsterdam, The Netherlands.

Appendices

Appendix A

Stresses Around the borehole

For a borehole along a principal stress direction and anisotropic horizontal stresses, stresses around the borehole in cylindrical coordinates are expressed as (Fjær et al., 2008, p. 149)

$$\sigma_r = \frac{\sigma_H + \sigma_h}{2} \left(1 - \frac{r_w^2}{r^2}\right) + \frac{\sigma_H - \sigma_h}{2} \left(1 + 3\frac{r_w^4}{r^4} - 4\frac{r_w^2}{r^2}\right) \cos 2\theta + p_w \frac{r_w^2}{r^2} \quad (\text{A.1})$$

$$\sigma_\theta = \frac{\sigma_H + \sigma_h}{2} \left(1 + \frac{r_w^2}{r^2}\right) - \frac{\sigma_H - \sigma_h}{2} \left(1 + 3\frac{r_w^4}{r^4}\right) \cos 2\theta - p_w \frac{r_w^2}{r^2} \quad (\text{A.2})$$

$$\sigma_z = \sigma_v - 2\nu_{fr}(\sigma_H - \sigma_h) \frac{r_w^2}{r^2} \cos 2\theta \quad (\text{A.3})$$

$$\tau_{r\theta} = -\frac{\sigma_H - \sigma_h}{2} \left(1 - 3\frac{r_w^4}{r^4} + 2\frac{r_w^2}{r^2}\right) \sin 2\theta \quad (\text{A.4})$$

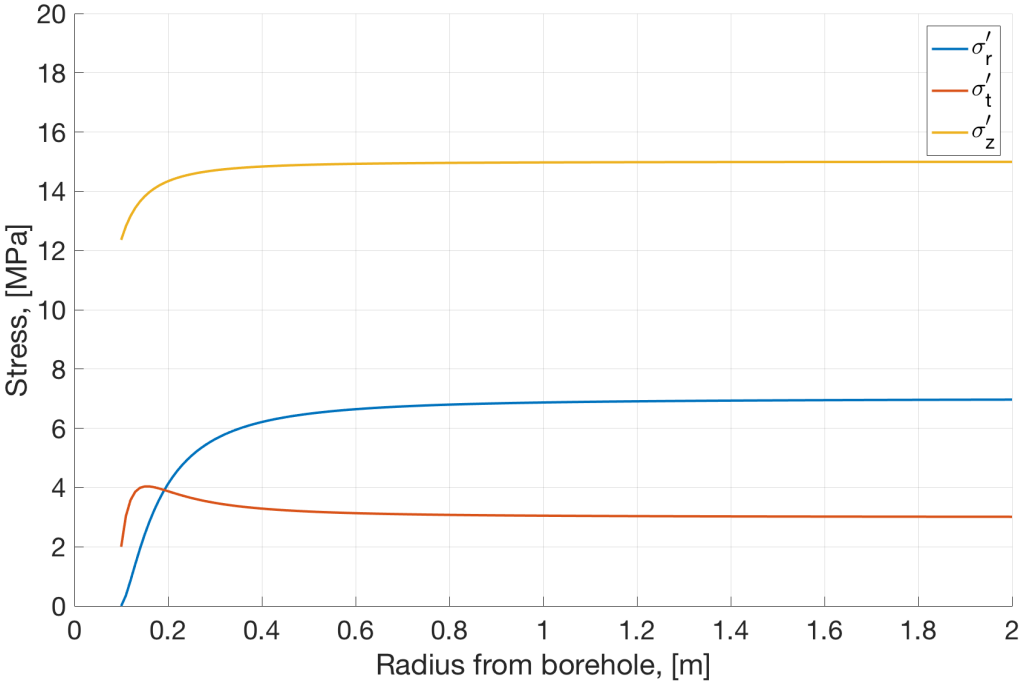
$$\tau_{rz} = \tau_{\theta z} = 0 \quad (\text{A.5})$$

where σ_r , σ_θ and σ_z are stresses surrounding the wellbore in $r\theta z$ -space, σ_h and σ_H are respectively minimum and maximum horizontal stress, σ_v is vertical stress, r is radius, r_w is borehole radius, p_w is well pressure, θ is angle in the borehole ($\theta = 0$ is in the direction of major horizontal stress), τ is shear stress and ν_{fr} is the poisson's ratio of the rock.

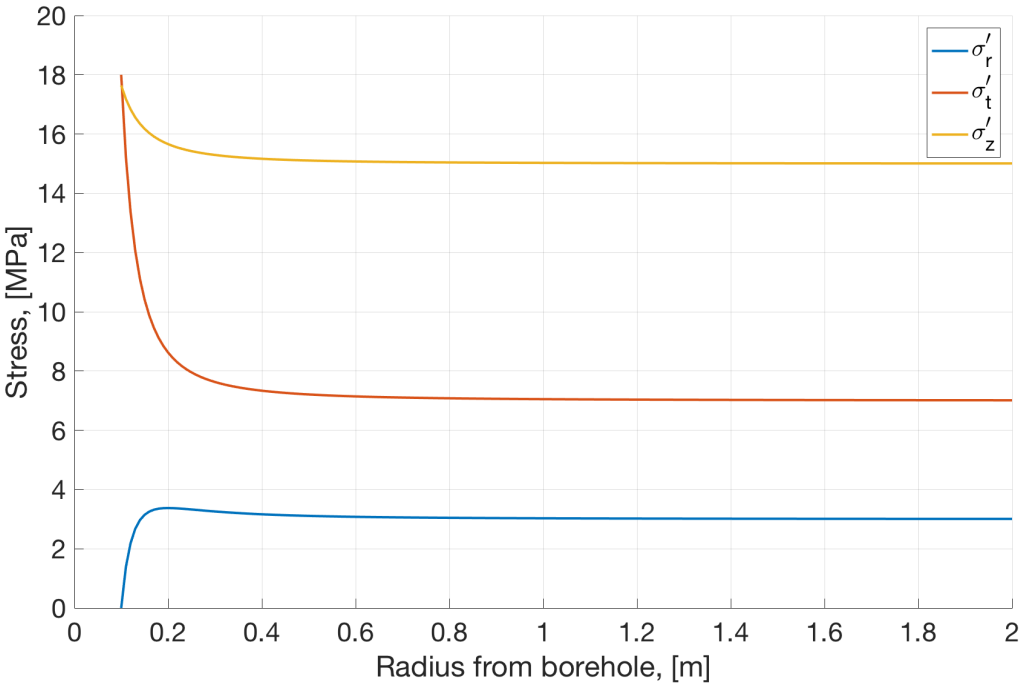
Equations (A.1), (A.2) and (A.3), with the values in table A.1 are used to calculate the stresses in figure A.1. The figures A.1a, and A.1b show how stresses around the borehole develop with distance from the borehole wall for $\theta = 0^\circ$ and 90° .

Table A.1: Values used to calculate stresses around the borehole in figure A.1

r_w	σ_h	σ_H	σ_v	p_f	ν_{fr}
m	MPa	MPa	MPa	MPa	
0.1	18	22	30	15	0.33



(a) $\theta=0^\circ$



(b) $\theta=90^\circ$

Figure A.1: Stresses around a borehole with linearly elastic formation calculated with equations (A.1)-(A.3) for $\theta=0^\circ$ and 90°

Appendix B

Results from the Sensitivity Analysis

B.1 Output Parameters from the Simulations

B.1.1 Case 2

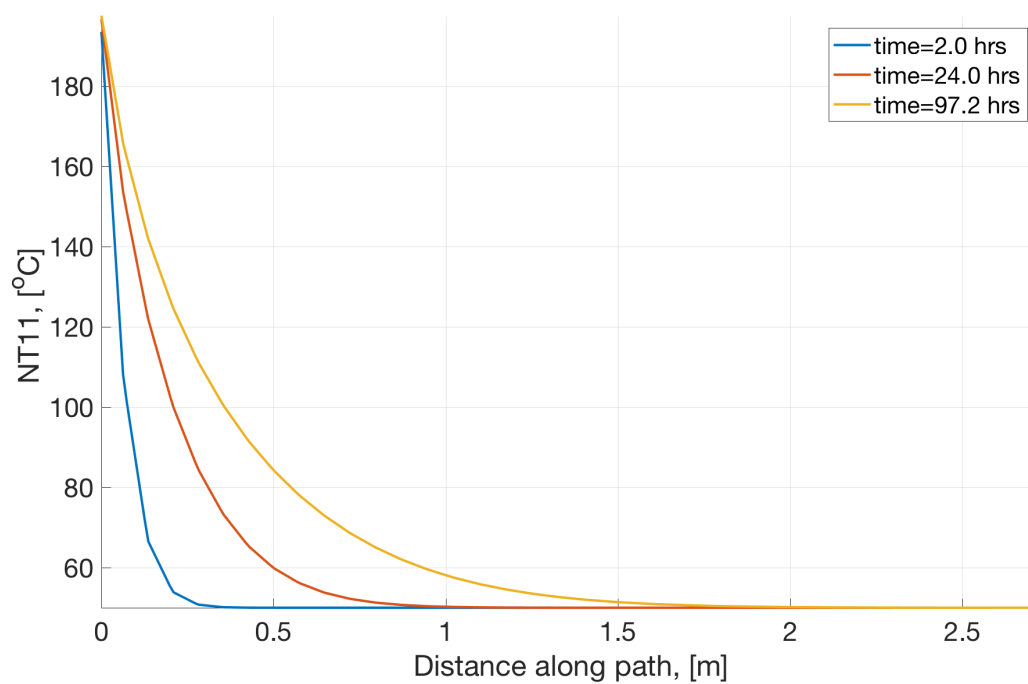


Figure B.1: Case 2, Temperature profile in the formation resulting from the ABAQUS FEA. $r_w = 0.10$ m, $T_0 = 50$ °C

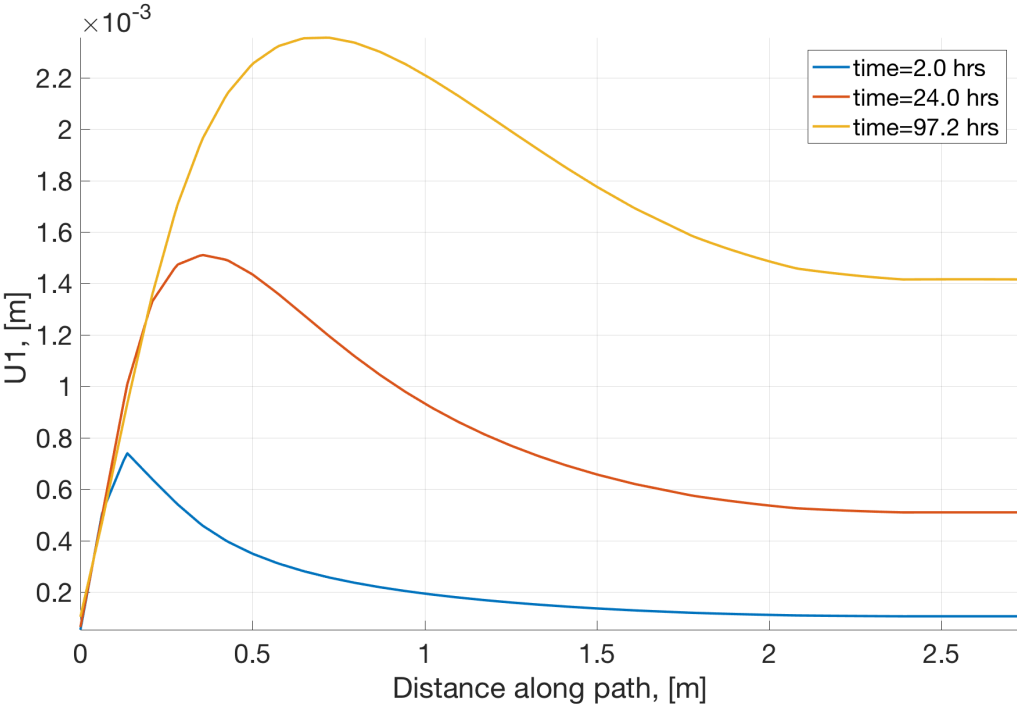


Figure B.2: Case 2, Radial displacement in the formation resulting from the ABAQUS FEA. $r_w = 0.10$ m.

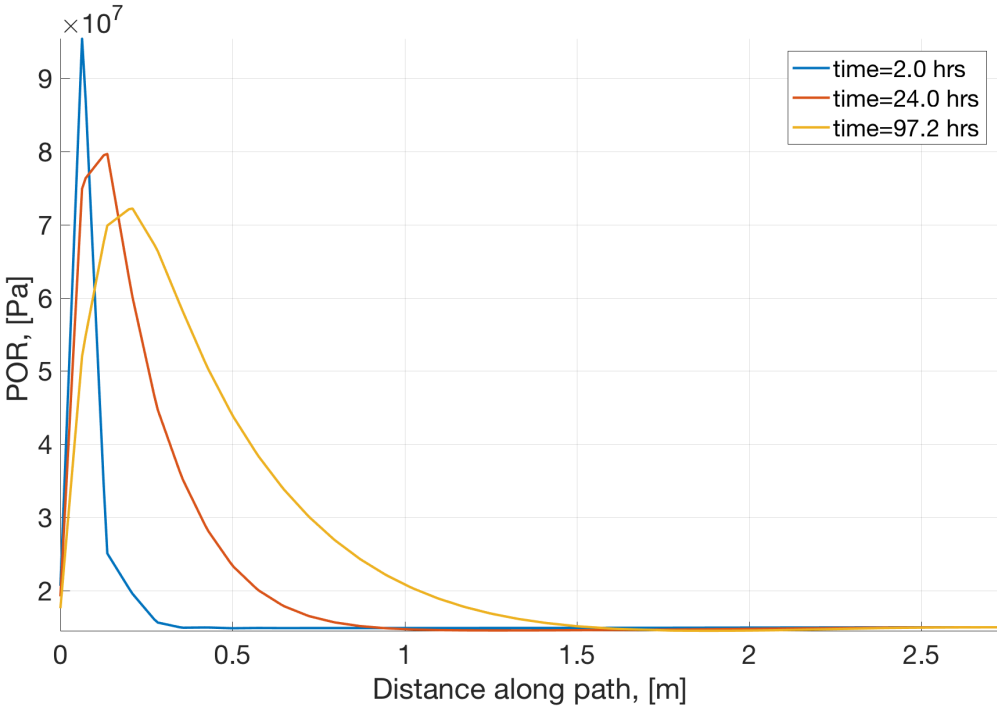


Figure B.3: Case 2, Pore pressure distribution in the formation resulting from the ABAQUS FEA. $r_w = 0.10$ m, $p_{f0} = 15$ MPa.

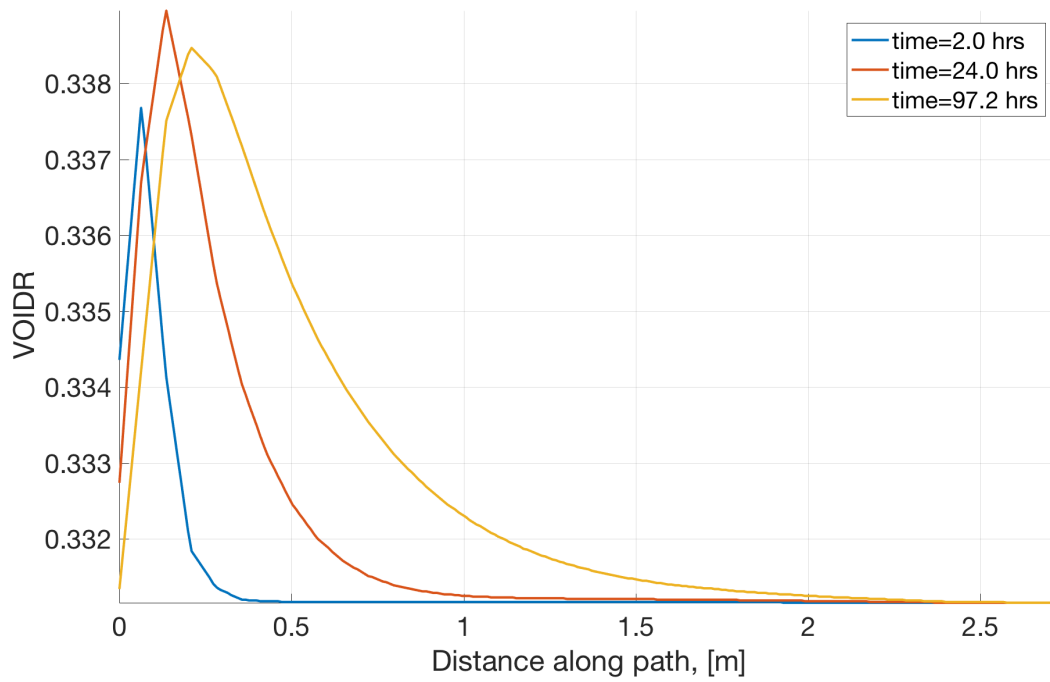


Figure B.4: Case 2, Void ratio distribution in the formation resulting from the ABAQUS FEA. $r_w = 0.10$ m, $e_0 = 0.33$.

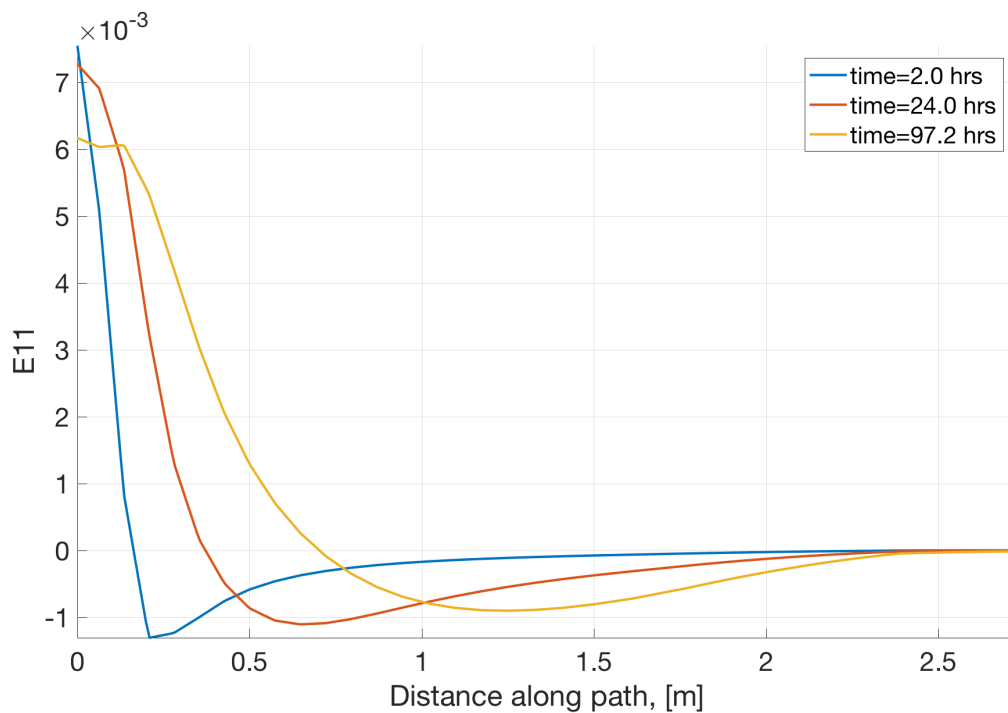


Figure B.5: Case 2, total radial strain in the formation resulting from the ABAQUS FEA. $r_w = 0.10$ m.

B.1.2 Case 3

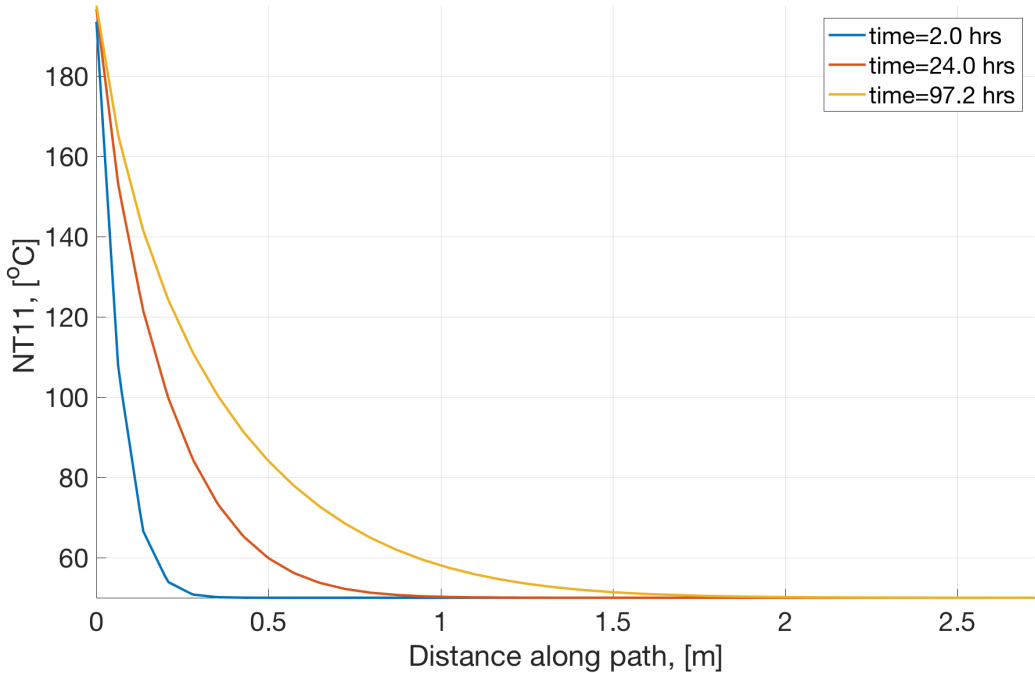


Figure B.6: Case 3, Temperature profile in the formation resulting from the ABAQUS FEA. $r_w = 0.10\text{ m}$, $T_0 = 50\text{ }^\circ\text{C}$

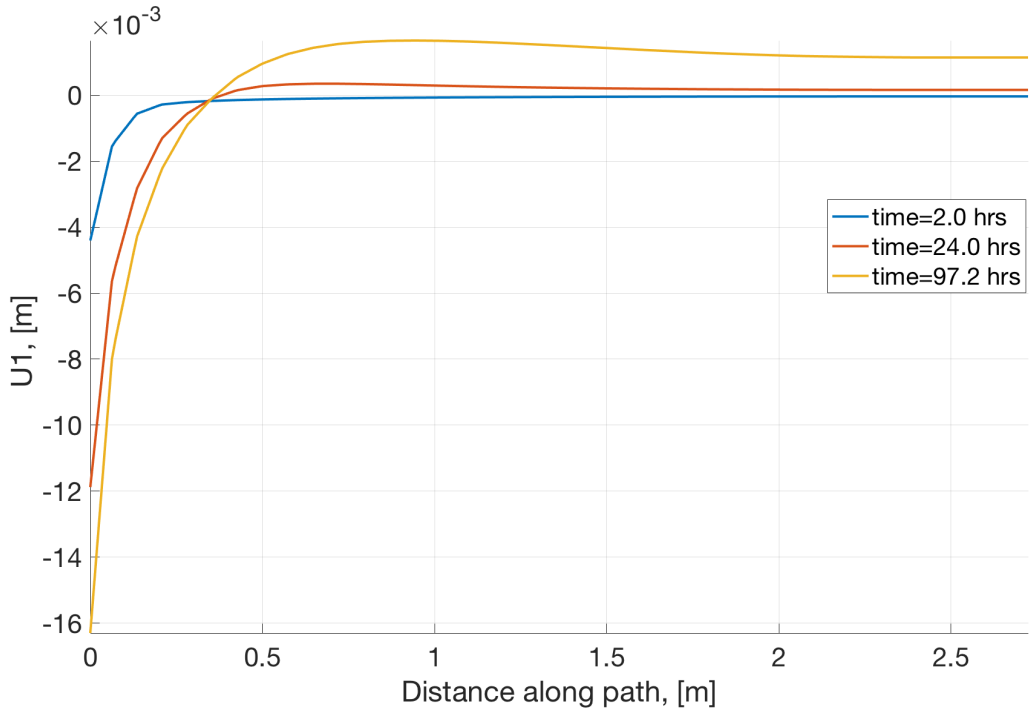


Figure B.7: Case 3, Radial displacement in the formation resulting from the ABAQUS FEA. $r_w = 0.10\text{ m}$.

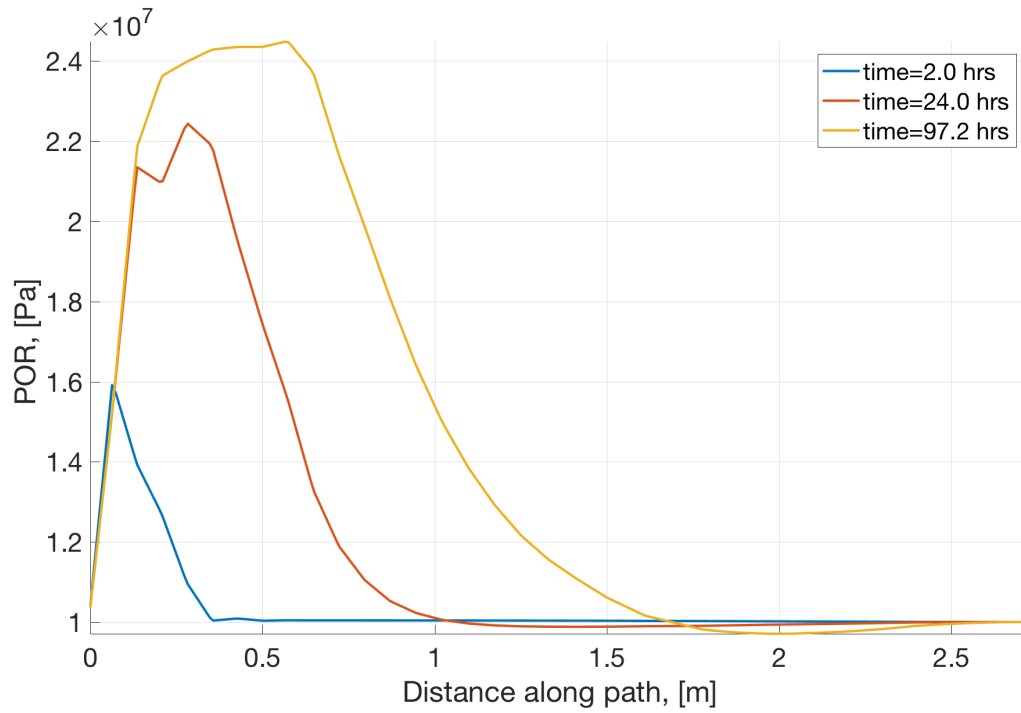


Figure B.8: Case 3, Pore pressure distribution in the formation resulting from the ABAQUS FEA. $r_w = 0.10$ m, $p_{f0} = 10$ MPa.

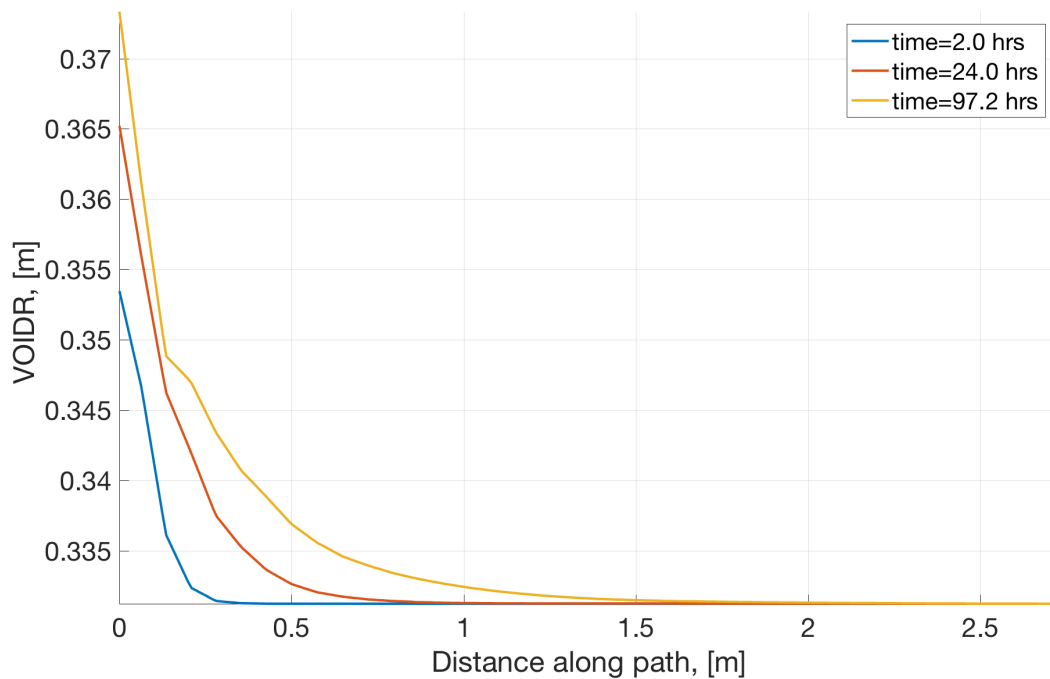


Figure B.9: Case 3, Void ratio distribution in the formation resulting from the ABAQUS FEA. $r_w = 0.10$ m, $e_0 = 0.33$.

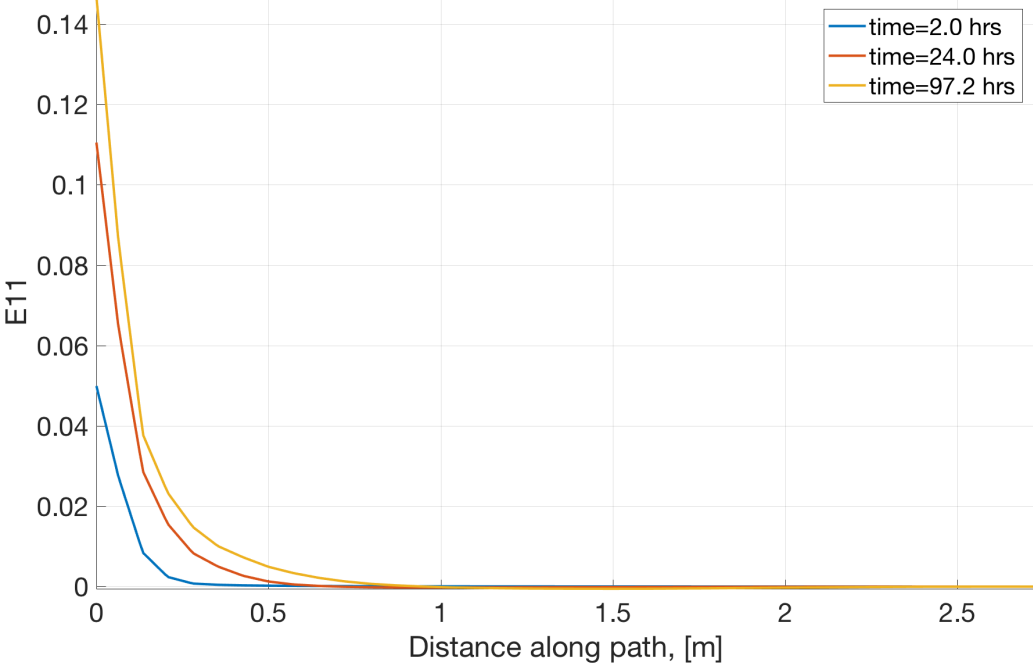


Figure B.10: Case 3, total radial strain in the formation resulting from the ABAQUS FEA. $r_w = 0.10$ m.

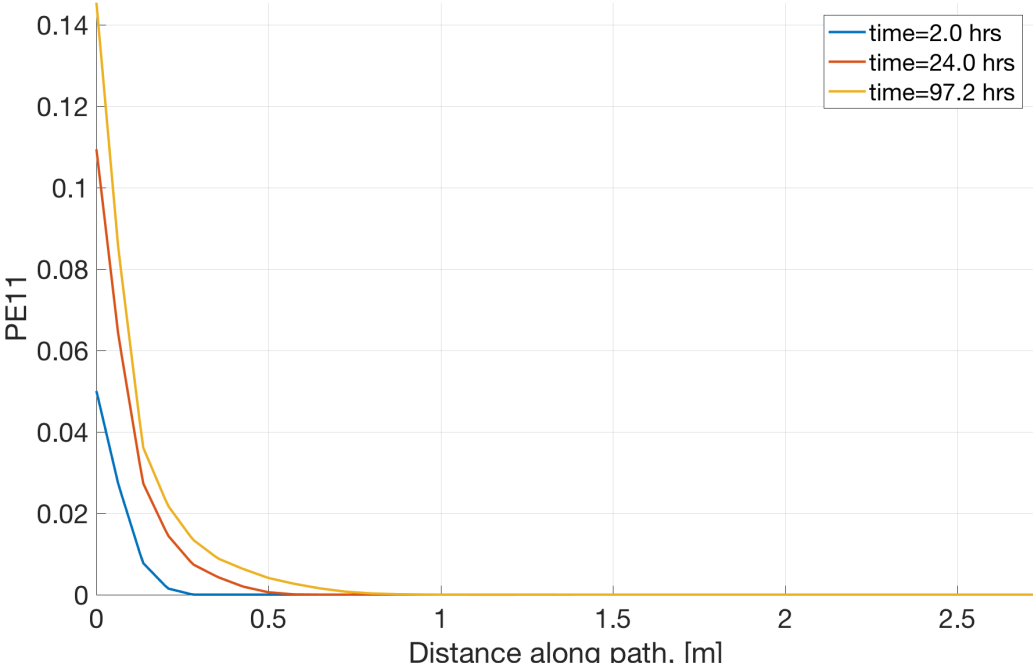


Figure B.11: Case 3, Radial plastic strain in the formation resulting from the ABAQUS FEA. $r_w = 0.10$ m

B.1.3 Case 4

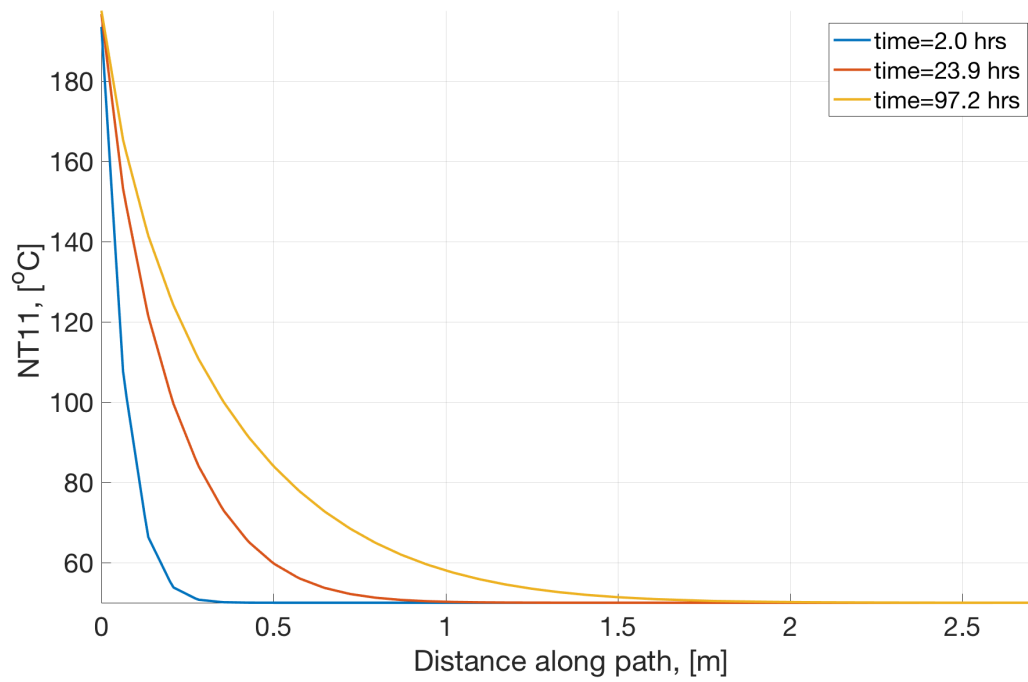


Figure B.12: Case 4, Temperature profile in the formation resulting from the ABAQUS FEA. $r_w = 0.10$ m, $T_0 = 50$ °C

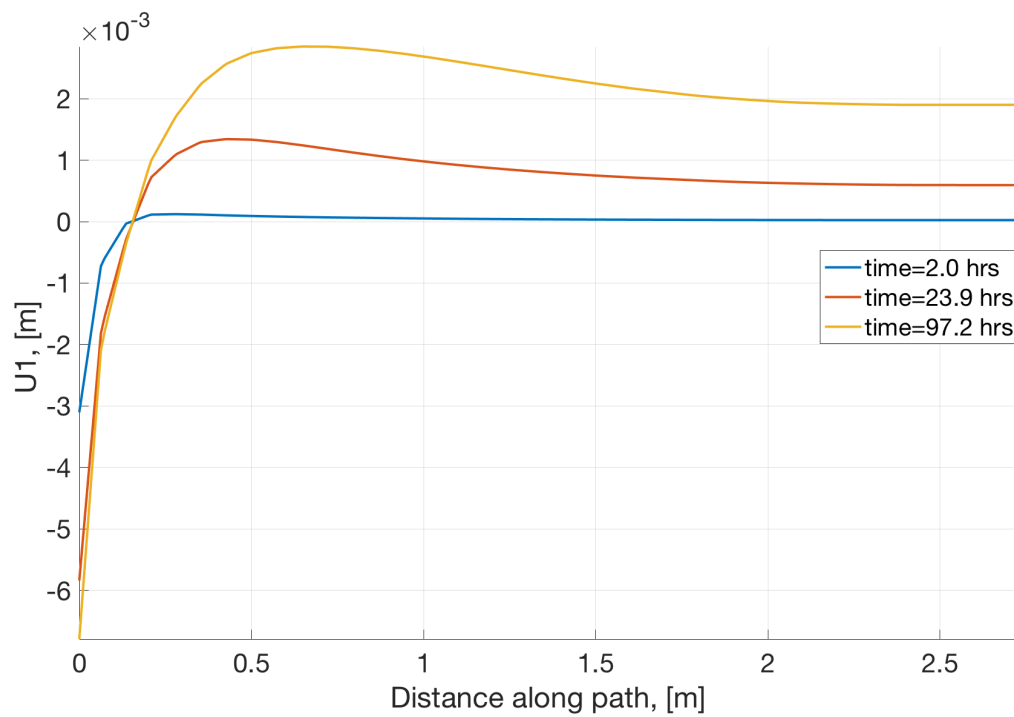


Figure B.13: Case 4, Radial displacement in the formation resulting from the ABAQUS FEA. $r_w = 0.10$ m.

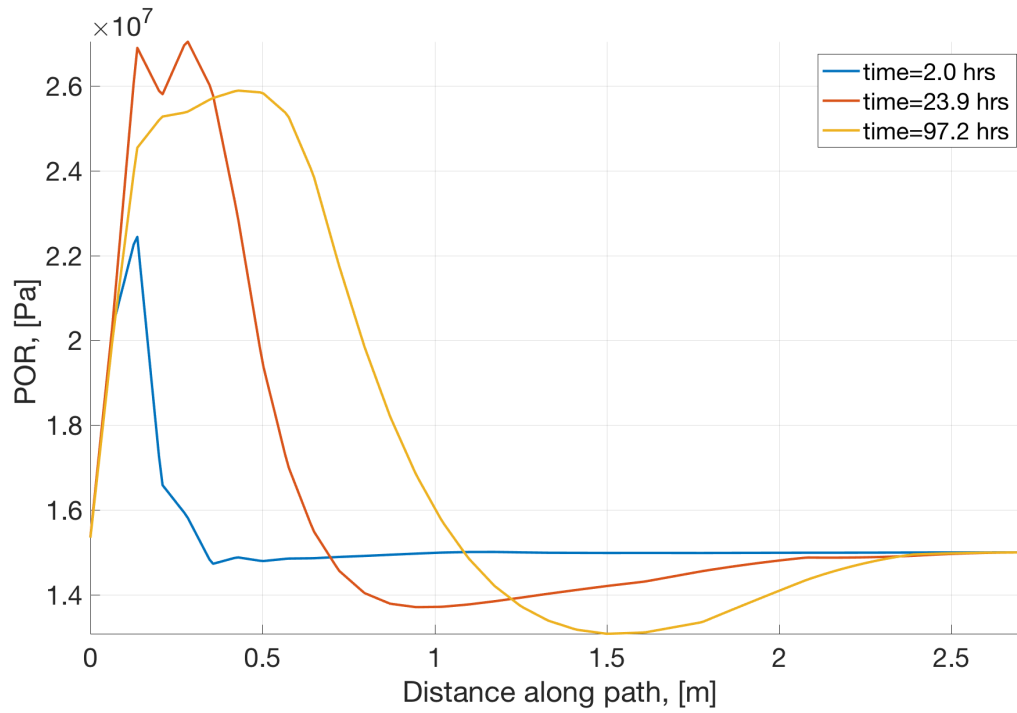


Figure B.14: Case 4, Pore pressure distribution in the formation resulting from the ABAQUS FEA. $r_w = 0.10$ m, $p_{f0} = 15$ MPa.

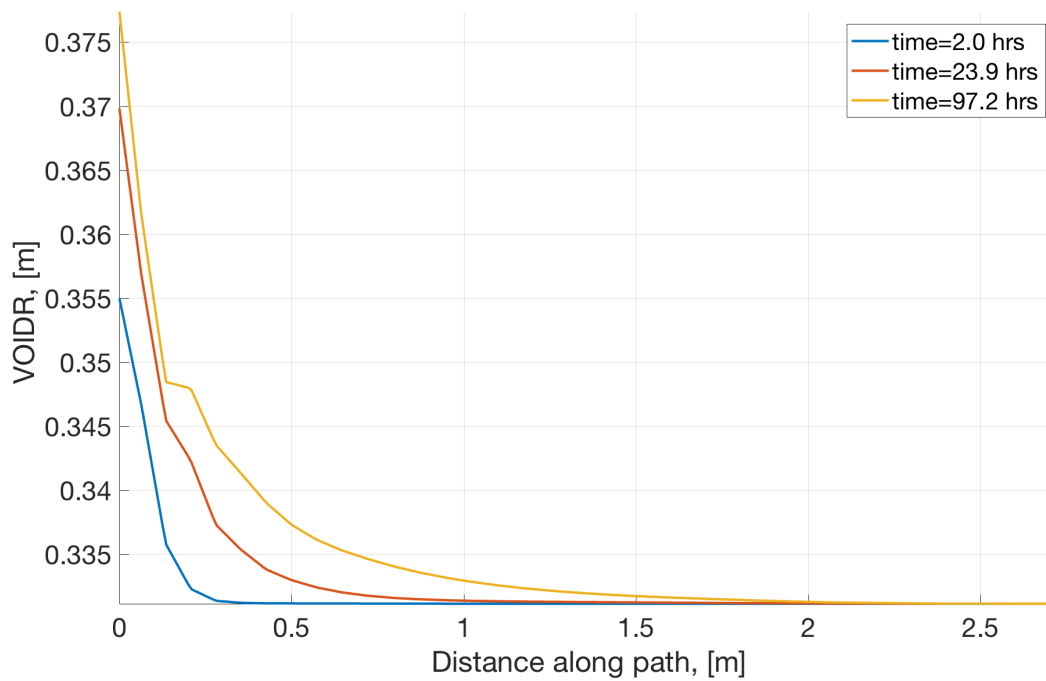


Figure B.15: Case 4, Void ratio distribution in the formation resulting from the ABAQUS FEA. $r_w = 0.10$ m, $e_0 = 0.33$.

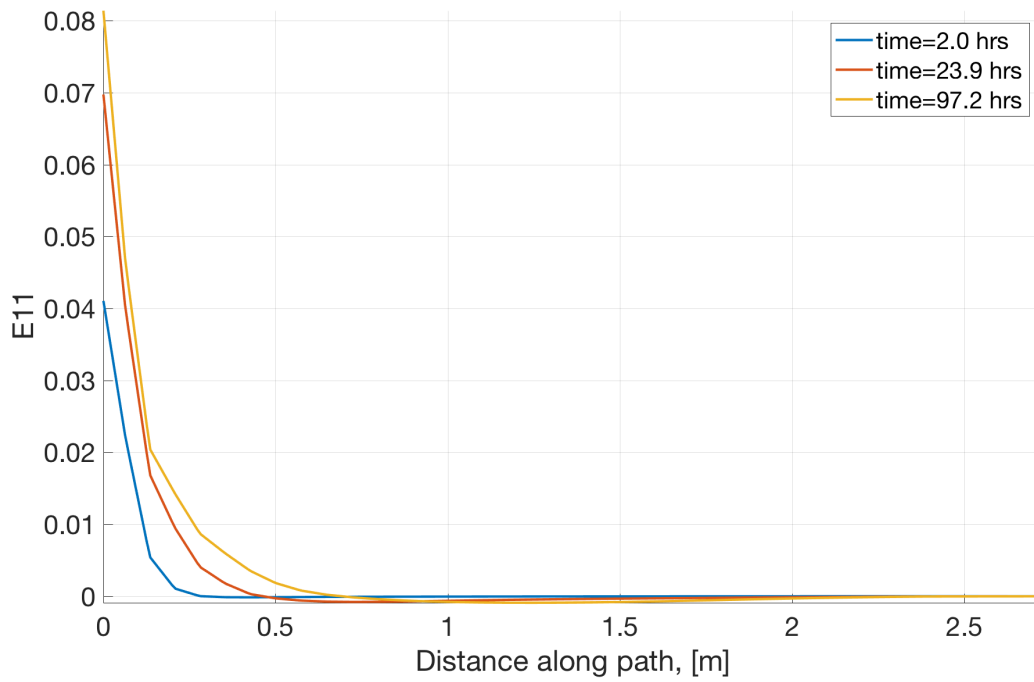


Figure B.16: Case 4, total radial strain in the formation resulting from the ABAQUS FEA. $r_w = 0.10$ m.

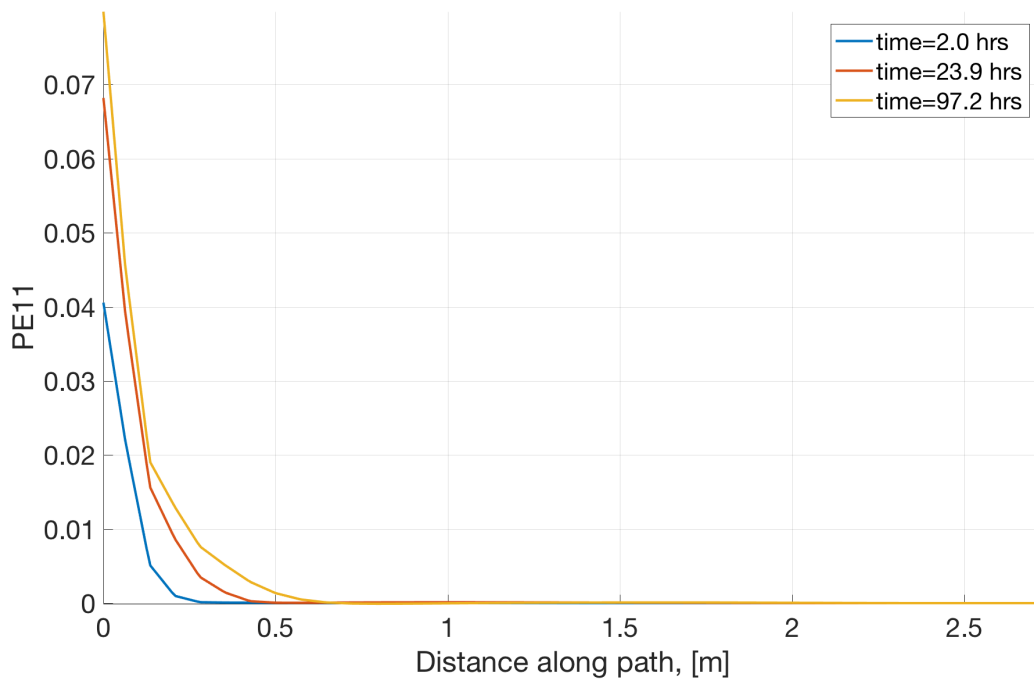


Figure B.17: Case 4, Radial plastic strain in the formation resulting from the ABAQUS FEA. $r_w = 0.10$ m

B.1.4 Case 5

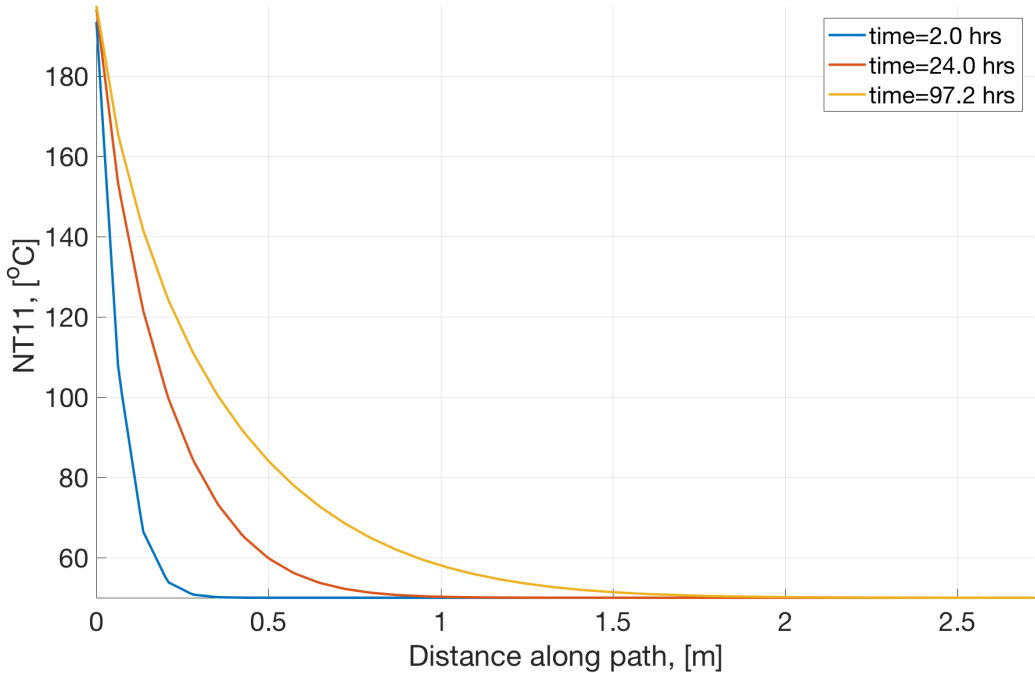


Figure B.18: Case 5, Temperature profile in the formation resulting from the ABAQUS FEA. $r_w = 0.10\text{ m}$, $T_0 = 50\text{ }^\circ\text{C}$

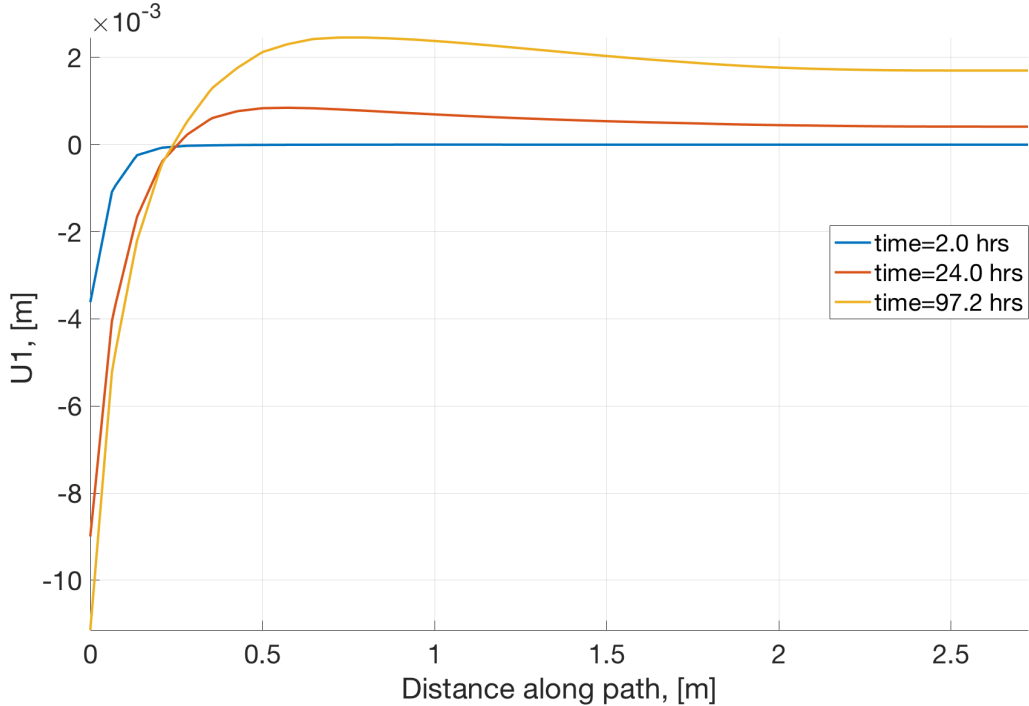


Figure B.19: Case 5, Radial displacement in the formation resulting from the ABAQUS FEA. $r_w = 0.10\text{ m}$.

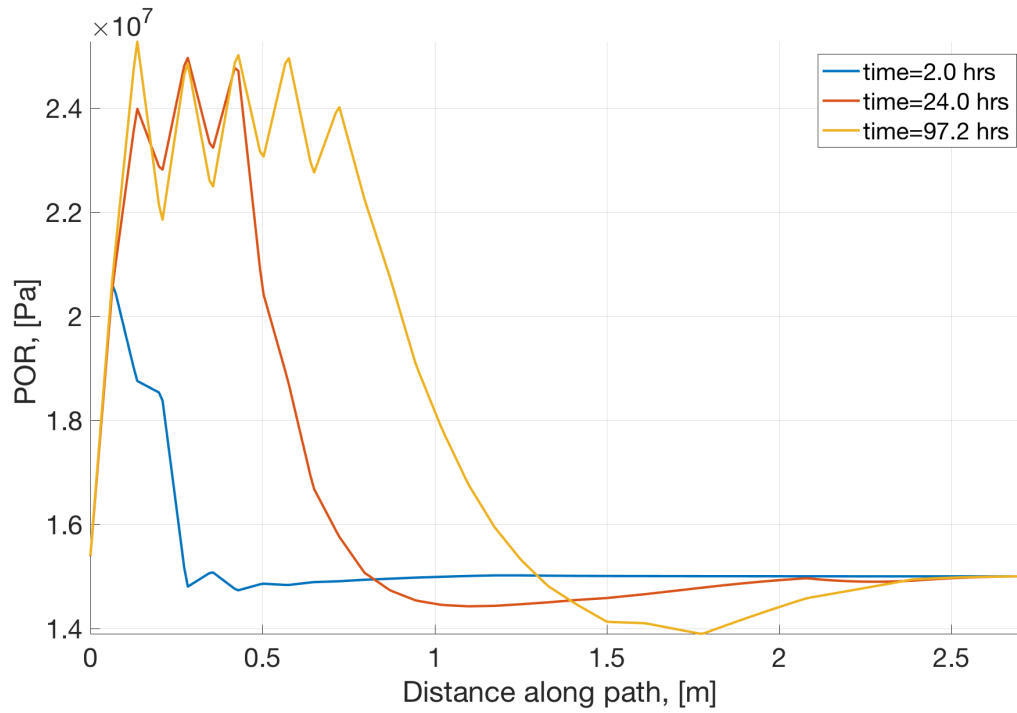


Figure B.20: Case 5, Pore pressure distribution in the formation resulting from the ABAQUS FEA. $r_w = 0.10$ m, $p_{f0} = 15$ MPa.

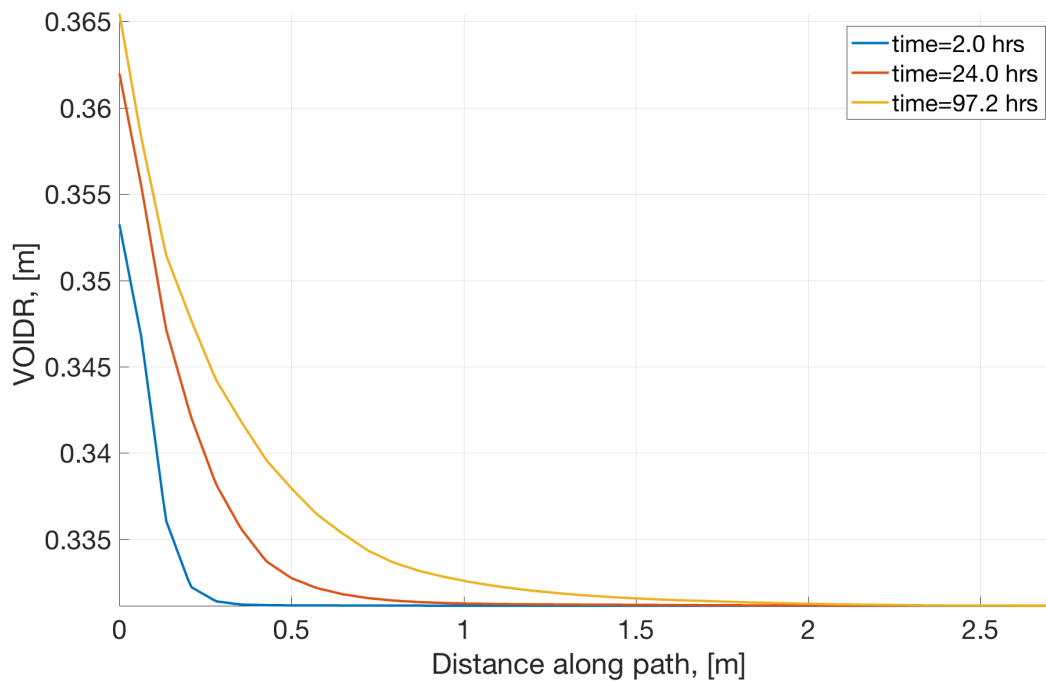


Figure B.21: Case 5, Void ratio distribution in the formation resulting from the ABAQUS FEA. $r_w = 0.10$ m, $e_0 = 0.33$.

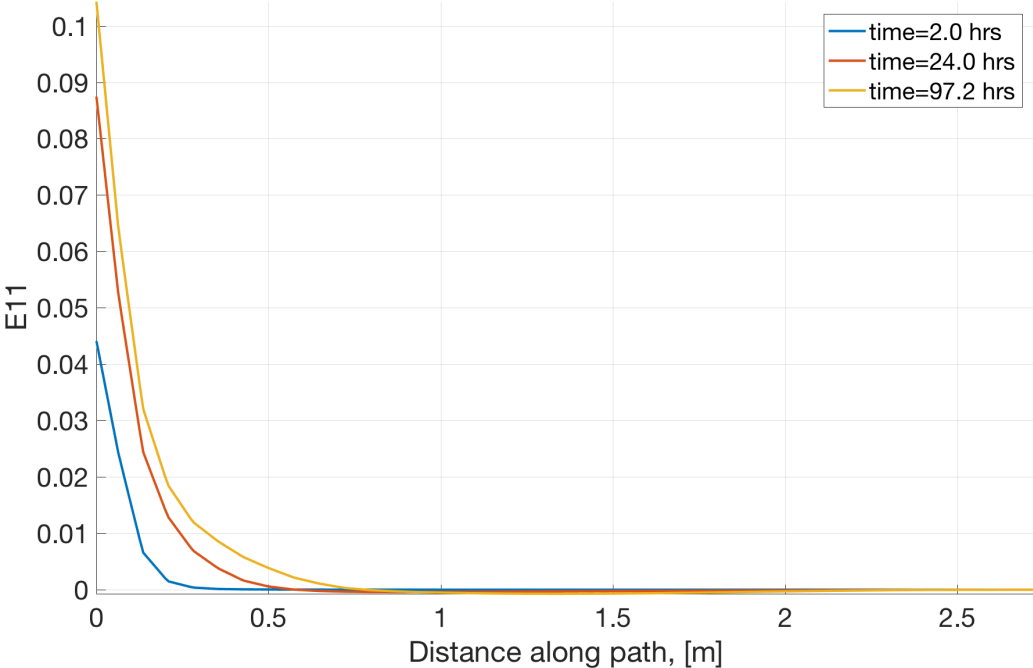


Figure B.22: Case 5, total radial strain in the formation resulting from the ABAQUS FEA. $r_w = 0.10$ m.

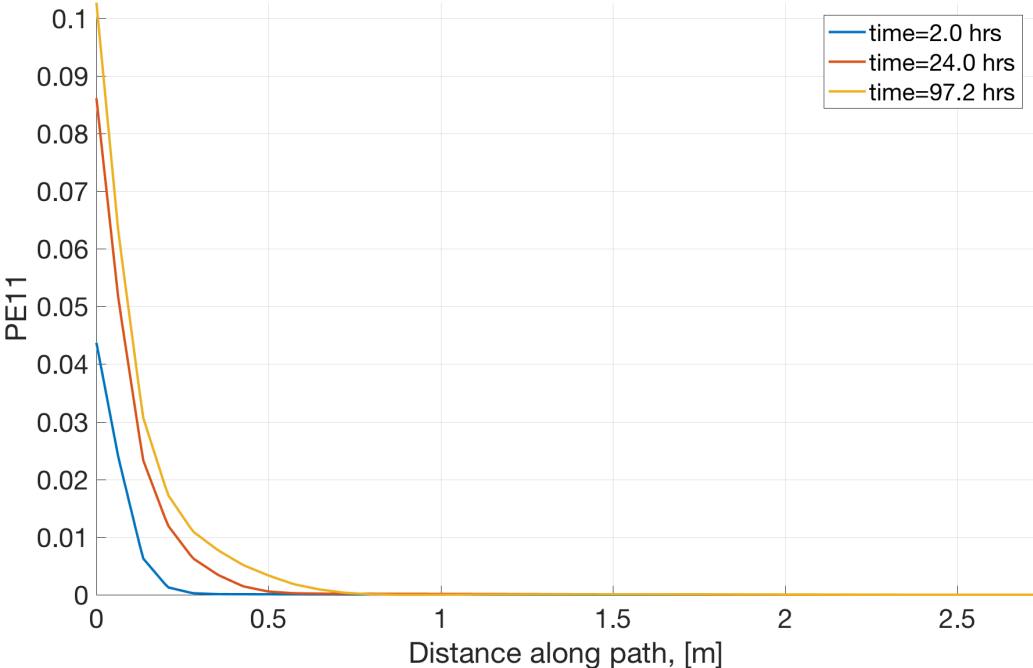


Figure B.23: Case 5, Radial plastic strain in the formation resulting from the ABAQUS FEA. $r_w = 0.10$ m

B.1.5 Case 6

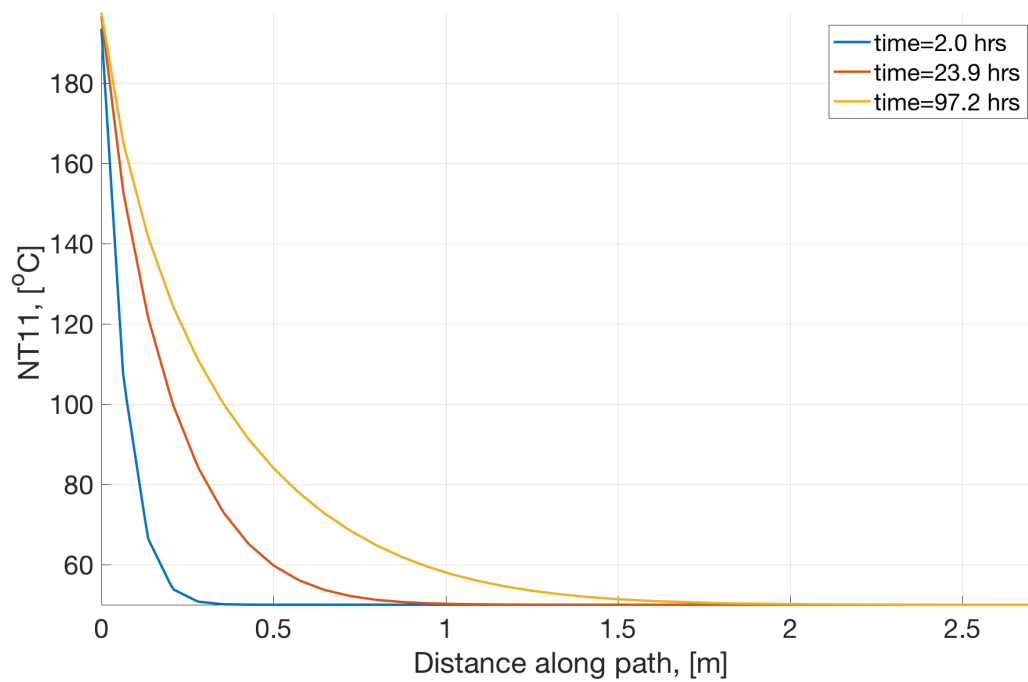


Figure B.24: Case 6, Temperature profile in the formation resulting from the ABAQUS FEA. $r_w = 0.10$ m, $T_0 = 50$ °C

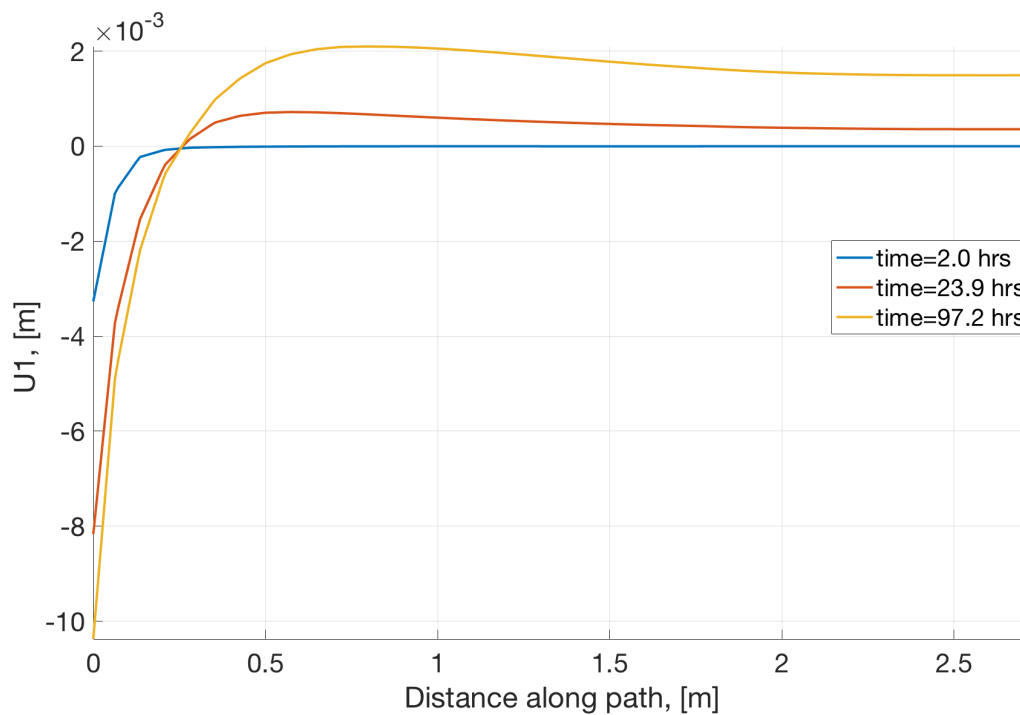


Figure B.25: Case 6, Radial displacement in the formation resulting from the ABAQUS FEA. $r_w = 0.10$ m.

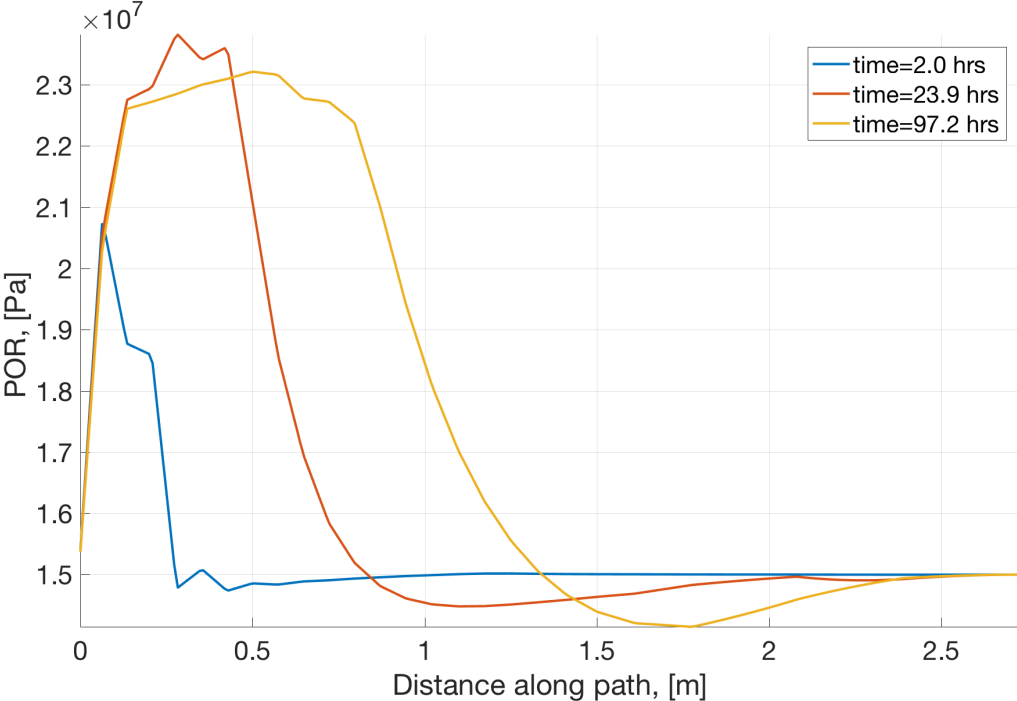


Figure B.26: Case 6, Pore pressure distribution in the formation resulting from the ABAQUS FEA. $r_w = 0.10$ m, $p_{f0} = 15$ MPa.

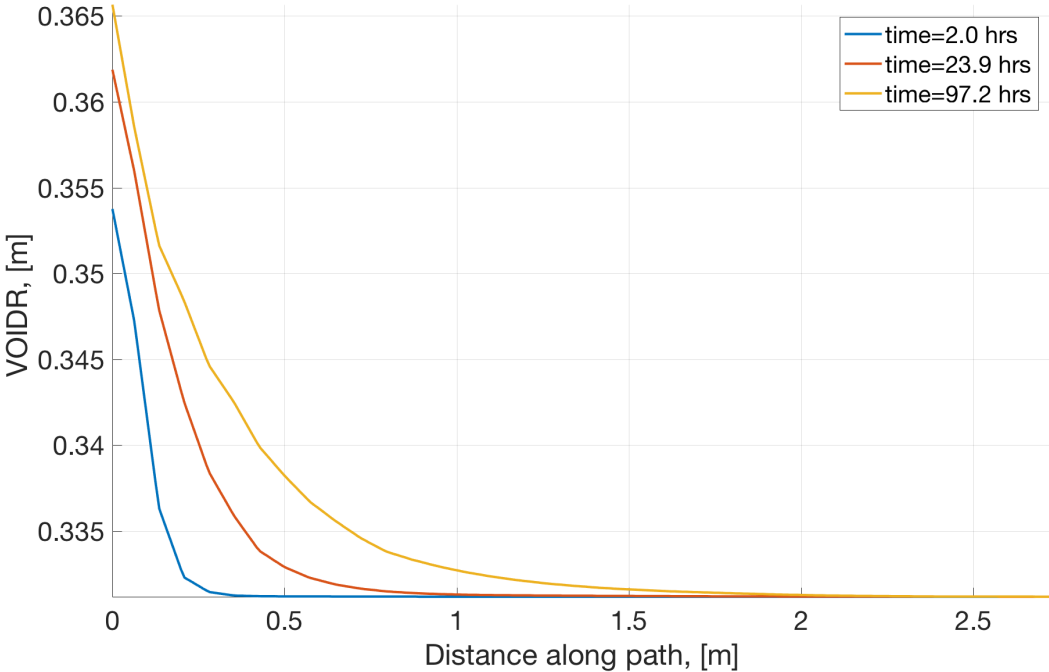


Figure B.27: Case 6, Void ratio distribution in the formation resulting from the ABAQUS FEA. $r_w = 0.10$ m, $e_0 = 0.33$.

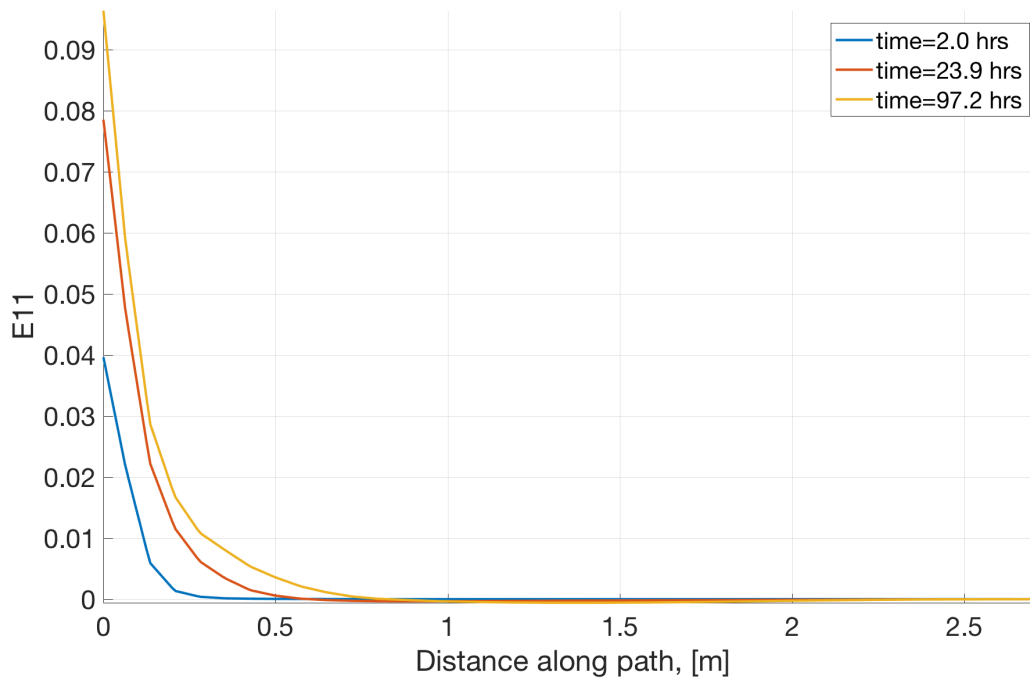


Figure B.28: Case 6, total radial strain in the formation resulting from the ABAQUS FEA. $r_w = 0.10$ m.

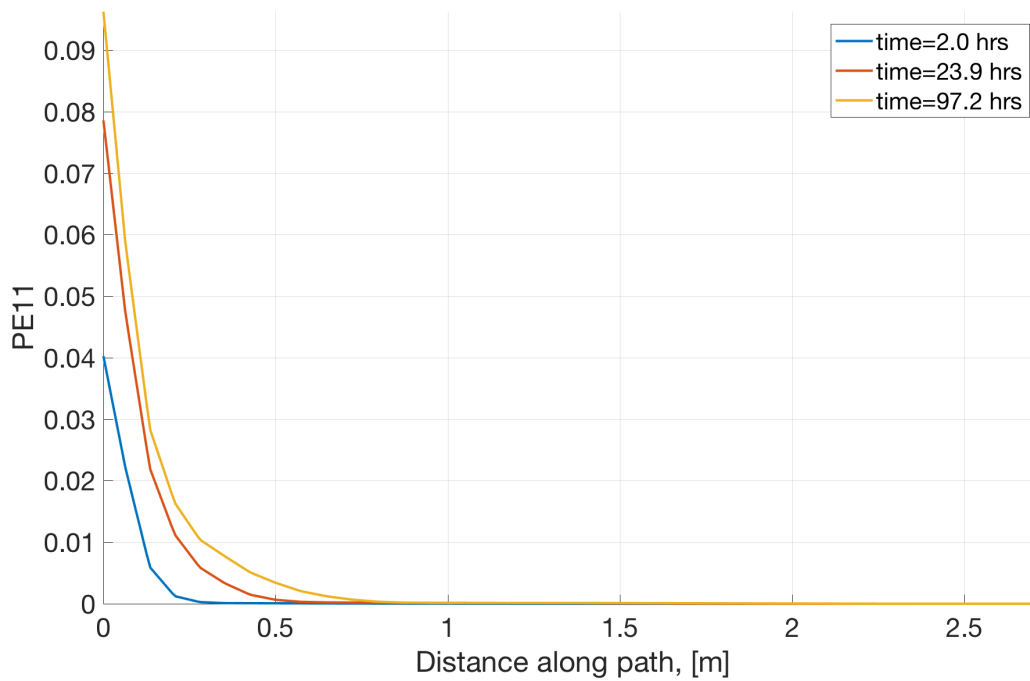


Figure B.29: Case 6, Radial plastic strain in the formation resulting from the ABAQUS FEA. $r_w = 0.10$ m

B.1.6 Case 7

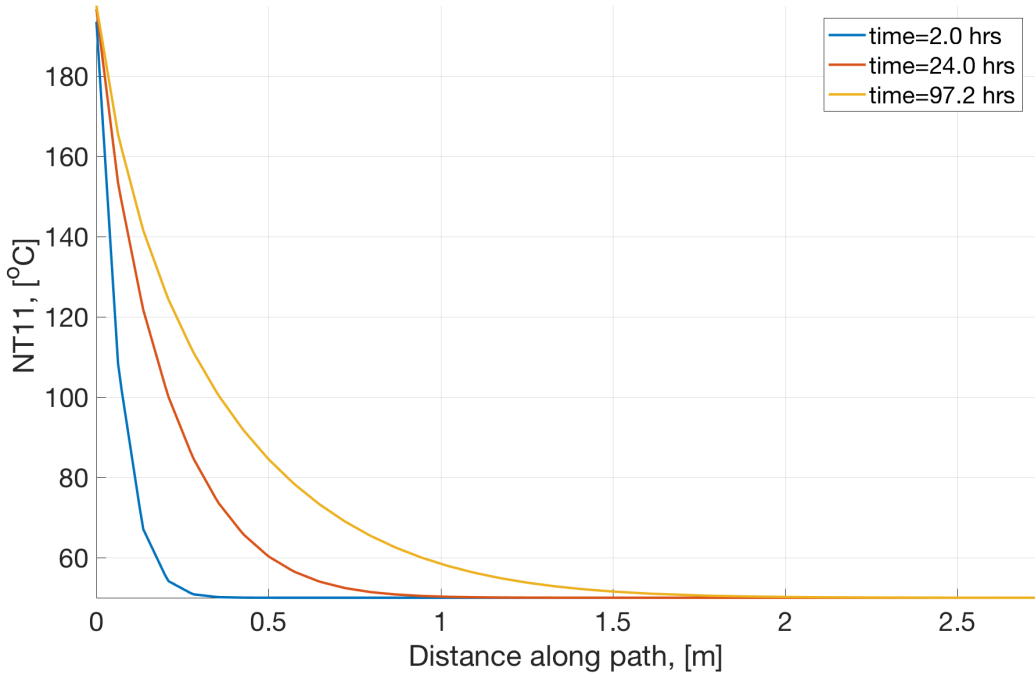


Figure B.30: Case 7, Temperature profile in the formation resulting from the ABAQUS FEA. $r_w = 0.10\text{ m}$, $T_0 = 50\text{ }^\circ\text{C}$

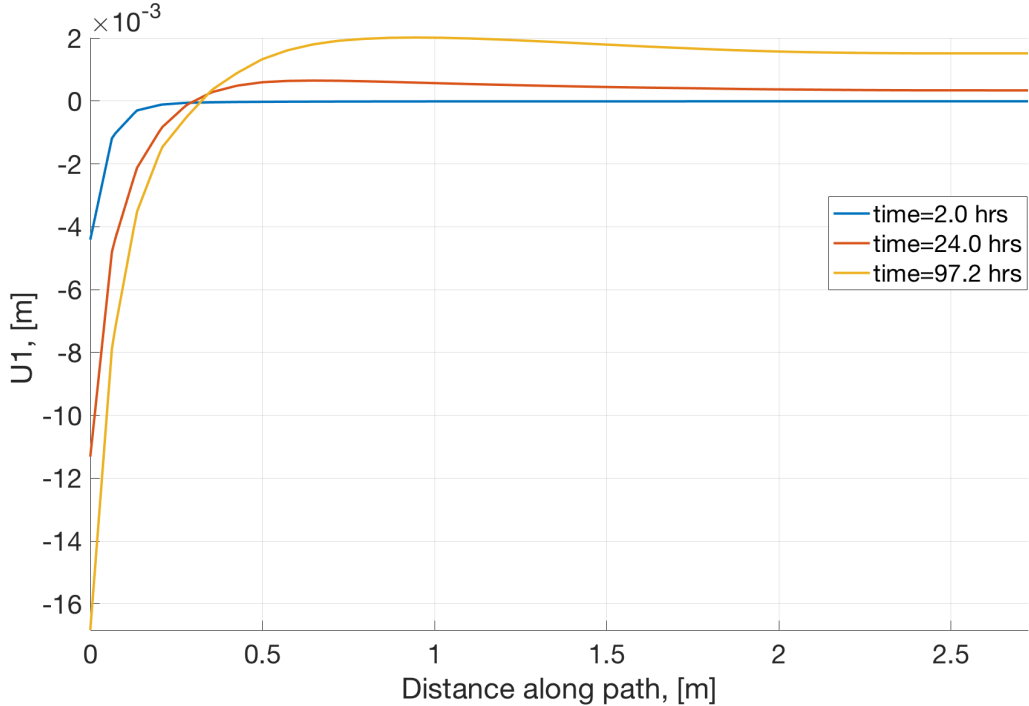


Figure B.31: Case 7, Radial displacement in the formation resulting from the ABAQUS FEA. $r_w = 0.10\text{ m}$.

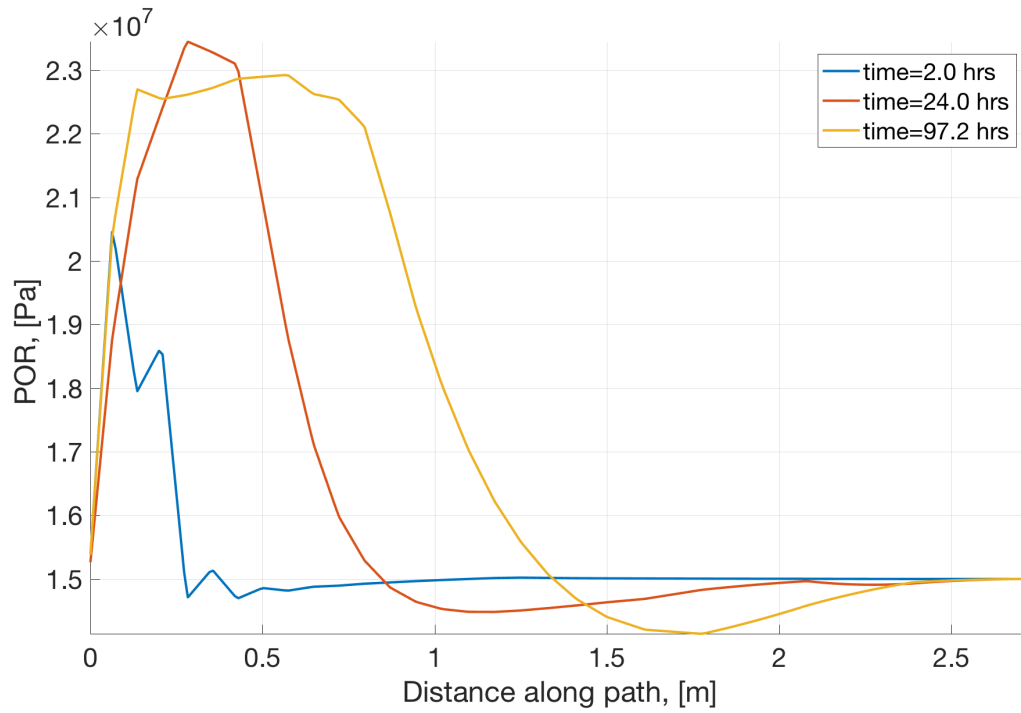


Figure B.32: Case 7, Pore pressure distribution in the formation resulting from the ABAQUS FEA. $r_w = 0.10$ m, $p_{f0} = 15$ MPa.

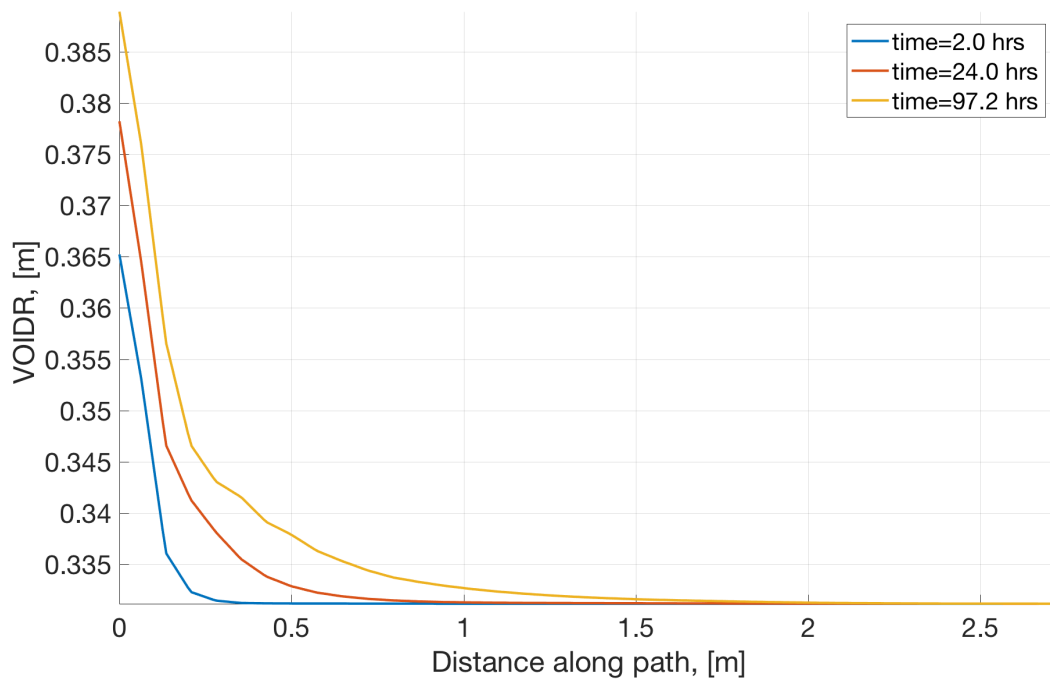


Figure B.33: Case 7, Void ratio distribution in the formation resulting from the ABAQUS FEA. $r_w = 0.10$ m, $e_0 = 0.33$.

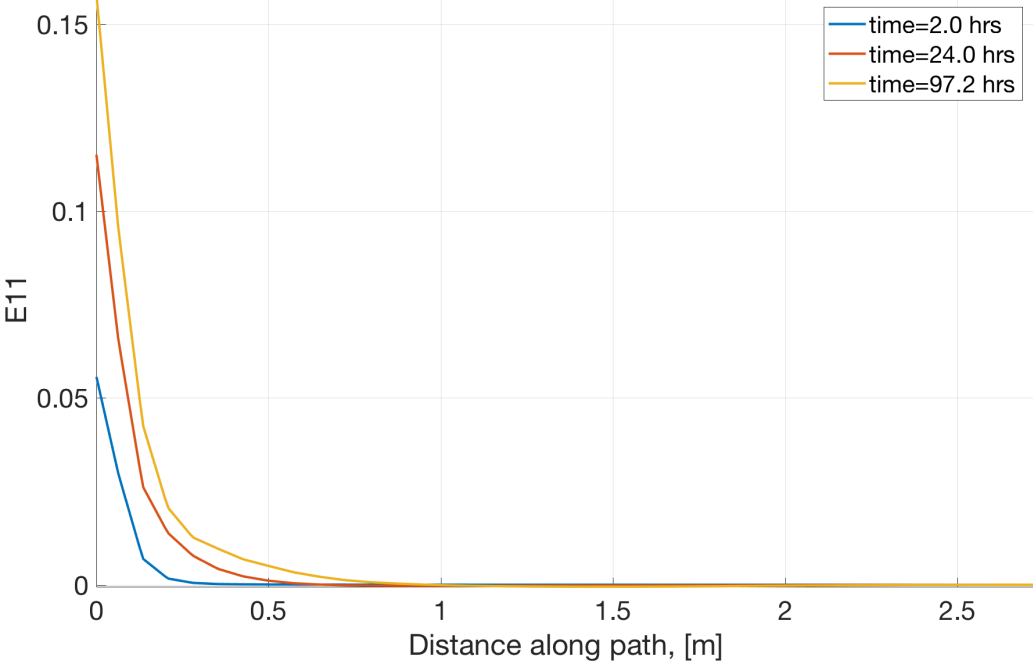


Figure B.34: Case 7, total radial strain in the formation resulting from the ABAQUS FEA. $r_w = 0.10$ m.

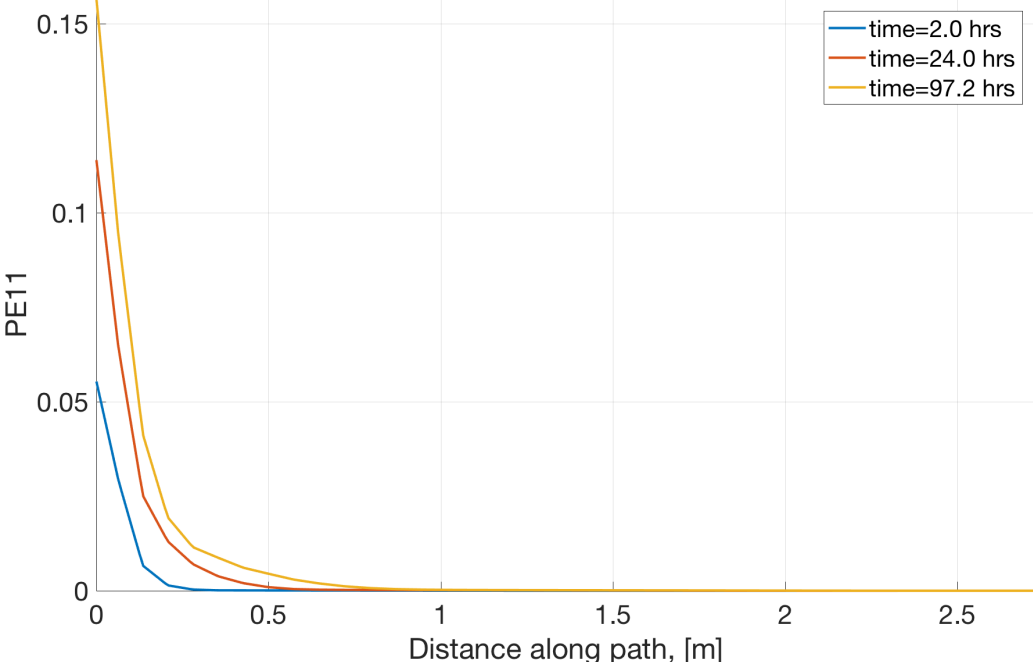


Figure B.35: Case 7, Radial plastic strain in the formation resulting from the ABAQUS FEA. $r_w = 0.10$ m

B.2 Stress conditions in case 1 and 3

B.2.1 Case 1

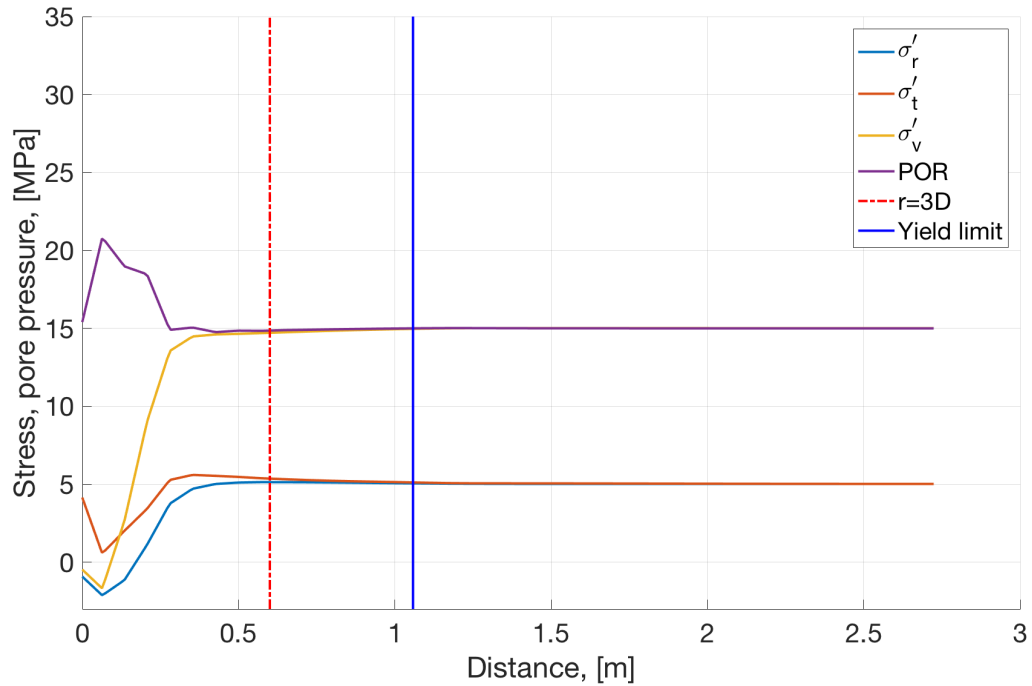


Figure B.36: Case 1 - Stress conditions at $t=0.3$ h. Red stippled vertical line marks distance from the borehole wall equal 3 times borehole diameter. To the left the blue vertical line plastic strain has occurred

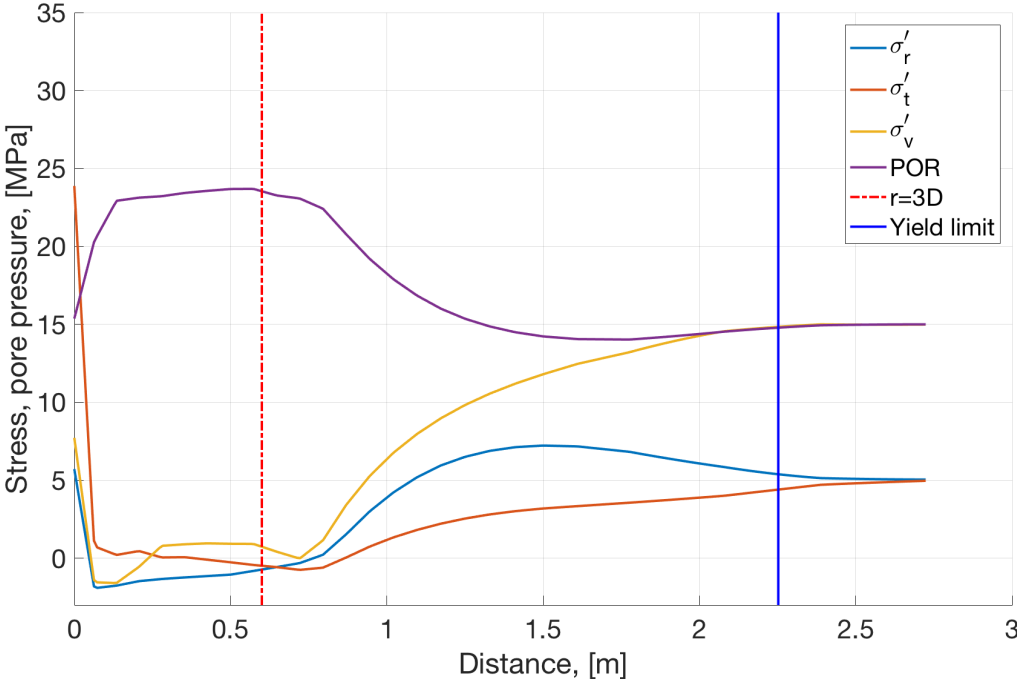


Figure B.37: Case 1 - Stress conditions at t=96.7 h. Red stippled vertical line marks distance from the borehole wall equal 3 times borehole diameter. To the left the blue vertical line plastic strain has occurred

B.2.2 Case 3

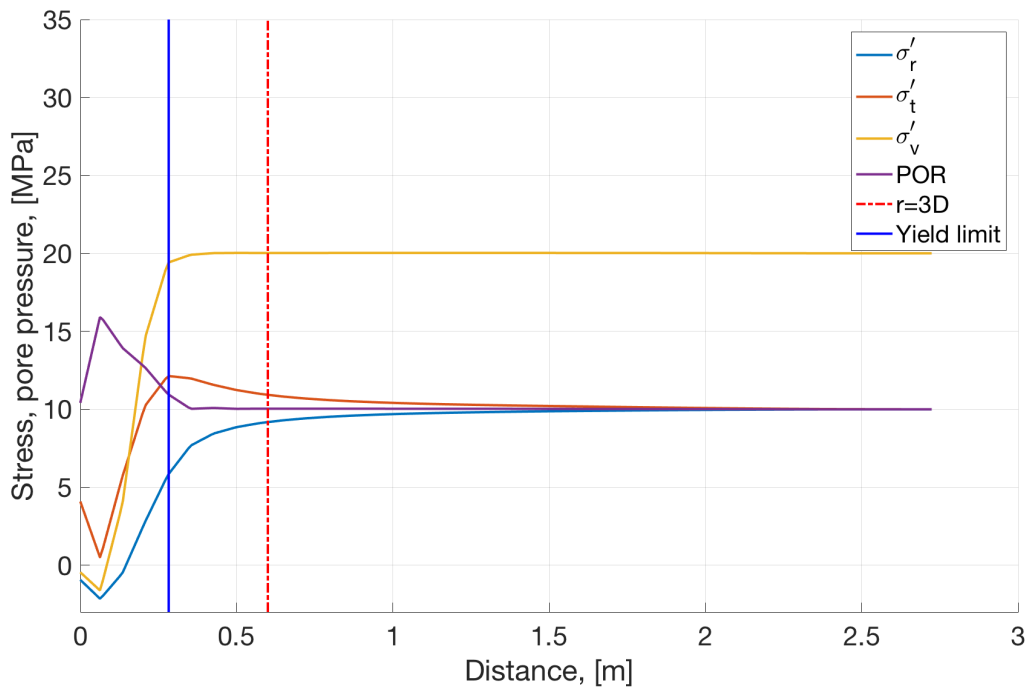


Figure B.38: Case 3 - Stress conditions at $t=0.3$ h. Red stippled vertical line marks distance from the borehole wall equal 3 times borehole diameter. To the left the blue vertical line plastic strain has occurred

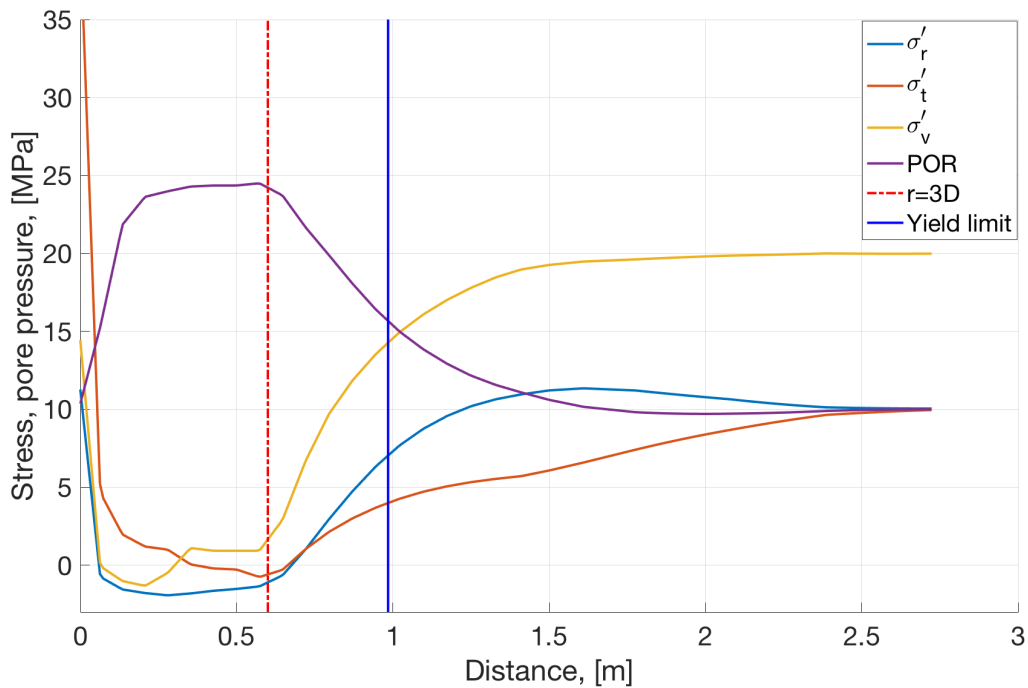


Figure B.39: Case 3 - Stress conditions at $t=97.1$ h. Red stippled vertical line marks distance from the borehole wall equal 3 times borehole diameter. To the left the blue vertical line plastic strain has occurred

B.3 The Pressure-Temperature relation

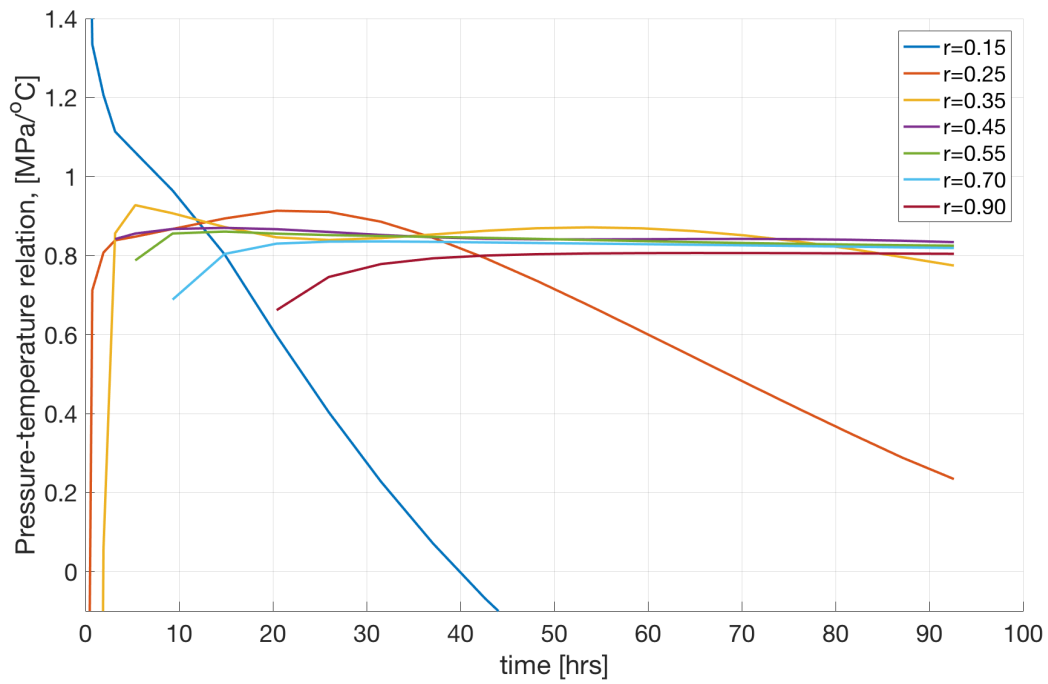


Figure B.40: Pressure-temperature relation, for case 2 at different radii from the borehole wall as function of time

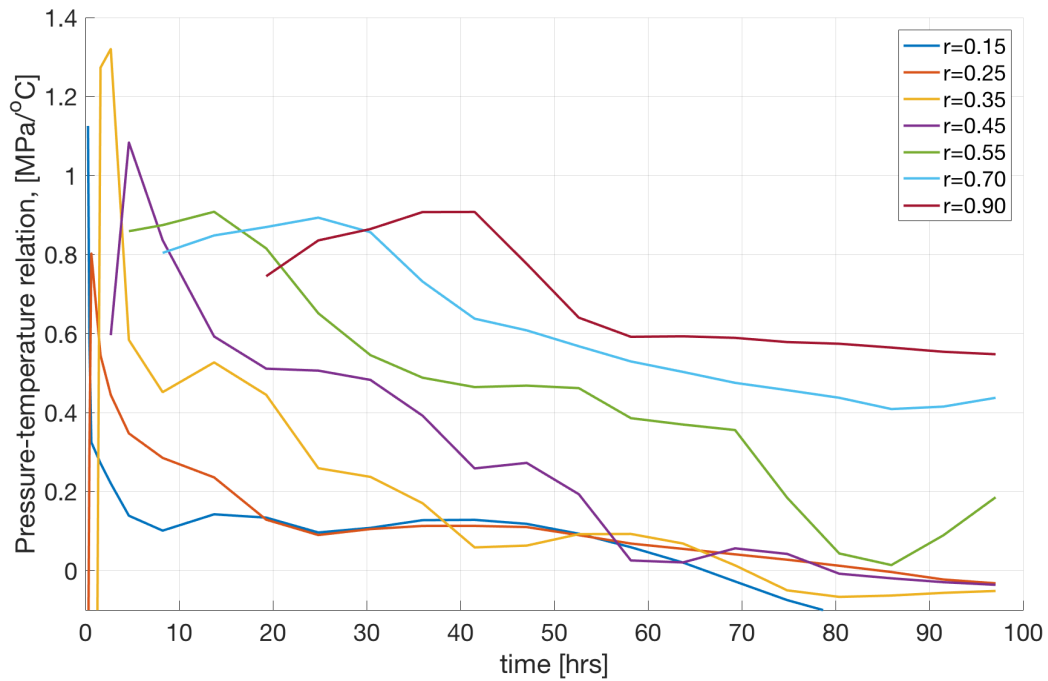


Figure B.41: Pressure-temperature relation, for case 3 at different radii from the borehole wall as function of time

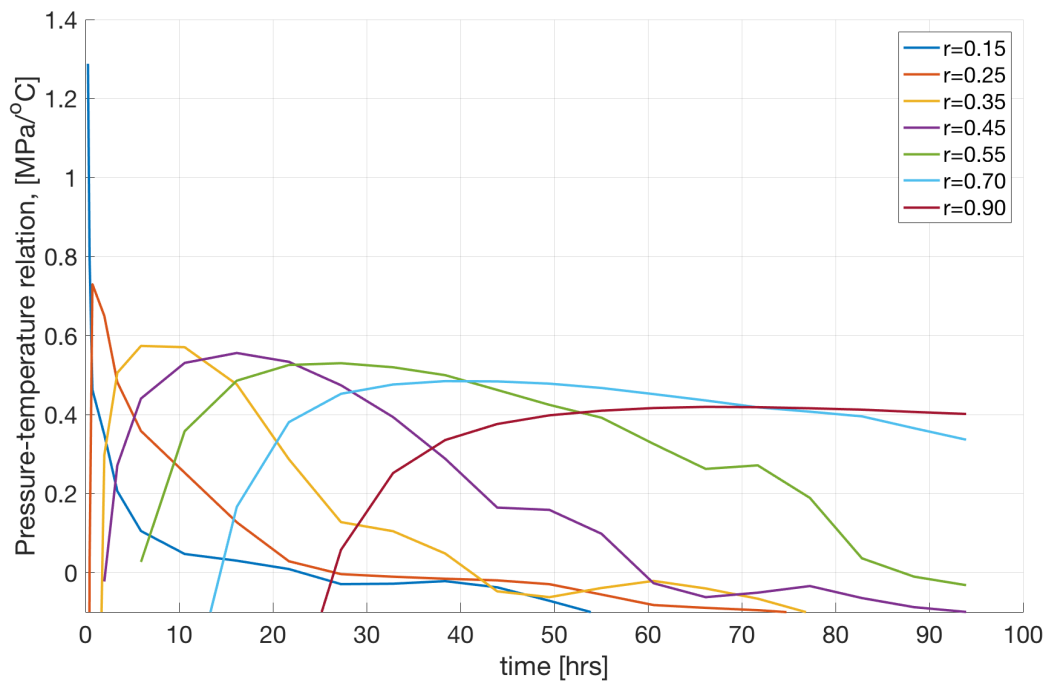


Figure B.42: Pressure-temperature relation, for case 4 at different radii from the borehole wall as function of time

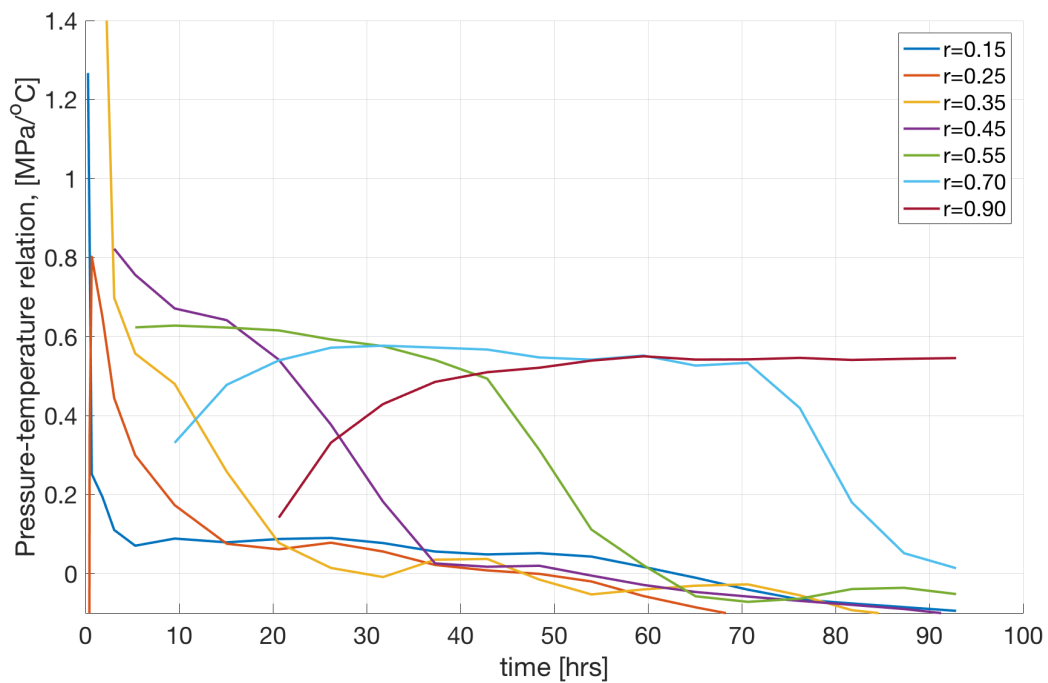


Figure B.43: Pressure-temperature relation, for case 5 at different radii from the borehole wall as function of time

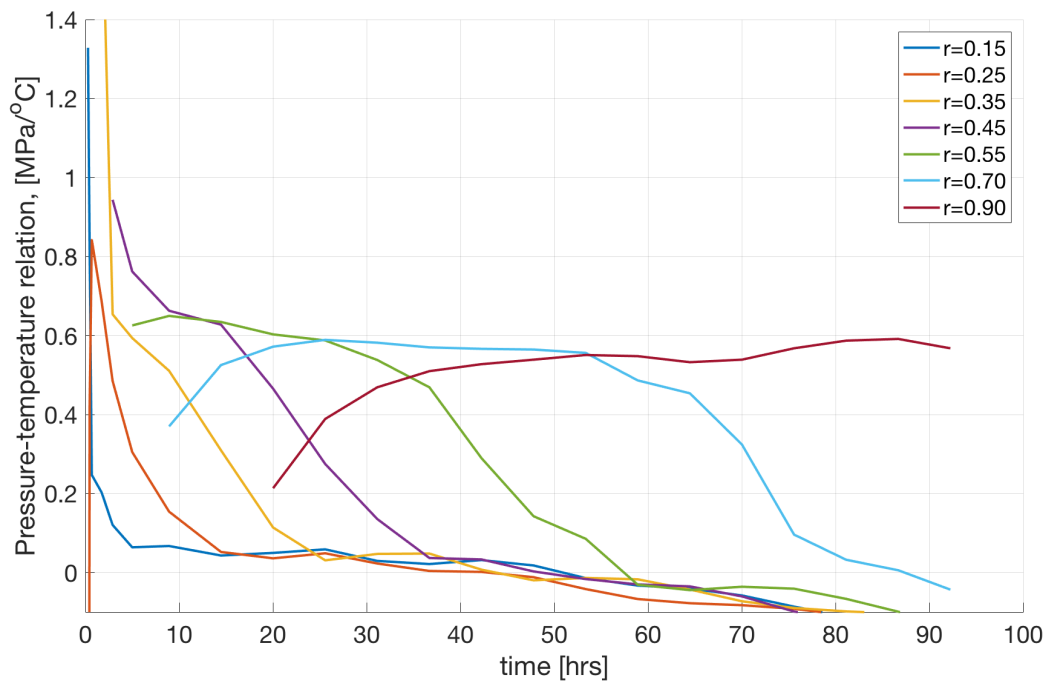


Figure B.44: Pressure-temperature relation, for case 6 at different radii from the borehole wall as function of time

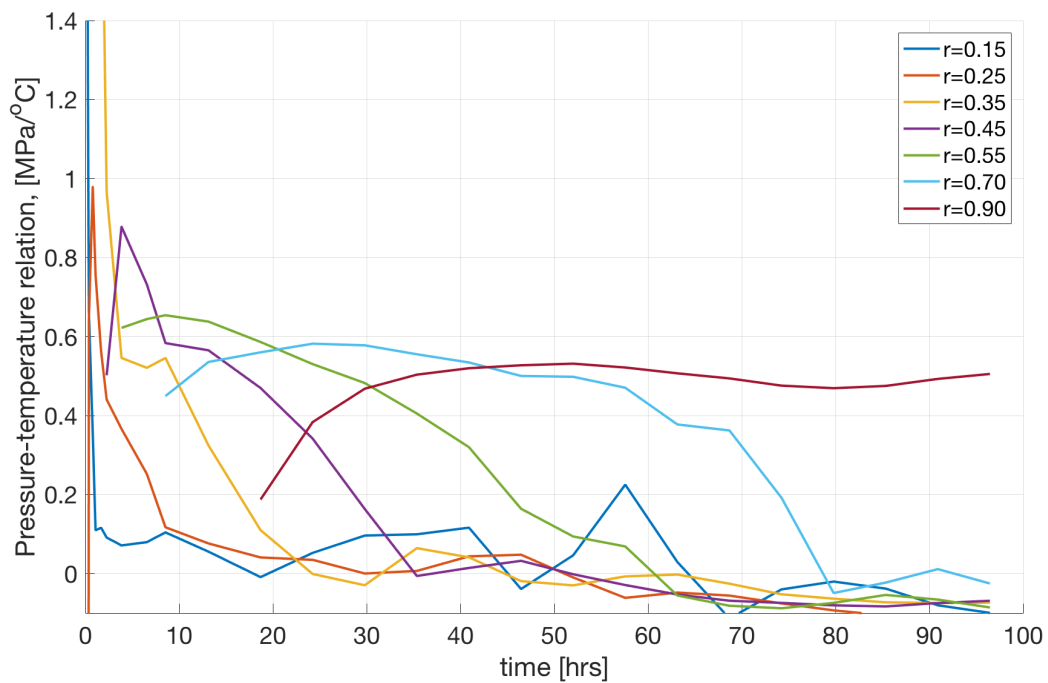


Figure B.45: Pressure-temperature relation, for case 7 at different radii from the borehole wall as function of time

B.4 Excerpts from ABAQUS displaying selected output parameters

B.4.1 Displacement

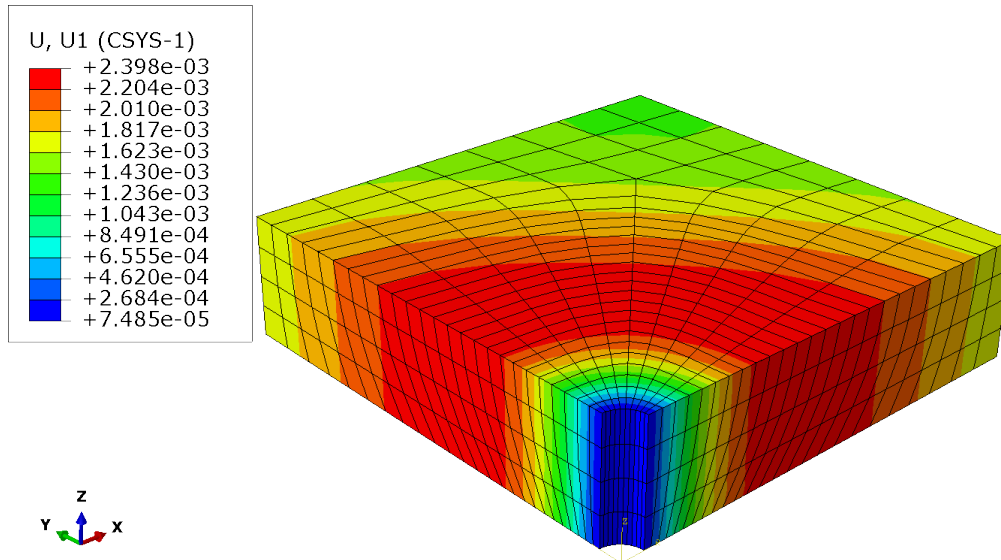


Figure B.46: Excerpt of ABAQUS FEA model for Case 2 displaying radial displacement at 97.2 h for a cutout of the lower 0.5 m of the model.

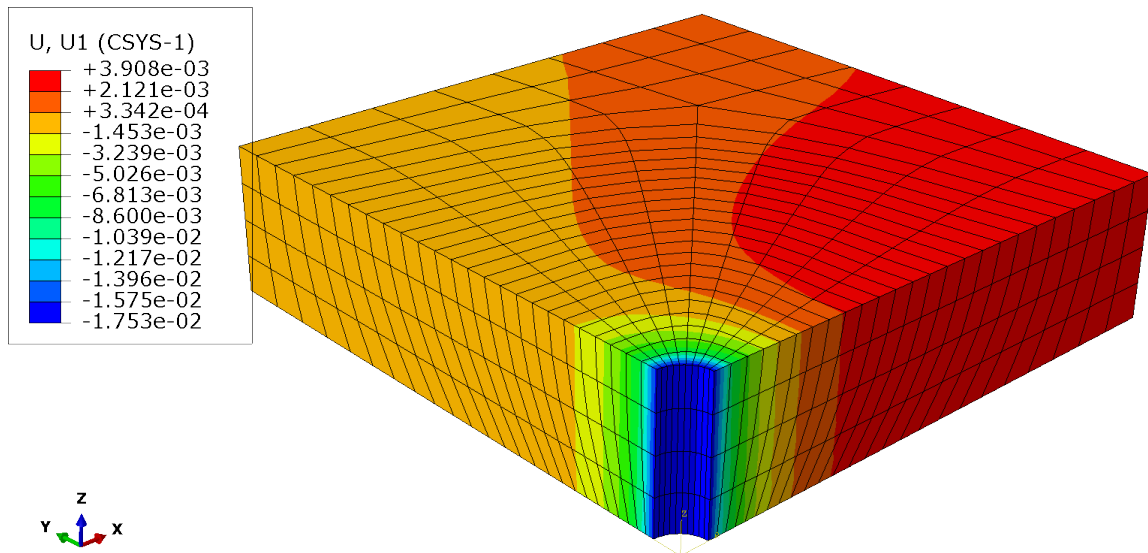


Figure B.47: Excerpt of ABAQUS FEA model for Case 3 displaying radial displacement at 97.2 h for a cutout of the lower 0.5 m of the model.

B.4.2 Radial plastic strain

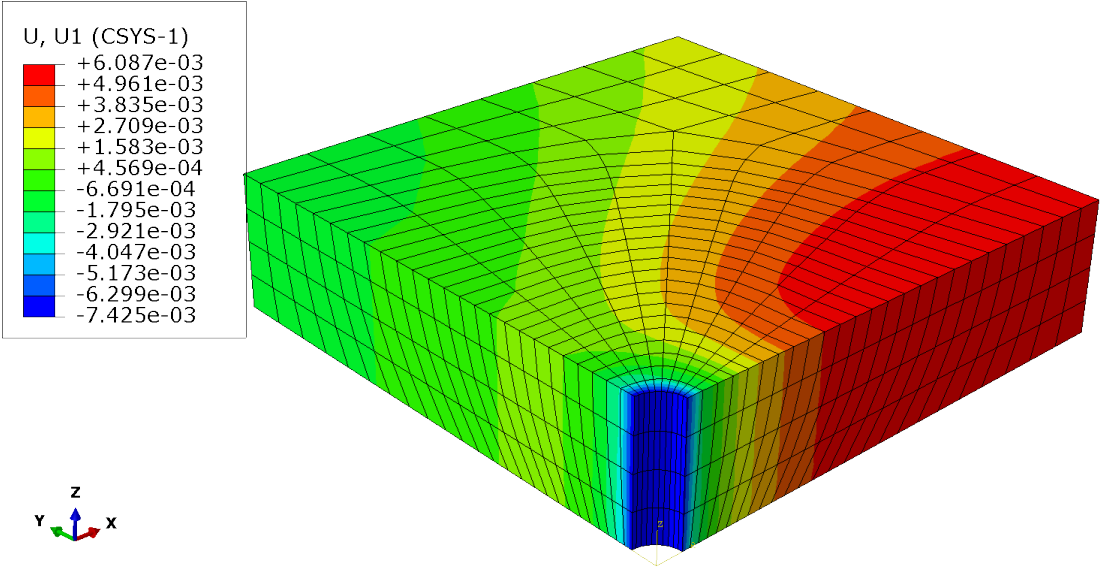


Figure B.48: Excerpt of ABAQUS FEA model for Case 4 displaying radial displacement at 97.2 h for a cutout of the lower 0.5 m of the model.

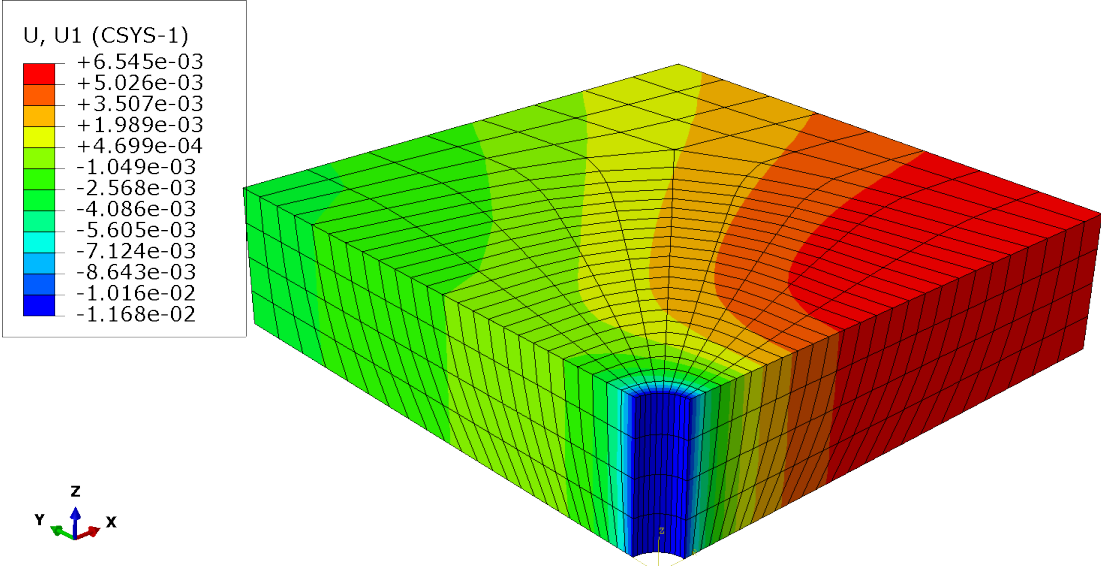


Figure B.49: Excerpt of ABAQUS FEA model for Case 5 displaying radial displacement at 97.2 h for a cutout of the lower 0.5 m of the model.

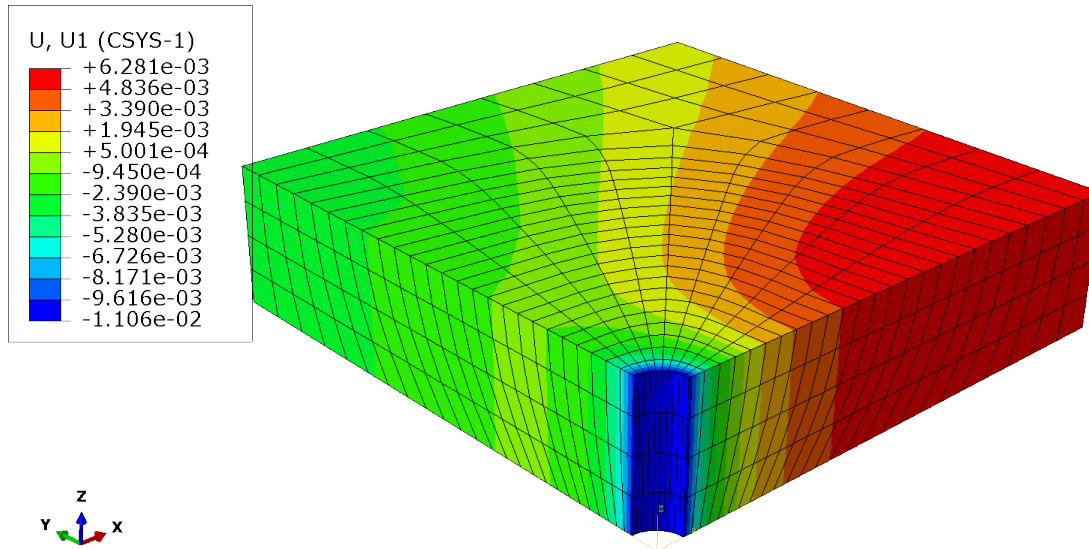


Figure B.50: Excerpt of ABAQUS FEA model for Case 6 displaying radial displacement at 97.2 h for a cutout of the lower 0.5 m of the model.

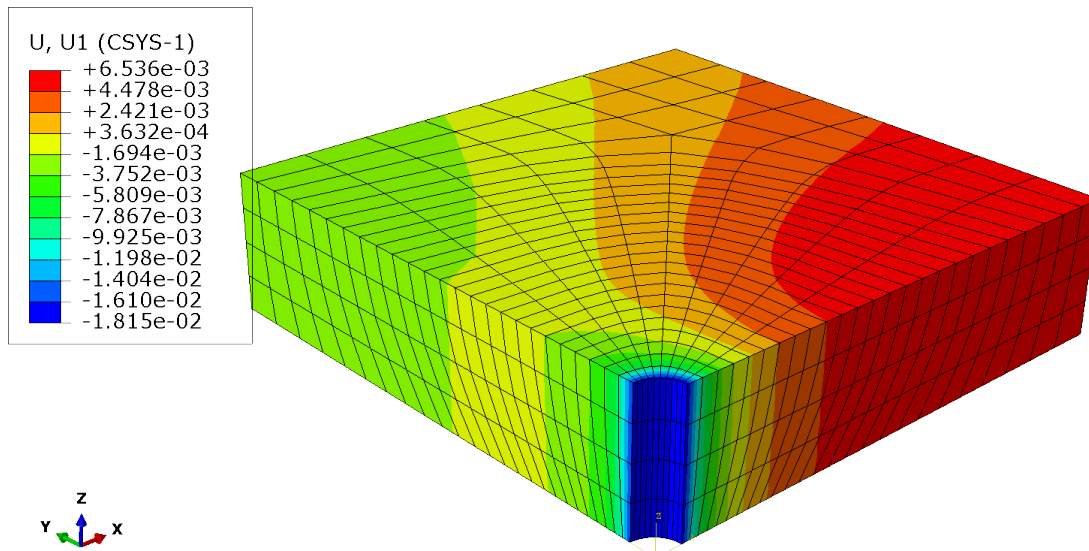


Figure B.51: Excerpt of ABAQUS FEA model for Case 7 displaying radial displacement at 97.2 h for a cutout of the lower 0.5 m of the model.

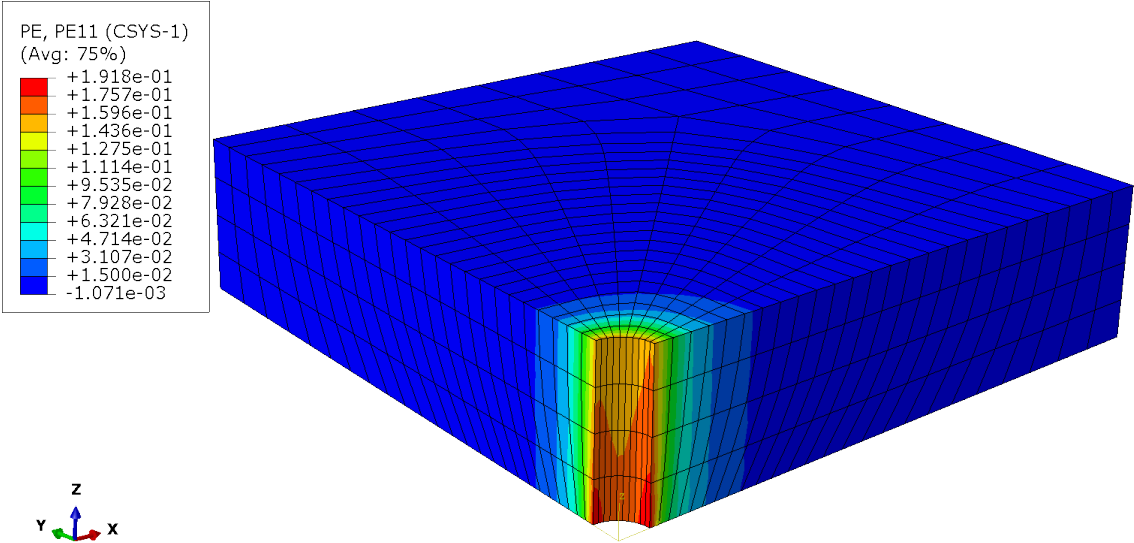


Figure B.52: Excerpt of ABAQUS FEA model for Case 3 displaying radial plastic strain at 97.2 h for a cutout of the lower 0.5 m of the model

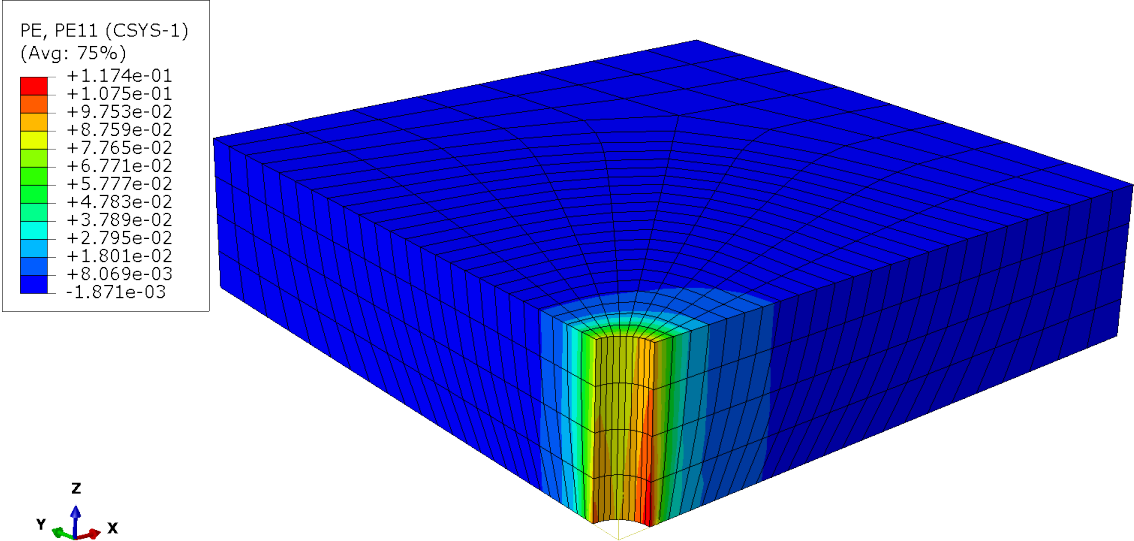


Figure B.53: Excerpt of ABAQUS FEA model for Case 4 displaying radial plastic strain at 97.2 h for a cutout of the lower 0.5 m of the model

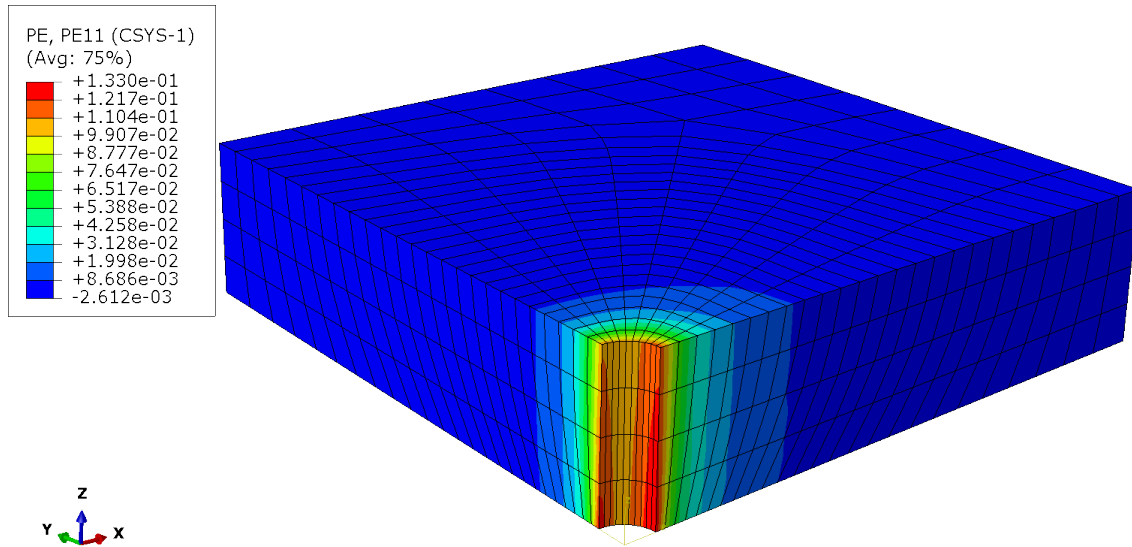


Figure B.54: Excerpt of ABAQUS FEA model for Case 5 displaying radial plastic strain at 97.2 h for a cutout of the lower 0.5 m of the model

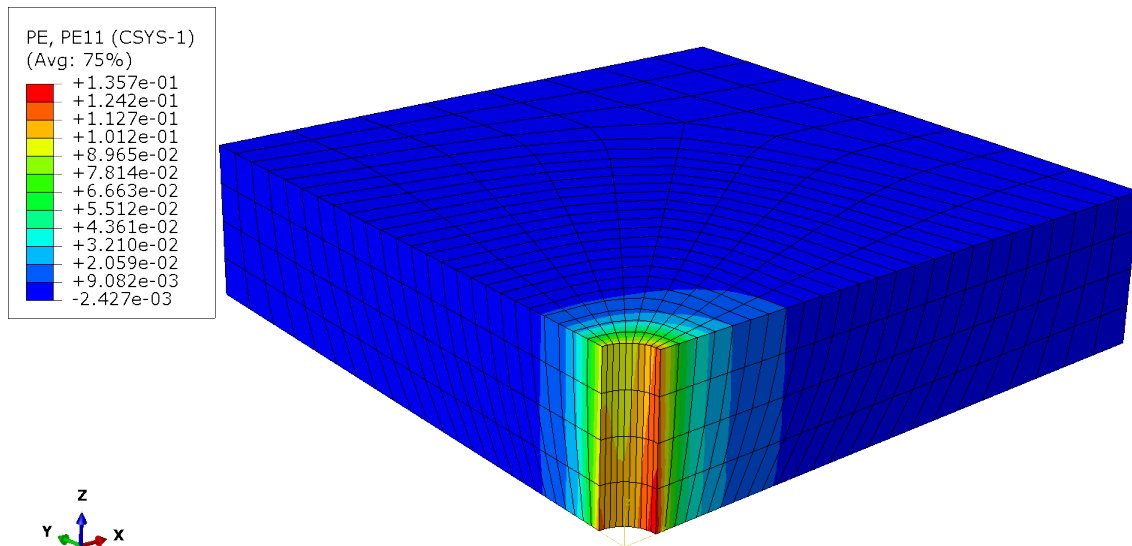


Figure B.55: Excerpt of ABAQUS FEA model for Case 6 displaying radial plastic strain at 97.2 h for a cutout of the lower 0.5 m of the model

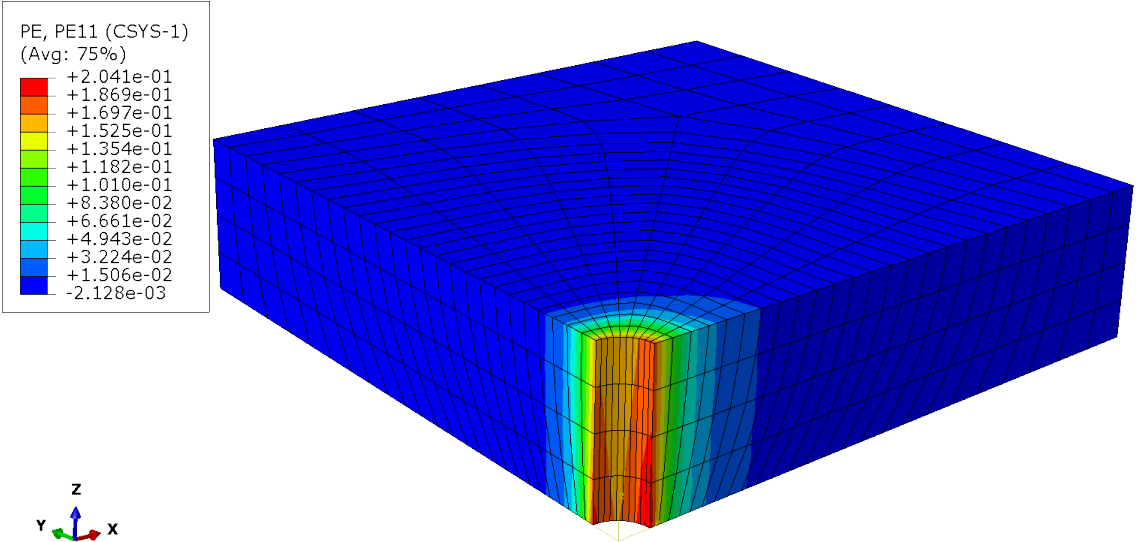


Figure B.56: Excerpt of ABAQUS FEA model for Case 7 displaying radial plastic strain at 97.2 h for a cutout of the lower 0.5 m of the model